AD-A045 825 BRITISH COLUMBIA UNIV VANCOUVER INST OF OCEANOGRAPHY F/G 8/3
TURBULENT ENERGY DISSIPATION IN THE ATLANTIC EQUATORIAL UNDERCU--ETC(U)
DEC 76 W R CRAWFORD N00014-76-C-0446

UNCLASSIFIED NL

1 OF 2
ADA045825

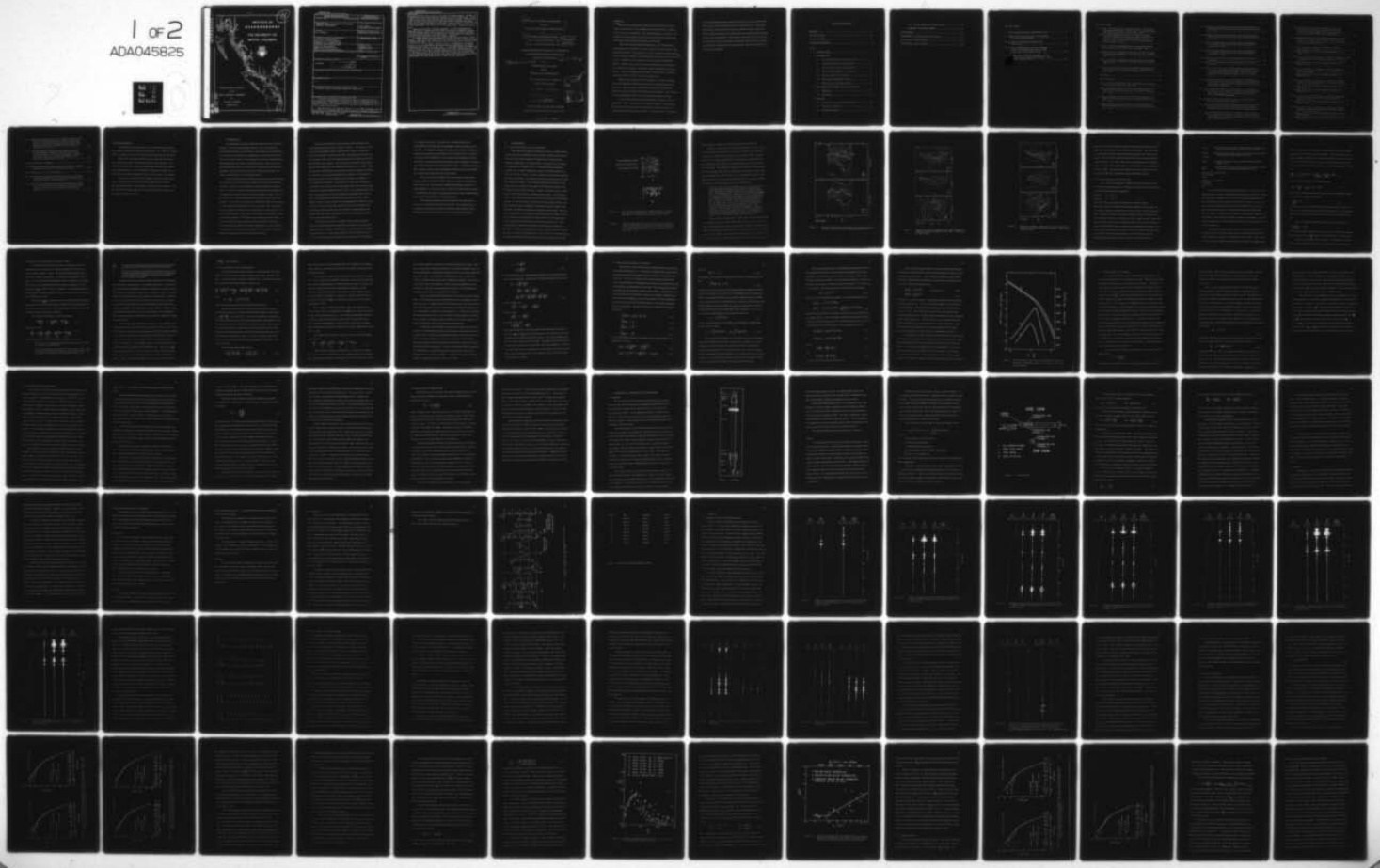

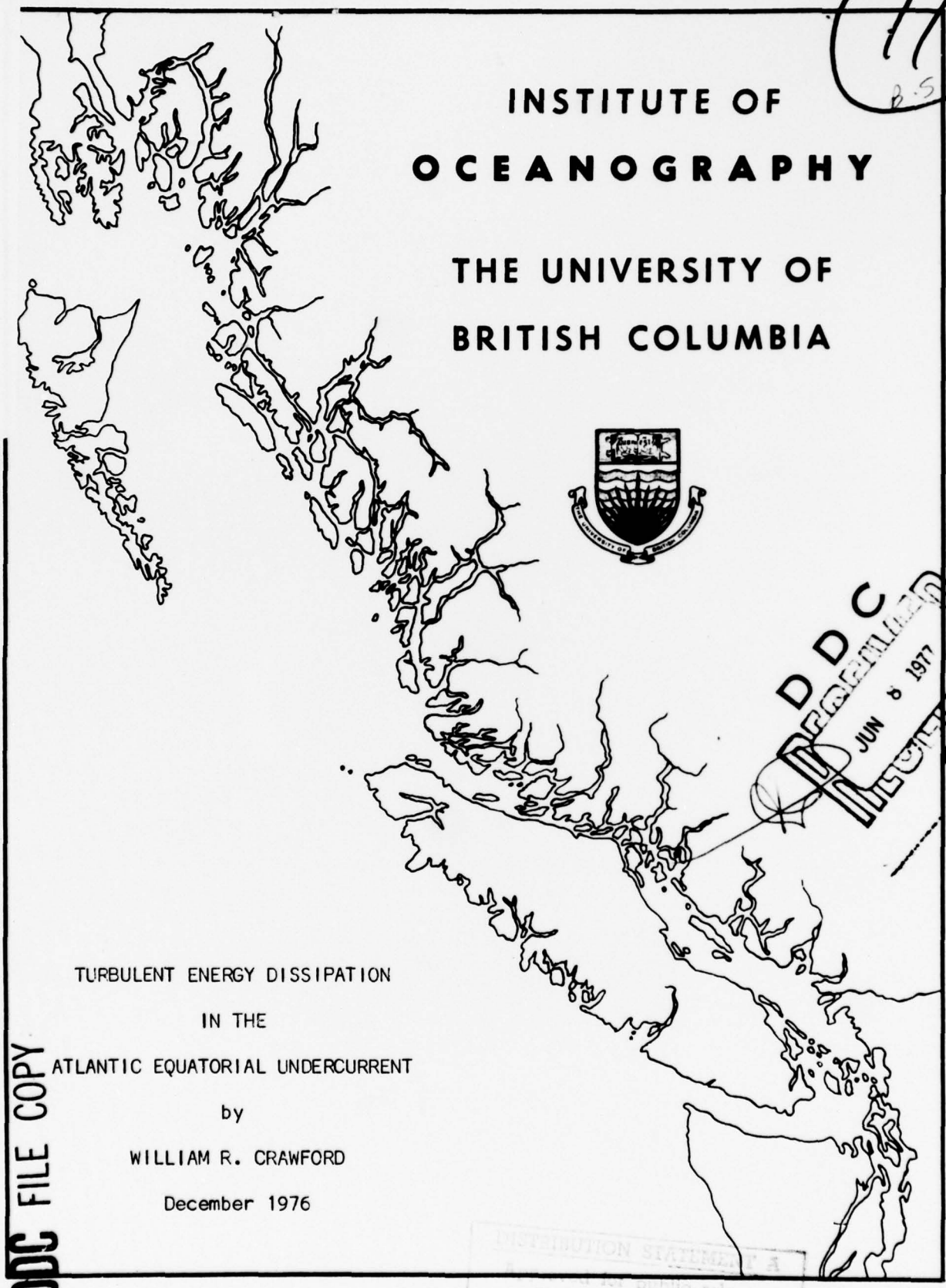

INSTITUTE OF OCEANOGRAPHY

THE UNIVERSITY OF BRITISH COLUMBIA

TURBULENT ENERGY DISSIPATION

IN THE

ATLANTIC EQUATORIAL UNDERCURRENT

by

WILLIAM R. CRAWFORD

December 1976

UNCLASSIFIED

SECURITY CLASSIFICATION OF THIS PAGE (When Data Entered)

REPORT DOCUMENTATION PAGE		READ INSTRUCTIONS BEFORE COMPLETING FORM
1. REPORT NUMBER	2. GOVT ACCESSION NO.	3. RECIPIENT'S CATALOG NUMBER
4. TITLE (and Subtitle) TURBULENT ENERGY DISSIPATION IN THE ATLANTIC EQUATORIAL UNDERCURRENT.		5. TYPE OF REPORT & PERIOD COVERED Ph.D. Thesis
		6. PERFORMING ORG. REPORT NUMBER --
7. AUTHOR(s) W. R. Crawford		8. CONTRACT OR GRANT NUMBER(s) N00014-76-C-0446 NR 083-207
9. PERFORMING ORGANIZATION NAME AND ADDRESS Institute of Oceanography University of British Columbia Vancouver, B.C., Canada V6T 1W5		10. PROGRAM ELEMENT, PROJECT, TASK AREA & WORK UNIT NUMBERS ---
11. CONTROLLING OFFICE NAME AND ADDRESS Office of Naval Research NORDA Code 410/ONR Code 481 Bay St. Louis, Mississippi 39520		12. REPORT DATE December, 1976
		13. NUMBER OF PAGES 149
14. MONITORING AGENCY NAME & ADDRESS (if different from Controlling Office)		15. SECURITY CLASS. (of this report)
		15a. DECLASSIFICATION/DOWNGRADING SCHEDULE

16. DISTRIBUTION STATEMENT (of this Report)

Unlimited

DISTRIBUTION STATEMENT A
Approved for public release;
Distribution Unlimited

17. DISTRIBUTION STATEMENT (of the abstract entered in Block 20, if different from Report)

--

18. SUPPLEMENTARY NOTES

---

19. KEY WORDS (Continue on reverse side if necessary and identify by block number)

Turbulence, Energy dissipation, Equatorial undercurrent.

20. ABSTRACT (Continue on reverse side if necessary and identify by block number)

A free-fall oceanographic instrument has been used to measure vertical microstructure scale gradients of horizontal velocity, temperature and electrical conductivity. The velocity gradients, or shears, were measured at scales between 3 and 40 cm by an airfoil shear probe whose specifications and calibration procedure are discussed.

Data collected in the equatorial Atlantic in July 1974 indicated a consistent pattern of turbulence near the velocity core of the Atlantic Equatorial

DD FORM 1 JAN 73 1473 EDITION OF 1 NOV 65 IS OBSOLETE S/N 0102-LF-014-6601

UNCLASSIFIED

SECURITY CLASSIFICATION OF THIS PAGE (When Data Entered)

20. cont'd

Undercurrent. (The velocity core is the region of maximum speed.) The most intense turbulence was found above the velocity core of the undercurrent. Turbulence in the velocity core was weak and intermittently spaced. Below the core, near the base of the thermocline, moderately intense turbulence was found. The rate of viscous dissipation of turbulent energy has been estimated from the shear measurements, and typical values were $3 \times 10^{-3} cm^2 sec^{-3}$ above the velocity core.

Spectra of the shears have been computed. At small wavelengths the measured spectral coefficients fall below the unversal Kolmogoroff spectrum. This discrepancy between the two spectra is attributed to spatial averaging of velocity fluctuations by the shear probe. The estimates of viscous dissipation include a correction for this spatial averaging.

An energy balance has been determined for the turbulent velocity fluctuations. Above and below the core the basic balance is local production of turbulent energy equals local dissipation, and this balance gives a vertical eddy viscosity of order $10\ cm^2 sec^{-1}$ above the core. The equation of the energy balance of the average motion has been vertically integrated at the equator where meridional terms are assumed small. In the South Equatorial Current the rate of energy gain from the average zonal wind stress is balanced by the rate of energy loss to the zonal pressure gradient plus the rate of dissipation. In the under current, above the core, the rate of energy gain from the zonal pressure gradient equals the rate of dissipation within the uncertainty of the measurements, and the advection term is small but not negligible.

(6)

TURBULENT ENERGY DISSIPATION IN THE ATLANTIC EQUATORIAL UNDERCURRENT,

by

(10) WILLIAM ROBERT CRAWFORD

B. Sc., University of Waterloo, 1970

M. A. Sc., University of Waterloo, 1972

(11) Dec 76

(12) 165p.

A THESIS SUBMITTED IN PARTIAL FULFILLMENT OF

THE REQUIREMENTS FOR THE DEGREE OF

DOCTOR OF PHILOSOPHY (9) Doctoral thesis

(15) N00014-76-C-0446

in the

DEPARTMENT OF PHYSICS

and the

INSTITUTE OF OCEANOGRAPHY

We accept this thesis as conforming

to the required standard

.....

.....

.....

THE UNIVERSITY OF BRITISH COLUMBIA

063 770

LB

ABSTRACT

A free-fall oceanographic instrument has been used to measure vertical microstructure scale gradients of horizontal velocity, temperature and electrical conductivity. The velocity gradients, or shears, were measured at scales between 3 and 40 cm by an airfoil shear probe whose specifications and calibration procedure are discussed.

Data collected in the equatorial Atlantic in July 1974 indicated a consistent pattern of turbulence near the velocity core of the Atlantic Equatorial Undercurrent. (The velocity core is the region of maximum speed.) The most intense turbulence was found above the velocity core of the undercurrent. Turbulence in the velocity core was weak and intermittently spaced. Below the core, near the base of the thermocline, moderately intense turbulence was found. The rate of viscous dissipation of turbulent energy has been estimated from the shear measurements, and typical values were 3×10^{-3} $cm^2 sec^{-3}$ above the velocity core.

Spectra of the shears have been computed. At small wavelengths the measured spectral coefficients fall below the universal Kolmogoroff spectrum. This discrepancy between the two spectra is attributed to spatial averaging of velocity fluctuations by the shear probe. The estimates of viscous dissipation include a correction for this spatial averaging.

An energy balance has been determined for the turbulent velocity fluctuations. Above and below the core the basic balance is local production of turbulent energy equals local dissipation, and this balance gives a vertical eddy viscosity of order 10 $cm^2 sec^{-1}$ above the core. The equation

of the energy balance of the average motion has been vertically integrated at the equator where meridional terms are assumed small. In the South Equatorial Current the rate of energy gain from the average zonal wind stress is balanced by the rate of energy loss to the zonal pressure gradient plus the rate of dissipation. In the undercurrent, above the core, the rate of energy gain from the zonal pressure gradient equals the rate of dissipation within the uncertainty of the measurements, and the advection term is small but not negligible.

TABLE OF CONTENTS

LIST OF TABLES

LIST OF FIGURES

ACKNOWLEDGMENTS

I would like to thank my supervisor, Dr. Osborn for the guidance and support he gave during all stages of this thesis. Dr. Pond, Dr. Burling and Dr. Cartshore have also given many helpful comments and criticisms.

Many of the conclusions of this thesis rely upon both my measurements and those of other investigators during the GATE program. I am especially indebted to Dr. Katz of the Woods Hole Oceanographic Institute who supplied ship time on the ATLANTIS II and together with Mr. Bruce provided much valuable information of large scale features at the equator.

The Camel was designed by Dr. Osborn, and the electronics work and the construction of the Camel and shear probes were the work of Mr. Rick Wards and Mr. David English, who deserve special thanks. I am grateful for the financial support the National Research Council has given me during my studies at U. B. C.

1. INTRODUCTION

The energetics of equatorial undercurrents have received limited attention. For a flow in geostrophic balance, there is no transfer of energy between the pressure and kinetic energy fields, since the Coriolis force can do no work and flow is perpendicular to the pressure gradient. The rate of energy transfer in most regions of the oceans depends upon the ageostrophic flow across lines of constant pressure, which is relatively low and difficult to measure. However, at the equator the Coriolis force disappears, allowing the exchange of energy between the pressure and kinetic energy fields to be more easily measured.

Even the simplest energy balance for the undercurrent must include the work done by the zonal pressure gradient, the energy advected by the mean flow, and the energy dissipated by turbulence (Wyrtki and Bennett, 1963). The rate of release of energy from the zonal pressure gradient can be obtained from measurements of velocity and dynamic height. However, the velocity cores of the equatorial undercurrents have been observed to meander. To accurately determine the velocity field, either measurements at several locations must be taken, or many sections across the equator must be sampled. Until 1974, such observations were not available. The energy advected by the average flow remains difficult to calculate because of limited observations. The undercurrents undergo seasonal changes, as well as meanders of shorter period. Most measurements of the large scale features of the undercurrents have usually been at a single position and extend over a relatively short time interval, so it has been difficult to distinguish temporal variations from spatial variations.

The rate of dissipation of kinetic energy can be estimated from velocity measurements at scales of about 1 to 50 cm. This range of scales is the viscous dissipation range at which kinetic energy is converted to heat by the molecular viscosity of the fluid. Instrumentation to sense velocity gradients at the scales and magnitudes found in the undercurrents has been developed only recently. Only one previous attempt has been made to measure these gradients in the undercurrent (Belyaev et al, 1975b). From measurements of temperature fluctuations and the use of theories of isotropic turbulence, the rate of dissipation may be inferred, as was done by Williams and Gibson (1974) at 0° and 1° N in the Pacific, at 150° W, at a single depth at each latitude. An estimate of vertical heat transport for certain flows can be made from measurements of the mean and microscale temperature gradients (Osborn and Cox, 1972). Such measurements in the Pacific at the equator have given a qualitative comparison of the microscale velocity gradients and the intensity of turbulence (Gregg, 1976). Although theories suggest that the rate of dissipation ($\bar{\epsilon}$) should be a limiting factor in the flow of the undercurrent, the values of $\bar{\epsilon}$ suggested by these studies differ from the value derived from a study by Wyrtki and Bennett (1963) based upon measurements of large scale features in the Pacific Equatorial Undercurrent.

In the summer of 1974, participants in the Global Atmospheric Research Program undertook a study of the atmosphere and ocean in the tropical Atlantic, called the GARP Atlantic Tropical Experiment (GATE). During this project, a study of the microscale velocity gradients in and near the undercurrent was undertaken with instrumentation developed by

T.R. Osborn and myself. The study was conducted from the R/V ATLANTIS II of the Woods Hole Oceanographic Institute during June and July 1974. An extensive mapping of the large scale velocities and dynamic heights at the equator was undertaken by Dr. Eli Katz and Mr. John Bruce on board the R/V ATLANTIS II, and by numerous investigators on board other ships. These large scale measurements make it possible to estimate some of the transfers of the average kinetic energy. A comparison between these transfers and the viscous dissipation of turbulent energy is possible for a long term average of the flow at the equator.

There are clearly two topics here: the energetics of the undercurrents, and of microscale oceanic turbulence, which are separated not only by scale size, but also by the background information required to understand them. In the next section, I will discuss these topics separately, and show how microscale measurements lead to a better understanding of the overall energy balance in the undercurrent.

The design and operation of the instruments will be discussed in section 3, as well as the procedure in the field. The microstructure of the undercurrent region, the nature and spectra of the turbulence there, and the energetics of the undercurrent will be described in section 4.

2. BACKGROUND

2.1 Large Scale Features of the Undercurrent

There have been numerous models constructed to explain and predict the nature of the equatorial undercurrents, beginning soon after the discovery of the Pacific Equatorial Undercurrent, as described by Cromwell, Montgomery and Stroup (1954). A summary of such models was undertaken by Philander (1973). To understand why equatorial currents exist, a simple explanation is given by Neumann and Pierson (1966, p. 453-454). Figure 1a shows a wind and current pattern typically found near the equator. The doldrums between the SE and NE trade winds are located near 5°north. In the Southern Hemisphere, transport in the Ekman layer is to the left of the wind; in the Northern Hemisphere this transport is to the right of the wind, causing a convergence of the surface waters at 5°N and divergence at 10°N and at the equator. The resulting surface slope caused by such convergences and divergences is illustrated in figure 1b. For the surface currents to be in geostrophic balance with the meridional pressure gradients caused by these surface slopes, they must flow westward at all latitudes except between 5°and 10°N. The eastward current here is the Equatorial Countercurrent in the Atlantic Ocean. The westward current present to the south of 5°N is the South Equatorial Current and that north of 10°N is the North Equatorial Current. This current pattern is most like that found in the Atlantic from August to November. During the remainder of the year, when the winds are weaker, the countercurrent is frequently absent. In the Pacific, this countercurrent is labelled the North Equatorial Countercurrent to distinguish it from the

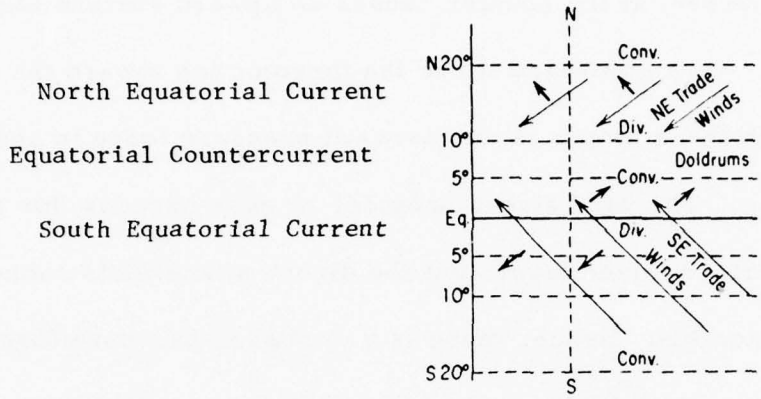

(a)

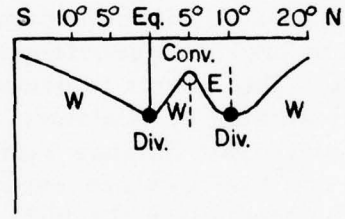

(b)

Figure 1a Possible wind distribution in equatorial regions. Long arrows represent wind direction. Short arrows show possible Ekman drift. (from Neumann and Pierson, 1966 p. 452)

Figure 1b Idealized topography of the sea surface across the equator caused by wind pattern of figure 1a. Surface water divergences or convergences are denoted by DIV. or CONV. and direction of flow is denoted by E or W. (from Neumann and Pierson, 1966 p. 452)

South Equatoral Countercurrent sometimes found near 10° south.

When the winds and surface currents are present as shown in figures 1a and 1b the undercurrent is set up in the following way: the westward surface current at the equator causes an upward surface slope toward the west, and a downward tilt of the thermocline toward the west. Associated with these slopes is an eastward pressure force in and above the thermocline. The wind stress balances or even exceeds this pressure force in the surface mixed layer, but the direct wind effects cannot penetrate the thermocline. Hence, there is a westward pressure force in the thermocline which is not balanced by the wind stress. Near the equator this causes an eastward flow of water in the thermocline.

> "However, with increasing distance from the equator the effects of the Coriolis force become more and more significant and tend to provide a geostrophic balance of the zonal pressure gradient. This seems to occur very close to the equator, probably as close as $\frac{1}{2}$° or 1° latitude. Quantitative evidence of approximate geostrophic balance within the undercurrent to latitudes as low as $\frac{1}{2}$° has been presented by Montgomery and Stroup (1962) and by Metcalf et al (1962). Thus, with a downward slope of the sea surface from west to east a little north of the equator, the water flows with a Southward component, and a little south of the equator with a Northward component..... This leads to a water transport from both the Northern and Southern Hemisphere toward the equator where the general motion is eastward and provides ample water supply for the Equatorial Undercurrent." (Neumann and Pierson 1966, p. 454.)

Cross-sections of temperature, salinity and velocity sampled during the ATLANTIS II sections along 24°W, 28°W, 33°W are shown in figures 2 to 4. The divergence of surface currents at the equator, combined with inflow from the sides in the thermocline, leads to upwelling near the equator and causes the ridging and troughing of the isotherms shown in figures 2 to 4. This structure is a characteristic of all equatorial undercurrents. The

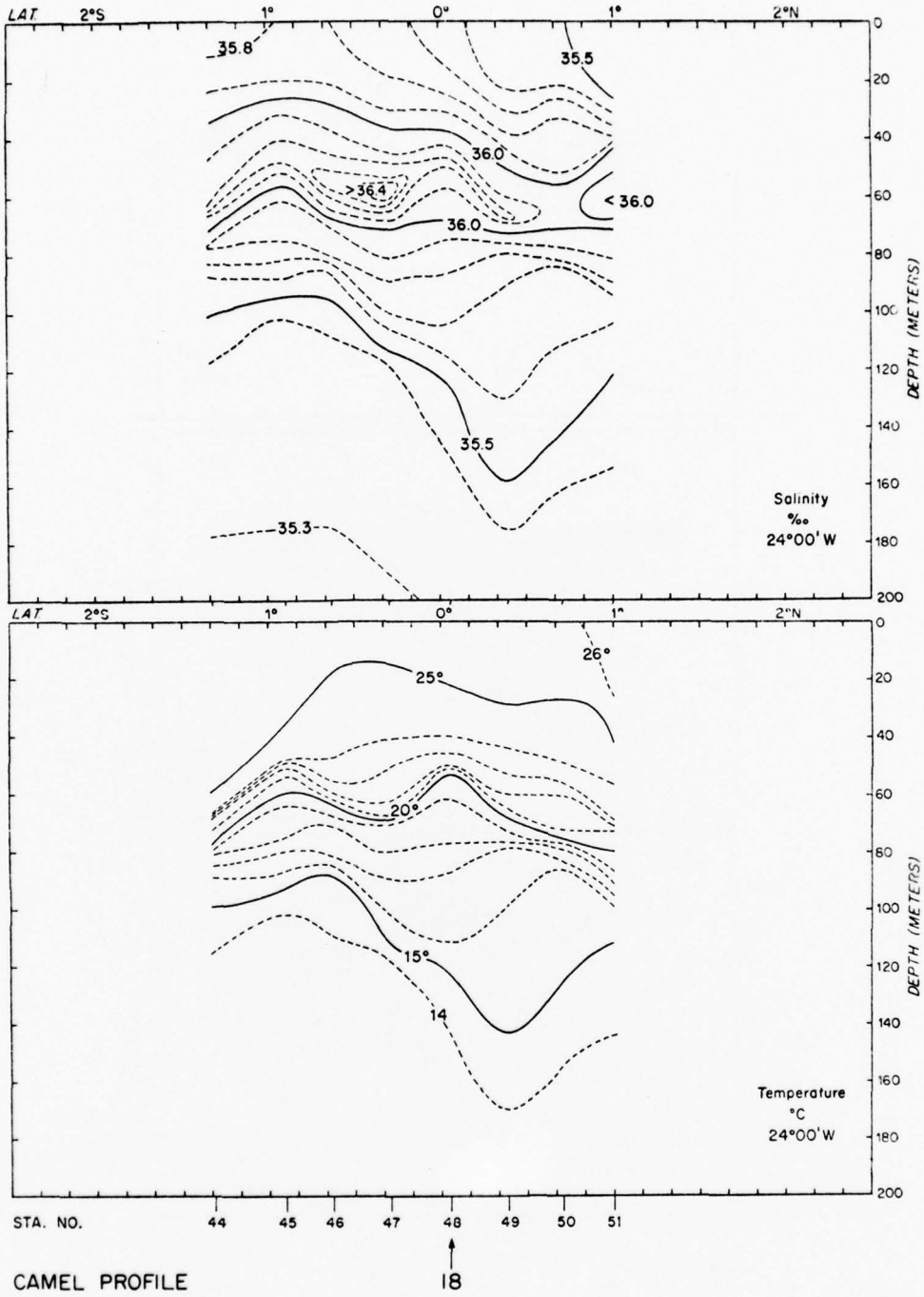

Figure 2 Contours of salinity and temperature in the Equatorial Atlantic alone 24°W in July 1974. (from Bruce and Katz 1976)

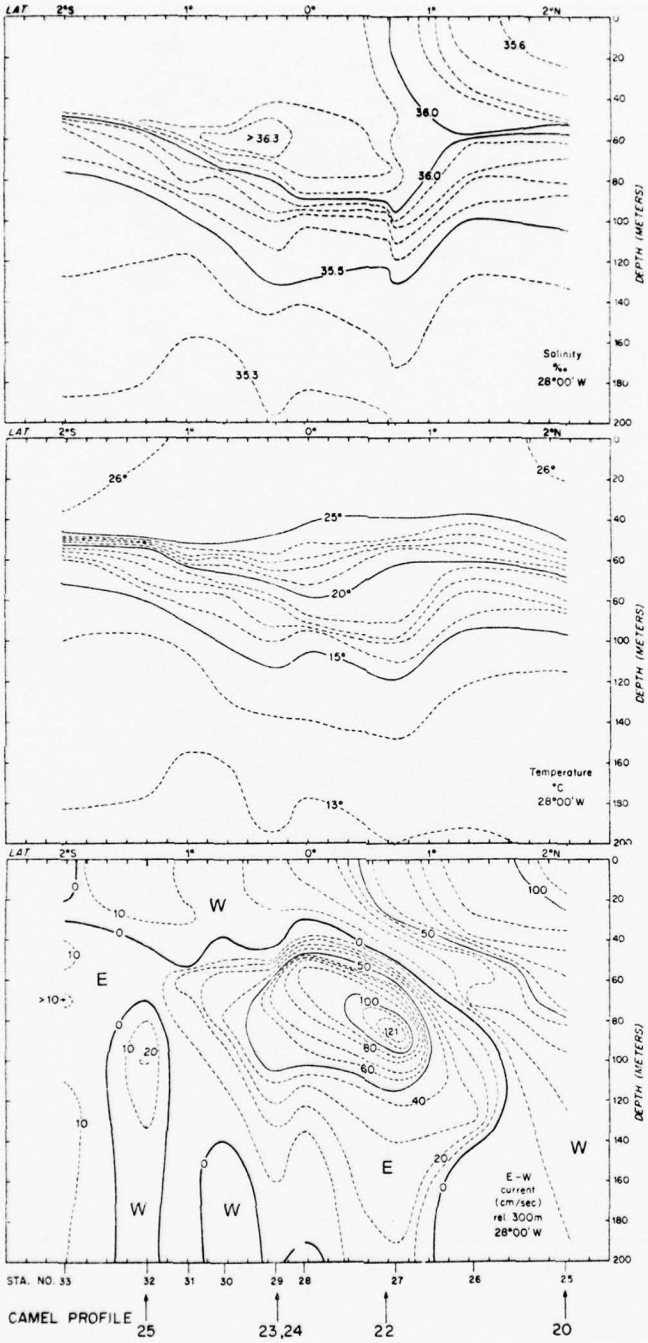

Figure 3 Contours of salinity, temperature and zonal current in the Equatorial Atlantic along 28°W in July 1974. (from Bruce and Katz, 1976)

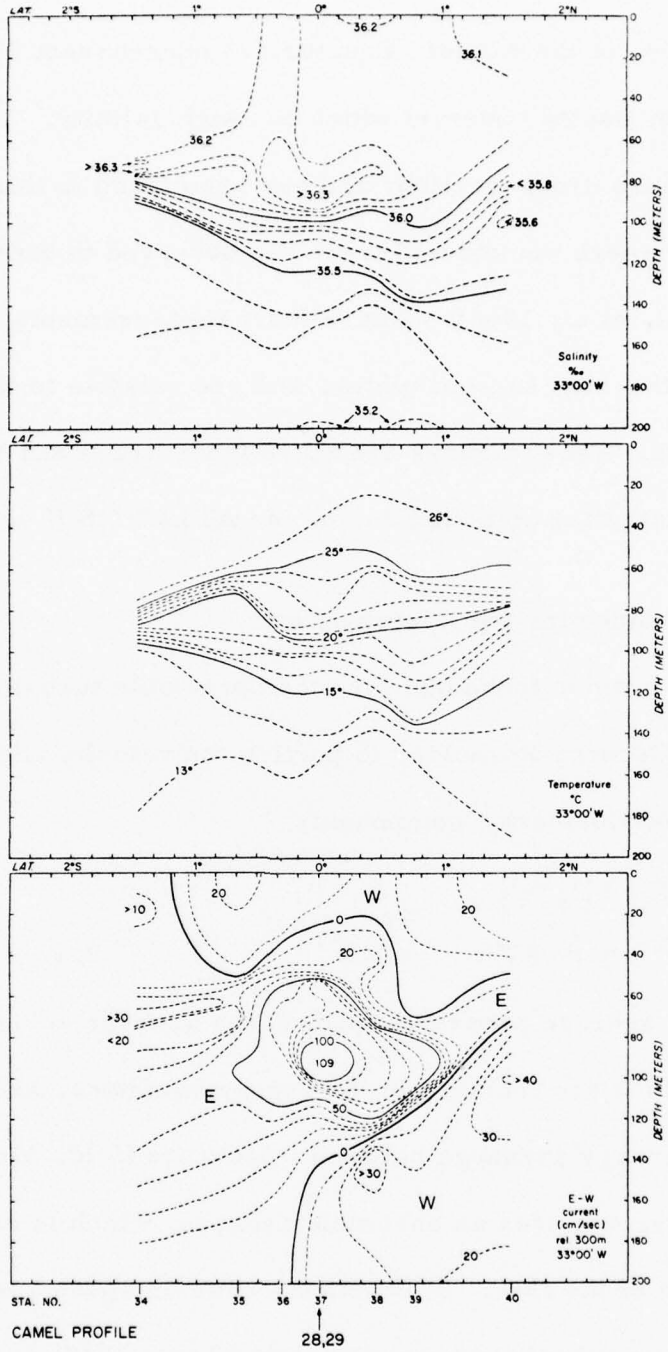

Figure 4 Contours of salinity, temperature and zonal current in the Equatorial Atlantic along 33°W in July 1974. (from Bruce and Katz, 1976)

water in the core of the Atlantic Equatorial Undercurrent derives from the North Brazilian Coastal Current which has high salinity. This saline core is evident in these cross-sections and has been found in this undercurrent as far as 6°E, where the undercurrent was observed to turn away from the equator (Rinkel, et al, 1966). The velocity measurements were obtained from an over-the-side current meter, and are relative to the measurement at 300 m. depth. These figures are taken from Bruce and Katz (1976) and are based on data they collected during the ATLANTIS II cruise.

2.2 Energy Balance for the Average Flow

It is a common technique for incompressible turbulent flows, first introduced by Osborne Reynolds, to portion the velocity and pressure fields into average and fluctuating components

velocity $\quad \upsilon_i = U_i + u_i$

pressure $\quad P = \bar{P} + p'$ $\qquad$ 2.1

where $\bar{P}$ is the average pressure and U_i is the average velocity.

When these values are included in the energy equations, and averaged, one can trace the energy exchange between a pressure field, kinetic energy and heat. In theory, one uses an ensemble average, which is an average over all realizations of the flow. In practice a time or space average is measured within the flow and the Ergodic hypothesis (Hinze, 1959, p. 5) is invoked so that the measurements can be assumed to be comparable to the theory. For time averages one must ask: are the averages over a time sufficiently long to include all or most of the fluctuations? Some periods at which the Atlantic Equatorial Undercurrent is expected to contain energy are:

1 year	Annual variations in the winds likely produce changes in the undercurrent (Philander, 1973), (Katz et al, 1976)
16 days + - 2 days	Meandering of the undercurrent was observed in the summer of 1974 during GATE (Düing et al, 1975)
3 days	Pulsing of the undercurrent was observed during GATE (Düing, 1975)
12-25 hours	Variations due to tides, with the semi-diurnal tide strongest were observed during GATE (Rybnikov, 1975)
several mintes to several hours	Internal waves
fractions of seconds to several minutes	Turbulence

Prior to the GATE oceanographic observations in 1974, there were insufficient observations to permit distinction between variations of several days and annual variations. The 16 day $\pm$2 day meander appeared in the three GATE observation periods of 21 days each, but there were also variations from one observation period to another which may or may not be part of an annual variation. The observations during the GATE project form the longest set available and in many cases permit averaging over the 16 day wave. No averages over longer variations are available. The effect of short sampling times upon the observations of the mean gradients may be large in some cases.

To obtain the energy equation of the average flow, the average and fluctuating values of velocity and pressure are substituted into the Navier-Stokes equation for a fluid of constant density and viscosity. The coordinate system is chosen with x_1 eastward along the equator, x_2 northward with

origin at the equator, and x_3 positive upward and zero at a level surface chosen to be close to the actual ocean surface. Each term in the Navier-Stokes equation is multiplied by U_i and an ensemble average of each term is taken. When all the terms are summed, the rate of change of kinetic energy per unit mass and per unit time is, in tensor form (Hinze, 1959, p. 65):

$$\frac{\partial Q^2}{\partial t} = -\frac{\partial}{\partial x_j} U_i\left(\frac{\bar{P}}{\rho} + Q^2\right) + \nu U_i \frac{\partial^2 U_i}{\partial x_j \partial x_j} - U_i \frac{\partial \overline{u_i u_j}}{\partial x_j} - g U_3 \qquad 2.2$$

where the overbar denotes an ensemble average,

$$Q^2 = \frac{U_i U_i}{2} = \frac{1}{2}\left[U_1^2 + U_2^2 + U_3^2\right] \qquad 2.3$$

is the kinetic energy per unit mass, and use has been made of the continuity equation for incompressible flows

$$\frac{\partial U_i}{\partial x_i} = 0 \qquad 2.4$$

The term $-gU_3$ has been added to Hinze's equations because, while he is able to use a reduced pressure (total minus hydrostatic), such an approach cannot be used in this case because of the presence of a free sloping surface.

It is assumed that the hydrostatic balance is valid, and hence

$$\frac{U_3}{\bar{\rho}} \frac{\partial \bar{P}}{\partial x_3} = -g U_3 \qquad 2.5$$

To reduce the number of terms, the $-gU_3$ term may be omitted by adopting the convention that the $U_i \frac{\partial \bar{P}}{\partial x_i}$ term is to be summed over i=1 and 2 but not 3.

There is no Coriolis term in equation 2.2. Although the Coriolis force can alter the direction of flow, it cannot change the speed of flow

and cannot alter the magnitude of the kinetic energy.

If a small density variation is present, the density field can be portioned into an average and a fluctuating component $\rho = \bar{\rho} + \rho'$ in the Navier-Stokes equations. If $\rho' \ll \bar{\rho}$, the Boussinesq approximation may be invoked to simplify the equations. As outlined by van Mieghem (1973), if $\frac{\rho'}{\bar{\rho}} \leq 10^{-2}$, the Boussinesq approximation holds: variations in the density of the fluid are only important where they affect the buoyancy. For the undercurrent, $\frac{\rho'}{\bar{\rho}} \leq 2\text{x}10^{-3}$. Hence, in equation 2.2, the density ρ may be replaced by the average density $\bar{\rho}$, but it must be outside the derivative for the equation to be correct.

The term $\nu U_i \frac{\partial^2 U_i}{\partial x_j \partial x_j}$ in equation 2.2 is the sum of the rate of dissipation per unit mass of the kinetic energy, and the rate of work done per unit mass by the viscous stresses. For oceanic flows, this term is very small compared to others and may be neglected.

The last term in equation 2.2 may be rewritten

$$-U_i \frac{\partial \overline{u_i u_j}}{\partial x_j} = -\frac{\partial U_i \overline{u_i u_j}}{\partial x_j} + \overline{u_i u_j} \frac{\partial U_i}{\partial x_j} \qquad 2.6$$

Equation 2.2 is now

$$\underset{\text{I}}{\frac{\partial Q^2}{\partial t}} = \underset{\text{II}}{-\frac{U_i}{\bar{\rho}} \frac{\partial \bar{P}}{\partial x_i}} \underset{\text{IIIa}}{-\frac{\partial U_i Q^2}{\partial x_i}} \underset{\text{IIIb}}{-\frac{\partial U_i \overline{u_i u_j}}{\partial x_j}} \underset{\text{IV}}{+\overline{u_i u_j} \frac{\partial U_i}{\partial x_j}} \qquad 2.7$$

For the meanings of the individual terms in equation 2.7 we have:

I The local rate of change of average kinetic energy per unit mass, for example a seasonal change.

II The rate of work done per unit mass by the pressure field. Measurements of the anomaly of dynamic height and the average velocity along the equator permit the evaluation of this term.

IIIa Divergence of transport of kinetic energy per unit mass by the
IIIb average flow and the turbulent diffusion of average energy.

IV The rate of exchange of energy between the kinetic energy of the fluctuating motion and the kinetic energy of the average motion. It is the product of the Reynolds stress per unit mass $\overline{u_i u_j}$ and the average shear, $\partial U_i/\partial x_j$

A distinction has been made by Bowden (1962) between fluctuations due to turbulence and those due to two dimensional eddies. Turbulence is a term for random fluctuations of all three components of velocity, requiring a transfer of energy from large scales of motion to smaller scales and finally, at the smallest scales, the transfer of energy to heat. Turbulence is always a sink for kinetic energy of the mean flow, and causes mixing. Large scale two dimensional eddies (or meanders) are often found in the ocean or atmosphere, may either extract energy from or contribute energy to the mean flow and need not cause vertical mixing. The contribution of both of these interactions to the kinetic energy of the average flow is represented by term IV.

Estimates of some of the terms in equation 2.7 are available from observations during GATE, and will be discussed in section 4. Term I may be estimated, as well as the zonal components of terms II and IIIa. Regions can be chosen over which the contributions of other divergence terms are small. However, there are no measurements in equatorial regions of term IV in equation 2.7. It is possible, however, to evaluate some terms in the kinetic energy equation for the fluctuating flow. The term $\overline{u_i u_j}\frac{\partial U_i}{\partial x_j}$ appears in this equation as a source of kinetic energy of turbulent fluctuations, and as a source or sink of kinetic energy of the two-dimensional eddies. If other terms in the equation are measured or small, the term

$\overline{u_i u_j}\frac{\partial U_i}{\partial x_j}$ may be deduced.

2.3 Energy Balance for the Fluctuating Flow

The equation for the kinetic energy of a constant density, fluctuating flow can be derived in a way similar to that of the equation for the average flow. The Navier-Stokes equation is multiplied by U_i, averaged and summed. The equation in tensor form is (Hinze, 1959, p. 65):

$$\underset{\text{I}}{\frac{dq^2}{dt}} = \underset{\text{II}}{-\frac{\partial}{\partial x_i}\overline{u_i\left(\frac{p'}{\rho}+q^2\right)}} \underset{\text{III}}{-\overline{u_i u_j}\frac{\partial U_i}{\partial x_j}} \underset{\text{IV}}{+\nu\frac{\partial}{\partial x_i}\overline{\left(u_j\left(\frac{\partial u_i}{\partial x_j}+\frac{\partial u_j}{\partial x_i}\right)\right)}} \underset{\text{V}}{-\nu\overline{\left(\frac{\partial u_i}{\partial x_j}+\frac{\partial u_j}{\partial x_i}\right)\frac{\partial u_j}{\partial x_i}}} \qquad 2.8$$

where

$$q^2 = \frac{\overline{u_i u_i}}{2} = \frac{1}{2}\left[\overline{u_1^2}+\overline{u_2^2}+\overline{u_3^2}\right] \qquad 2.9$$

is the kinetic energy per unit mass of the fluctuating motion.

Equation 2.8 states that the rate of change (I) of kinetic energy of the fluctuating motion per unit mass of the fluid following the mean motion (i.e., $\frac{\partial q^2}{\partial t}+U_j\frac{\partial q^2}{\partial x_j}$) is equal to (II) the convective diffusion by the fluctuating motion of the total energy of the fluctuating motion, plus (III) the energy transferred to or from the mean motion through the stresses of the fluctuating motion, plus (IV) the work done per unit mass and time by the viscous stresses of the fluctuating motion, plus (V) the dissipation per unit mass of the fluctuating motion (Hinze, 1959). As shown by Tennekes and Lumley (1972, p. 70), term IV is of order (Reynolds number)$^{-1}$ times term V and may be neglected.

The last term is frequently written

$$-\nu\overline{\left(\frac{\partial u_i}{\partial x_j}+\frac{\partial u_j}{\partial x_i}\right)\frac{\partial u_j}{\partial x_i}} = -\frac{\nu}{2}\overline{\left(\frac{\partial u_i}{\partial x_j}+\frac{\partial u_j}{\partial x_i}\right)^2} = -\bar{\epsilon} \qquad 2.10$$

which shows that the viscous dissipation term $-\bar{\epsilon}$ in equation 2.8 is always negative definite, and always decreases the value of q^2, converting the kinetic energy into heat.

The presence of small density variations alters the form of equation 2.8. As was noted for the equation of the kinetic energy of the average flow, the Boussinesq approximation is valid for the undercurrent. When the density field is portioned into mean and fluctuating components, and the Boussinesq approximation applied, the density ρ may be replaced by the average density $\bar{\rho}$ in equation 2.8, (however, it must be outside the derivative) and an extra term $-\overline{\rho' u_3} g/\bar{\rho}$ is added to the right side of the equation (van Mieghem, 1973).

In the presence of density variations, $-\rho' g/\bar{\rho}$ is the buoyancy force per unit mass acting on a fluid element, and $-\overline{\rho' u_3} g/\bar{\rho}$ is the average work done per unit mass by the buoyancy force. In a stably stratified fluid, this term is negative, indicating that kinetic energy is lost to the potential energy field. When the stratification is unstable, kinetic energy may be gained from the potential energy field, and this term is positive (Monin and Yaglom, 1971, p. 397).

The equation for the kinetic energy per unit mass of the fluctuating velocity is now

$$\underset{\text{I}}{\frac{dq^2}{dt}} = \underset{\text{II}}{-\frac{1}{\bar{\rho}}\frac{\partial \overline{u_i p'}}{\partial x_i}} \underset{\text{III}}{-\frac{\partial}{\partial x_i}\left(\overline{u_i q^2}\right)} \underset{\text{IV}}{-\overline{u_i u_j}\frac{\partial U_i}{\partial x_j}} \underset{\text{V}}{-\bar{\epsilon}} \underset{\text{VI}}{-\overline{\rho' u_3} g/\bar{\rho}} \qquad 2.11$$

The fluctuating components considered here include the meanders, tides, internal waves, and turbulence. The expected effect of the meanders has been discussed; the tides and internal waves can transmit energy from

one region to another, and can carry energy into and out of a region. However, unless they interact with turbulence or generate instabilities they are not very dissipative, and do little mixing (for a wave an excellent approximation is $\overline{u_i u_j} = 0$ for $i \neq j$); hence their contributions to terms V and VI are small. To produce large values of $\bar{\epsilon}$, turbulence is required. The evaluation of terms II and III is difficult, and has not been attempted for oceanic turbulence. There are no measurements of term IV, as mentioned in the previous section, and no measurements for term VI.

With such a dearth of measurements, one is forced to some assumptions. In the Introduction it was noted that the viscous dissipation of turbulent energy was an important sink for the kinetic energy of the average flow. This energy is passed from the average flow to the turbulence through term IV, which appears in equation 2.7 and equation 2.11. There are no equatorial measurements of term IV, but I will show in section 4 that it is similar to $\bar{\epsilon}$ in regions of relatively intense turbulence at the equator, and $\bar{\epsilon}$ can be estimated from the velocity microstructure measurements.

To determine the dissipation, the degree of isotropy must be known because it is not possible to measure all the terms in the expression for $\bar{\epsilon}$ (equation 2.10). In flows of large Reynolds numbers, there may be several orders of magnitude difference in the size of scales at which turbulent energy is generated from the mean flow and the scales at which it is converted to heat by the viscous forces. In such cases Kolmogoroff first proposed in 1941 that there is a tendency for flows at small scales where viscous dissipation occurs to become isotropic, a condition termed local isotropy. In this case (Monin and Yaglom, 1975, p. 353-354):

$$\bar{\epsilon} = 15\nu\overline{\left(\frac{\partial u_1}{\partial x_1}\right)^2}$$

$$= \frac{15}{2}\nu\overline{\left(\frac{\partial u_1}{\partial x_3}\right)^2} \qquad 2.12a$$

Thus measurements of a single gradient at small scales will give the full value of the dissipation. Writing out $\bar{\epsilon}$ in full from equation 2.10 we have

$$\frac{\bar{\epsilon}}{\nu} = \frac{1}{2}\overline{\left(\frac{\partial u_i}{\partial x_j} + \frac{\partial u_j}{\partial x_i}\right)^2}$$

$$= \overline{\left(\frac{\partial u_1}{\partial x_1}\right)^2} + \overline{\left(\frac{\partial u_2}{\partial x_2}\right)^2} + \overline{\left(\frac{\partial u_3}{\partial x_3}\right)^2}$$

$$+\overline{\left(\frac{\partial u_1}{\partial x_2} + \frac{\partial u_2}{\partial x_1}\right)^2} + \overline{\left(\frac{\partial u_2}{\partial x_3} + \frac{\partial u_3}{\partial x_2}\right)^2} + \overline{\left(\frac{\partial u_3}{\partial x_1} + \frac{\partial u_1}{\partial x_3}\right)^2} \qquad 2.12b$$

In the isotropic case

$$\overline{\left(\frac{\partial u_1}{\partial x_1}\right)^2} = \overline{\left(\frac{\partial u_2}{\partial x_2}\right)^2} = \overline{\left(\frac{\partial u_3}{\partial x_3}\right)^2}$$

and terms like

$$\overline{\left(\frac{\partial u_1}{\partial x_3}\right)^2} = 2\overline{\left(\frac{\partial u_1}{\partial x_1}\right)^2}$$

and cross terms like

$$2\,\overline{\frac{\partial u_3}{\partial x_1}\frac{\partial u_1}{\partial x_3}} = -\overline{\left(\frac{\partial u_1}{\partial x_1}\right)^2}$$

The instrumentation we used at the equator (and described in section 3) measures $\frac{\partial u_1}{\partial x_3}$ and $\frac{\partial u_2}{\partial x_3}$ directly (although some corrections must be made of small scale resolution limits of the probe). Thus in the isotropic case, the sum of the quantities measured is $\frac{4}{15}\bar{\epsilon}$. *Isotropy is needed only when we* convert what we measure to an estimate of the total dissipation. Note that even if the turbulence is anisotropic we are measuring directly terms which make a large contribution to $\bar{\epsilon}$, since equation 2.10 is a general relation not dependent on isotropy.

2.4 Spectral Representation of Turbulence

Some checks of local isotropy may be made using the spectral representation of turbulence. G.I. Taylor first introduced the energy density function to describe the concept of energy in turbulence associated with a scale size. I will use the notation E(k) to denote the three dimensional energy density function; E(k)dk denotes the energy of all fluctuations having a wavenumber magnitude between k and k+dk. The one dimensional spectral function $\Phi_{11}(k_1)$ denotes the energy density of the u_1 component of velocity associated with all fluctuations having a wavenumber component k_1 in the x_1 direction, and $\Phi_{22}(k_1)$ is the energy density of the u_2 component of velocity associated with all fluctuations having a wavenumber component k_1 in the x_1 direction. The three velocities are related to the spectral functions by

$$\int_0^\infty E(k)\,dk = \frac{1}{2}(\overline{u_1^2} + \overline{u_2^2} + \overline{u_3^2}) \qquad 2.13$$

$$\int_0^\infty \Phi_{11}\,dk_1 = \overline{u_1^2} \qquad 2.14$$

$$\int_0^\infty \Phi_{22}\,dk_1 = \overline{u_2^2} \qquad 2.15$$

$$\int_0^\infty \Phi_{33}\,dk_1 = \overline{u_3^2} \qquad 2.16$$

In a locally isotropic region of wavenumber space one finds (Monin and Yaglom, 1975, p. 54):

$$E(k) = \frac{k_1^2}{2}\frac{\partial^2 \Phi_{11}(k_1)}{\partial k_1^2} - \frac{k_1}{2}\frac{\partial \Phi_{11}(k_1)}{\partial k_1} \qquad 2.17$$

$$\Phi_{22}(k_1) = \frac{1}{2}\left[\Phi_{11}(k_1) - \frac{k_1\,\partial \Phi_{11}(k_1)}{\partial k_1}\right] = \Phi_{33}(k_1) \qquad 2.18$$

and also

$$\varphi_{12}(k_1) = 0 \qquad 2.19$$

where $\varphi_{12}(k_1)$ is the spectrum of $\overline{u_1 u_2}$ associated with a wavenumber k_1 such that

$$\int_0^\infty \varphi_{12}(k_1)\,dk_1 = \overline{u_1 u_2} \qquad 2.20$$

Equations 2.17 to 2.19 are necessary (but not sufficient) conditions for the presence of isotropy at the scale size corresponding to the wavenumber k_1. Theories of isotropic turbulence are generally expressed in terms of E(k) which cannot be measured. Measurements of turbulence usually sense components leading to estimates of $\varphi_{11}(k_1)$, $\varphi_{22}(k_1)$ or $\varphi_{12}(k_1)$, which are compared with theoretical relationships through equations 2.17 to 2.19. The viscous dissipation for locally isotropic turbulence is

$$\bar{\epsilon} = 2\nu \int_0^\infty k^2 E(k)\,dk \qquad 2.21$$

or, in terms of measured values of $\varphi_{11}(k_1)$ and $\varphi_{22}(k_1)$ is (Monin and Yaglom, 1975, p. 405):

$$\bar{\epsilon} = 15\nu \int_0^\infty k_1^2 \varphi_{11}(k_1)\,dk_1 = \frac{15}{2}\nu \int_0^\infty k_1^2 \varphi_{22}(k_1)\,dk_1 \qquad 2.22$$

The spectral representation can be used to check for local isotropy within the dissipation region and to determine the dissipation. A second advantage is that if the turbulence is locally isotropic, the form of the spectral density functions can be predicted, and conversely, if the shape of one of the $\varphi_{11}(k_1)$, $\varphi_{22}(k_1)$, $\varphi_{33}(k_1)$ curves is measured, then assuming isotropy, $\bar{\epsilon}$ can be determined without measurements at dissipation scales. These determinations rely upon the two Kolmogoroff hypotheses.

For large Reynolds numbers, Kolmogoroff proposed that the statistical properties of the flow at small scales are independent of the large scale flow, except for the average rate $\bar{\epsilon}$ at which energy is passed from the large scales to the smaller. These statistical properties will also depend upon the kinematic viscosity ν and the wavenumber k. A characteristic wavenumber can be formed from the viscosity and the dissipation

$$k_s = (\bar{\epsilon}\,\nu^{-3})^{1/4} \qquad 2.23$$

where k_s is the Kolmogoroff wavenumber. Dimensional analysis gives,

$$\Phi_{11}(k_1) = (\bar{\epsilon}\,\nu^5)^{1/4}\, F(k/k_s)$$

$$\Phi_{22}(k_1) = (\bar{\epsilon}\,\nu^5)^{1/4}\,\frac{1}{2}\left[F(k/k_s) - k_1\frac{\partial F(k/k_s)}{\partial k_1}\right] = (\bar{\epsilon}\,\nu^5)^{1/4}\, F_2(k/k_s) \qquad 2.24$$

Both $F(k/k_s)$ and $F_2(k/k_s)$ are functions of the universal non-dimensional wavenumber (k/k_s). (The subscript is traditionally omitted from the wavenumber k_1 within the brackets but it is understood that this is k_1, not the magnitude of the vector wavenumber.) The dissipation spectra are

$$k_1^2\,\Phi_{11}(k_1) = k_s^2\,(\bar{\epsilon}\,\nu^5)^{1/4}\, G(k/k_s) \qquad 2.25$$

$$k_1^2\,\Phi_{22}(k_1) = k_s^2\,(\bar{\epsilon}\,\nu^5)^{1/4}\, G_2(k/k_s) \qquad 2.26$$

where

$$G(k/k_s) = \frac{k_1^2}{k_s^2}\, F(k/k_s) \qquad 2.27$$

and

$$G_2(k/k_s) = \frac{k_1^2}{k_s^2}\, F_2(k/k_s) \qquad 2.28$$

are also universal non-dimensional spectra.

For yet larger Reynolds numbers, the second Kolmogoroff hypothesis proposes that only $\bar{\epsilon}$ and k are the relevant parameters within a locally isotropic inertial subrange. Scales within this subrange are too small to be directly influenced by the mean flow, and too large to be influenced by viscosity. Dimensional analysis gives

$$\varphi_{11}(k_1) = K' \bar{\epsilon}^{2/3} k_1^{-5/3} \qquad \text{and using 2.18} \qquad 2.29$$

$$\varphi_{22}(k_1) = \frac{4}{3} \varphi_{11}(k_1) \qquad 2.30$$

where K' is a universal constant. A summary by Monin and Yaglom (1975) of experiments gives $K' = 0.5$ as the most reasonable value suggested by experimental data. Oceanic work by Nasmyth (personal communication) gives $K' = 0.52$. The log $F(^k/k_s)$ curve derived by Nasmyth (personal communication) from a re-evaluation of his work reported earlier (Nasmyth, 1970) is shown in figure 5. The log $F_2(^k/k_s)$ curve, calculated from data for the log $F(^k/k_s)$ curve using equation 2.24 is shown alongside. Values of log $G(k/k_s)$ and $G_2(k/k_s)$ have been calculated from the log $F(k/k_s)$ curve using equations 2.27 and 2.28 and are also plotted in figure 5.

To determine $\bar{\epsilon}$ accurately from spectra the turbulence must be locally isotropic at least through the dissipation portion of the spectrum, and the Kolmogoroff hypotheses must be followed for the portion of the spectrum sensed. It is known that the $\varphi_{11}(k_1)$ spectrum often follows a -5/3 power dependence upon k_1 at wavenumbers where the turbulence is anisotropic (e.g., Weiler and Burling, 1967) and care must be taken in analyzing the results. If the fluid is stratified, buoyancy effects may influence the spectra.

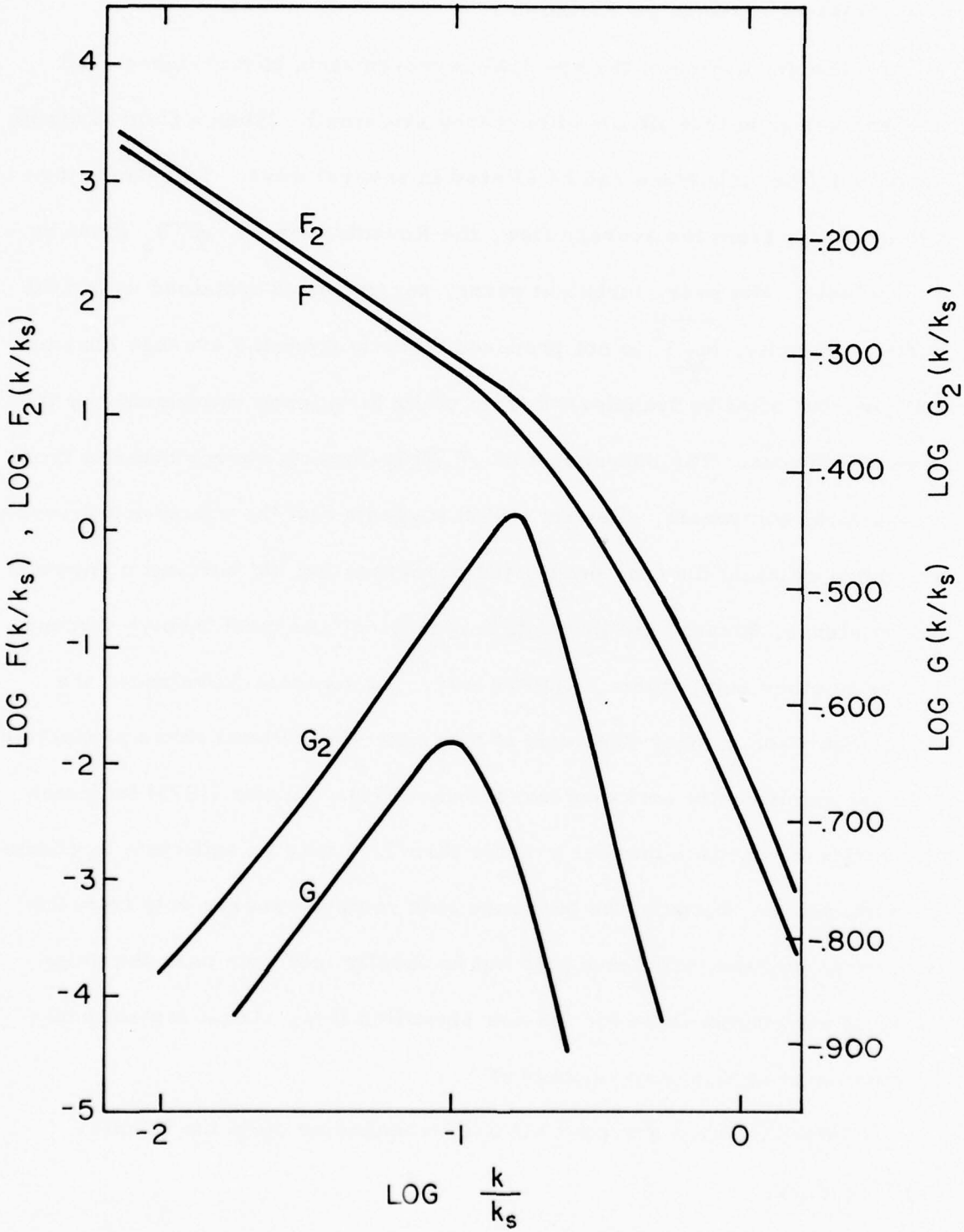

Figure 5 Universal curve of log $F(k/k_s)$ (from Nasmyth, personal communication) and derived curves of log $F_2(k/k_s)$, log $G(k/k_s)$ and log $G_2(k/k_s)$.

2.5 Buoyancy Effects on Turbulence

The discussion of the spectral representation of turbulence until now has assumed that effects of buoyancy are small. When a fluid is stably stratified, the turbulence can be altered in several ways. To extract turbulent energy from the average flow, the Reynolds stress $-\rho\overline{u_1 u_3}$ must be appreciable. However, turbulent energy per unit mass contained within the vertical velocity, $\frac{\overline{(u_3)^2}}{2}$ is not produced directly from the average horizontal flow, but must be transferred from other turbulence components by the pressure forces. The buoyancy sink $-\overline{u_3\rho'}g/\bar{\rho}$ extracts energy directly from the vertical component. Stewart (1959) suggests that the extraction processes are more efficient than the production processes for the vertical component of turbulence, because the production is indirect and must involve viscous losses in other components along the way. To maintain turbulence, the flux Richardson number (the ratio of buoyancy sink to total shear production) must be significantly less than one (Pond, 1973). Turner (1973) indicates that a flux Richardson number greater than 0.15 may be sufficient to eliminate turbulence. Because the buoyancy sink removes energy only from the u_3 component, the turbulence may not be locally isotropic over the same range of wavenumbers as for the non-stratified flow. Local isotropy may only be found at higher wavenumbers.

Internal waves are possible with frequencies up to the Brunt-Väisälä frequency,

$$N = \left(\frac{-g}{\rho}\frac{\partial \rho}{\partial x_3}\right)^{1/2} \qquad 2.31$$

These waves may contribute energy to the φ_{11}, φ_{22} and φ_{33} spectra at

low frequencies. These effects are discussed by Stewart (1969). Internal waves in a laminar flow can interact to generate patches of turbulence. Patches of turbulence can lose energy to internal waves which radiate energy away.

There is some evidence that for turbulence of sufficiently high Reynolds numbers, stable stratification influences the energy density spectra only at wavelengths greater than some value ℓ_b. Turbulent fluctuations of wavelengths less than ℓ_b may not feel the large scale stratification, and may be locally isotropic. In a stably stratified atmospheric boundary layer, experiments have found evidence consistent with local isotropy for values of $fL/U \approx 10$ ($\lambda \approx 0.1L$) (Kaimal et al, 1972) where L is the Monin-Obukhov length and λ is the wavelength. Away from the surface in the atmosphere or ocean, the length L is no longer the relevant length scale, and various other scales have been proposed. Ozmidov (1965) has proposed the criterion

$$\ell_b = \bar{\epsilon}^{1/2} N^{-3/2} \qquad 2.32a$$

and Obukhov (1959) has suggested the length scale for regions where temperature fluctuations dominate the density fluctuations should be

$$\ell_b' = \bar{\epsilon}^{5/4} / (\Theta^{3/4} (g/T_o)^{3/2}) \qquad 3.32b$$

where $\Theta = \kappa_T \overline{(\nabla T')^2}$ is the rate of dissipation of temperature fluctuations, κ_T is the molecular diffusivity for heat and T_o is the average temperature in degrees Kelvin. Unfortunately there have been no rigorous tests of isotropy using the criteria of equations 2.17 to 2.19, although several investigators have observed a $k^{-5/3}$ power law dependence for $\varphi_{11}(k_1)$ or

$\varphi_{33}(k_1)$: (Shur, 1962, Vinnichenko, 1969, for clear air turbulence in the atmosphere; Seitz, 1973, for turbulence in an estuary; Belyaev, et al, 1975a, for turbulence in the ocean). Measurements by Nasmyth (1970) of patches of turbulence in the winter thermocline in the North Pacific Ocean revealed that the $\varphi_{11}(k_1)$ spectra did not conform to a universal Kolmogoroff spectrum even for scales in the viscous dissipation region.

If the turbulence in the dissipation range is anisotropic due to stable density gradients, u_3 may not be suppressed completely, or there would be no turbulence. However, if u_3 tends to zero, but the isotropic relations hold for u_1 and u_2, then $\bar{\epsilon} = 15\overline{\left(\frac{\partial u_1}{\partial x_3}\right)^2}$; that is, the true dissipation would be $^{11}/15$ of the value estimated from the measurements using the isotropic relation. The situation cannot be this extreme, although in the anisotropic case $\frac{\partial u_1}{\partial x_3}$ and $\frac{\partial u_2}{\partial x_3}$ may become somewhat larger relative to terms like $\frac{\partial u_1}{\partial x_1}$, etc. It appears that an estimate of the rate of dissipation based upon our measurements of $\frac{\partial u_1}{\partial x_3}$ and $\frac{\partial u_2}{\partial x_3}$ and assuming isotropy may overestimate $\bar{\epsilon}$ by almost 50% in the most extreme case, but likely the error is smaller.

2.6 Observations of Oceanic Turbulence

To measure any of the terms in the expression for $\bar{\epsilon}$ (equation 2.10) velocity gradients at scale sizes at which viscous dissipation takes place must be resolved. The Kolmogoroff wavenumber $k_s = (\bar{\epsilon}\ \nu^{-3})^{\frac{1}{4}}$, and the corresponding Kolmogoroff wavelength $\lambda_s = 2\pi/k_s$ characterize the wavenumbers and wavelengths at which the rate of viscous dissipation is high. For turbulence which is locally isotropic at dissipation scales, the peak of the dissipation spectrum $G(k/k_s)$ is near a wavenumber $k=0.1k_s$. (Pond, 1965.) Oceanic turbulence has a dissipation spectrum extending from small scales of 1 to 6 cm (Gregg, 1973), up to about 1 metre, and velocity fluctuations at these wavelengths are referred to as velocity microstructure. The intensity of the microscale velocity gradients can often be used as a qualitative indicator of the intensity of turbulence (i.e., the intensity of the large scale energy containing fluctuations) because the small scale fluctuations can adapt quickly to changes of the large scales, and increase in amplitude as the large scale fluctuations increase in amplitude.

Observations by Grant et al.(1962) in a tidal channel in British Columbia revealed very active turbulence by using a hot film probe towed behind a ship. They measured values of $\bar{\epsilon}$ from 0.01 to 1 $cm^2 sec^{-3}$ and found an extensive minus five thirds region in the spectrum of $\Phi_{11}(k_1)$. Reynolds numbers in the channel are as high as 3×10^8. Later observations by Grant et al. (1968) in the open ocean show that in the upper mixed layer measurable turbulence is almost always found. In and below the thermocline, the fraction of the water which has measurable turbulence is small, often less than 10%. Average values of $\bar{\epsilon}$ in the upper mixed layer were

0.025 $cm^2 sec^{-3}$, and about two orders of magnitude less than 90 metres depth.

Nasmyth (1970) obtained measurements of turbulence in the winter thermocline in the North Pacific which reveal patchiness of the turbulence. He towed the hot film probe used by Grant et al. (1962, 1968) through the ocean, but added a cycling mode, whereby the probe could be alternately raised and lowered to sample along a sawtooth profile. Values of $\bar{\epsilon}$ ranged from about 2×10^{-2} to 2×10^{-4} $cm^2 sec^{-3}$ within the patches of turbulence, which occupied about 15% of the observed path during one set of observations, and 30% during another.

A free fall instrument used by Osborn (1974) to sense the $\varphi_{11}(k_3)$ and $\varphi_{22}(k_3)$ components of velocity microstructure in Howe Sound, British Columbia, revealed large variations in $\bar{\epsilon}$ over short distances. An examination of a typical 5 metre thick patch showed estimated dissipation there of about 3×10^{-4} $cm^2 sec^{-3}$.

Measurements of oceanic turbulence by Belyaev et al (1975 a, b) have revealed large changes in turbulent intensity in the horizontal and vertical, with the magnitude of $\bar{\epsilon}$ varying by a factor of 100.

Observations by Woods and Fosberry (1969) in the seasonal thermocline in the Mediterranean have revealed that shear instabilities can grow on a trough or crest of an internal wave propagating through a region. Shear instabilities grow from small disturbances which are able to extract energy from a larger scale shear, roll up into billows, eventually become gravitationally unstable and generate turbulence. These investigators noted that the instabilities grew on regions where the vertical density gradient

was large, called "sheets". The shear instabilities generated turbulence in patches, mixed the dye over a depth of up to 20 cm, and were smeared out along the sheet by the large scale shear.

Theoretical studies by Miles and Howard (1964) have shown that small disturbances will not grow in a laminar flow if the gradient Richardson number

$$Ri_g = \frac{-\frac{g}{\rho}\frac{\partial \rho}{\partial x_3}}{\left(\frac{\partial U_1}{\partial x_3}\right)^2} \qquad 2.33$$

is greater than $\frac{1}{4}$. The observations of Woods and Fosberry (1969) suggest that in and below the thermocline the average shear is too small to maintain turbulence, but that internal waves passing through can increase the shear in a region long enough to allow shear instabilities to grow and become turbulent. Measurements in the Atlantic by Sanford (1975) have shown that 10 m average values of Ri_g below the thermocline are greater than, but often close to 0.25. However, Sanford and also Stewart (1969) suggest that if there are non-uniform density and velocity gradients within the region, then the gradient Richardson number must be smaller for a portion of the region. For example, if within a 10 metre layer, the velocity and density gradients were concentrated within a few metres, the actual Richardson number would be much lower within these few metres than indicated by a 10 metre average gradient.

Thorpe (1973) found shear instabilities would grow and develop into turbulence in a tank only for values of Ri_g much less than 0.25. Recent

laboratory studies by Koop (1976) have shown shear instabilities to grow into billows for values of Ri_g less than about 0.07. For larger values, waves grew and their crests broke off and mixed into the flow. Orlanski and Bryan (1969) have proposed that internal waves may grow unstable and overturn much like plunging breakers on a beach. Garrett and Munk (1972) conclude that shear instabilities growing on internal waves are a more frequent source of turbulence than overturning internal waves, but they point out that a single overturning internal wave may generate much more turbulent kinetic energy than a single shear instability.

Double diffusion instabilities extract energy from the potential energy of the fluid to drive convective regimes. These have been summarized by Turner (1973) and Gregg (1973, 1975). When warm salty water overlies colder fresher water, salt fingering may be found. Williams (1974) observed such fingering below the Mediterranean outflow in the Atlantic, of scales about 6 mm in diameter and 24 cm high. When cold fresh water overlies warm salty water, layering may be found. Such layers have been observed for example in the Arctic by Neshyba and Neal (1971) and in several other oceanic regions. Thicknesses of the layers vary from less than a metre to up to 20 metres (Gregg, 1975). Although double diffusion regimes have been positively identified only in few regions, they may influence turbulence in much of the ocean. Gargett (1976) has noted that there is fairly strong statistical evidence for increased microstructure activity in regions where the local vertical gradients of temperature and salinity are suitable for double diffusion processes.

2.7 Observation in the Undercurrents

Measurements by Jones (1973) in the Pacific Equatorial Undercurrent show low values of the difference Richardson number (a finite difference approximation for Ri_g)

$$Ri_\Delta = \frac{-g}{\rho} \frac{\Delta\rho \Delta x_3}{(\Delta U)^2} \qquad 2.34$$

Values of Ri_Δ were less than one quarter over 5 to 10 metre depth intervals between 196 and 272 metres within the thermostad, which is a layer having a temperature from 11.5 to 13.5°C, located from about 100 to 300 metres below the surface. This layer is characterized by small changes in density, temperature and salinity with depth. It appears to increase in thickness, temperature and salinity as it flows from west to east, and may be formed by vertical or horizontal mixing. Jones feels that the low values of Ri_Δ indicate that vertical mixing should be more important.

Williams and Gibson (1974) have measured temperature fluctuations at microstructure scales in the Pacific Equatorial Undercurrent. From the wavenumber k_T at which the $\varphi_{TT}(k_1)$ vs log k_1 spectrum acquired a -1 slope, they calculate a viscous dissipation of 0.08 $cm^2 sec^{-3}$ at the Equator and at 1° North. These calculations require that conditions for Batchelor's (1959) theory for spectra of temperature fluctuations be met. However, studies by Gregg (1976) in the Pacific Equatorial Undercurrent do not show any good evidence of the turbulent subranges required for the Batchelor theory. He found values of the variance of temperature fluctuations appreciably lower than observed by Williams and Gibson.

Belyaev et al.(1975b) have reported values of $\bar{\epsilon}$ for the Atlantic

Equatorial Undercurrent. They observed velocity fluctuations at wavelengths longer than 2 cm ($k_1 \approx 3\ cm^{-1}$) and estimated values of $\bar{\epsilon}$. The values are high, ranging from about 0.027 to 0.34 $cm^2 sec^{-3}$ for horizontal samples. There is no significant depth variation of $\bar{\epsilon}$ over the depth range of 36 metres to 140 metres which they sampled. The turbulence is very intermittent, and Ozmidov (personal communication) has indicated that the values of $\bar{\epsilon}$ reported represent only the active regions, so the value of $\bar{\epsilon}$ averaged over all regions may be a factor of ten less.

Measurements of temperature and microstructure temperature gradients by Gregg (1976) at 155°W on the equator suggest that the most active turbulence was between 35 and 65 metres depth, which is above the velocity core, and that the turbulence intensity at the core is much less. The turbulence intensity and rate of dissipation are related; hence values of $\bar{\epsilon}$ where Gregg's data were collected would probably be relatively high above the core and relatively low in the core. The sensors employed by Gregg were a thermistor mounted on the nose of a free-fall instrument, and another on an outboard wing which rotated about the instrument. Comparison of temperature spectra from the two thermistors revealed that only in the thermostad is there a strong suggestion of local isotropy at microstructure scales.

3 EXPERIMENTAL APPARATUS AND PROCEDURE

3.1 Apparatus

The results obtained in this thesis are based mainly on measurements by a free-fall microstructure recording instrument during 1974. This instrument was built in 1971 and 1972 by Dr. T.R. Osborn and given the name "Camel". It was designed to measure velocity fluctuations in a column of water in the ocean, as well as temperature and conductivity variations. Early designs have been described by Osborn (1974) and Osborn and Siddon (1975).

The Camel (shown in figure 6) falls through the water with sensors in the nose to sample vertical profiles. The fall speed is 40 to 50 cm/sec and is controlled by adjusting the trimming weights and the release weights. The brushes at the upper end were added to increase form drag as the instrument fell. If a device such as a blunt collar were installed rather than brushes, the large eddies shed behind it could cause the instrument to wobble as it fell, and contaminate the velocity signal. A fall speed of 40 cm/sec is obtained when the Camel weighs 12 Newtons in seawater. Variation of density over the range encountered did not cause a significant change in terminal fall speed, although about 20 metres are required to reach this speed.

The weight release, recovery and communications systems have been described by Osborn and Siddon (1975). During a free-fall, signals are converted to standard IRIG FM frequencies, and transmitted up an XWL (an expendable wire length) to a tape recorder on board the work vessel. A set of FM discriminators and a chart recorder are used to obtain a

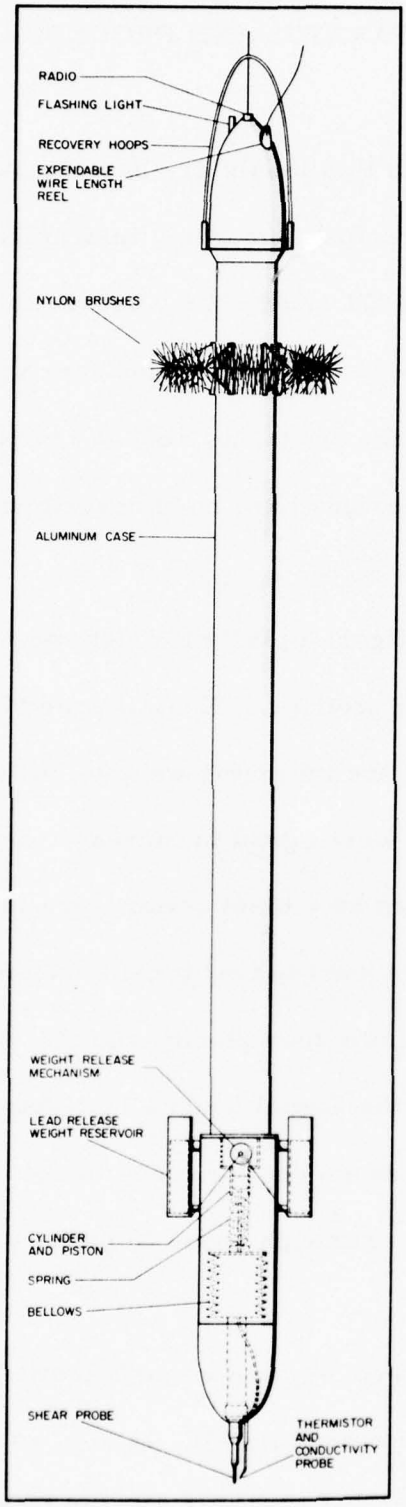

Figure 6 The Camel.

real time display during a free-fall. In 1974 the depth range of the Camel was limited to 450 metres by the XWL, but a modification of the XWL allowed depths of 800 m to be obtained on later cruises.

During free-fall, eight parameters were transmitted to the ship: temperature and its gradient, conductivity and its gradient, gradients of the two horizontal velocity components, pressure and orientation of the Camel relative to magnetic north. The shear, conductivity and temperature probes were located as shown in figure 6. The time gradients were obtained electronically within the Camel before transmission to the ship to improve the signal to noise ratio at high frequencies.

The method of obtaining the measurements is as follows:

Velocity

The main probe on the Camel is an airfoil velocity probe, used to sense horizontal velocities. Signals from the probe are differentiated to give vertical gradients (assuming Taylor's hypothesis, discussed below) of horizontal velocities, in other words, the shear. Accordingly, the probe is called a shear probe. The probe was developed by Siddon (1965, 1969) for studies of turbulence in wind tunnels. The modification for use in the ocean has been described by Osborn and Siddon (1975) and the use of the probe for studies of oceanic turbulence has been described by Osborn (1974). The calibration and testing of the shear probe is described briefly in the next few pages, and more detailed information is given in Appendix A.

The probe is of an axisymmetric shape, as shown in figure 7. It is mounted at the front of the Camel, which falls nearly vertically through the water. The expected tilts of the instrument are less than one degree, occur at low frequencies (Osborn, 1974) and will not interfere with the measurements of fluctuating velocities which are found in the dissipation range at higher frequencies. Water flows past the probe at a speed $\mathcal{U}$ at an angle of attack α; these depend on the fall speed of the Camel V, and the horizontal flow u relative to the Camel.

The sideways force on the probe is (Allen and Perkins, 1952):

$$F \approx \left(\tfrac{1}{2}\rho \mathcal{U}^2\right) A \sin 2\alpha = \rho \mathcal{U}^2 A \sin\alpha \cos\alpha \qquad 3.1$$
$$= \rho A V u$$

where

A is the effective area of the probe

ρ is the density of the fluid

V is the fall speed of the Camel

u is the horizontal velocity relative to the Camel

$\mathcal{U}^2$ is $(V^2 + u^2)$ (see figure 7)

The derivation, testing and limitations of this formula are described more fully in Appendix A.

The probe is constructed from a soft rubber compound and contains two piezoceramic bimorph beams mounted perpendicular to each other, as illustrated in figure 7. Much of the transverse force on the rubber mounting due to the flow is opposed by these beams which generate voltages proportional to the two components of bending moment.

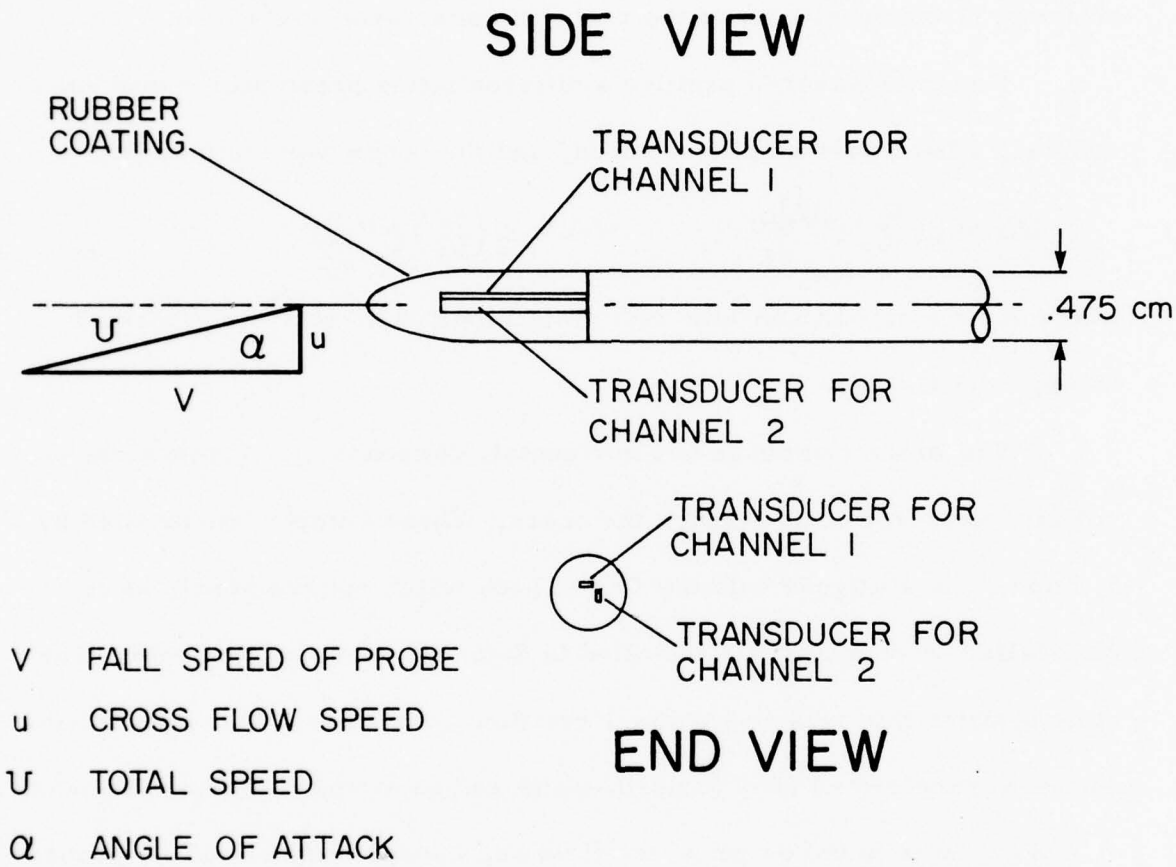

Figure 7 The shear probe.

To calibrate the probe, each voltage is sent to a preamplifier, and the voltage from each preamplifier is

$$v_{c1} = \frac{1}{2} S_1 \rho V u_1 \qquad v_{c2} = \frac{1}{2} S_2 \rho V u_2 \qquad 3.2$$

where S_i is the sensitivity of the probe in volts/(dyne/cm^2).

For the measured profiles a differentiating preamplifier was substituted, a band pass amplifier added, and the output voltage became

$$v_{D1} = \frac{1}{2}\left(\frac{S_1}{K_1}\right) \rho V \frac{du_1}{dt} \qquad v_{D2} = \frac{1}{2}\left(\frac{S_2}{K_2}\right) \rho V \frac{du_2}{dt} \qquad 3.2a$$

where K_i is a circuit constant with dimensions of (time)$^{-1}$ as explained in Appendix C.

The probe can sense two horizontal, perpendicular components of velocity as it free-falls through the ocean. These components denoted by u_1 and u_2, are aligned with the Camel body which rotates slowly as it free-falls. A compass was installed to determine the rotation rate. For most profiles this rate was below 1 rotation per minute. The signals have not been transformed back to north-south and east-west components; hence u_1 and u_2 refer to the output of the first and second channels of the probe preamplifier, and have an arbitrary orientation to the large scale flow, but this arbitrary co-ordinate system does not affect the results obtained.

The shear can be obtained with the use of Taylor's hypothesis, which is valid in this case (Osborn, 1974), by which spatial gradients can be derived from temporal variations sensed by the probe moving relative to the fluid at a speed V.

$$\frac{\partial}{\partial x_3} = -\frac{1}{V}\frac{\partial}{\partial t} \qquad 3.3$$

The equation 3.2 becomes, for the velocity components u_1 and u_2

$$\frac{\partial u_1}{\partial x_3} = \frac{-U_{01} K_1}{\frac{1}{2} S_1 \rho V^2} \qquad \frac{\partial u_2}{\partial x_3} = \frac{-U_{02} K_2}{\frac{1}{2} S_2 \rho V^2} \tag{3.4}$$

where U_{01}, U_{02} are the output voltages to the chart recorders on board the ship (I have not included in these formulae the effects of the filters, but these effects are noted in Appendix C).

A rubber based compound, PRC- 1202-Q medium, was used in the probes. It has a hardness on the Shore A scale of about 40. A typical value of both S_1 and S_2 was 5.0×10^{-4} volts/(dynes/cm^2). Tests showed this sensitivity changed by about 1% per degree Celsius. There is also a pyroelectric effect in the probes by which a sudden change in temperature can induce a large voltage output from the beams. Because the signal is differentiated before transmission to the ship, it is the rate of change of voltage which is important. For these probes, a step change of 1° C produces a slow voltage change of 100 millivolts/sec which corresponds to a shear of 0.35 sec^{-1} at a fall speed of 40 cm/sec. However, the output signal is at frequencies low compared to those which dominate contributions to the velocity derivatives and the effect was reduced by a high pass filter in the amplifier (rated -3db at 1Hz) (A full description of the electronics for the shear signals is given in Appendix C). Additional digital filtering was performed later for regions of low turbulence intensity and large temperature changes to further reduce noise at frequencies below 1Hz, and so prevent leakage into the frequency band of interest when the Fourier transforms were computed (see Appendix B).

The small wavelength response is determined by the size of the probe. Siddon (1969) found no (i.e., <0.5db) attenuation due to spatial averaging of an earlier model of the probe for fluctuations of wavelengths longer than four times the effective length of the probe. Because the pressure forces are concentrated near the tip, the diameter is chosen as a measure of the effective length. However, probes used for our measurements (diameter 4.7 mm) were longer than the probes tested by Siddon relative to the diameter, and the effective length may be greater than the diameter. A spectral test for spatial resolution is discussed in section 4.

To determine the effect of high pressure upon the sensitivity of the probe, the Camel was launched with a bar in front of the shear probe to generate eddies. The Camel descended at a uniform rate, so the turbulence behind the bar would have been uniform with depth and much larger than in situ turbulence (the gain of the circuit was changed to avoid overloading). No change in output signal level from the shear probe with depth was observed, so it seems that the sensitivity is independent of depth.

Temperature

Temperature is sensed with a Thermometrics microbead thermistor which is nominally 0.013 cm in diameter, coated with 0.0016 cm of Paralene C to insulate the beads and wire leads from seawater. Tests in a flow of 125 cm/sec showed the response was reduced to half power at frequencies of 15 Hz (Lueck et al, 1976). They showed the response was

mainly determined by the coating of Paralene C which is a very good electrical and thermal insulator. Therefore, at slower fall speeds, the response time should not be much different. For the 40 cm/sec fall speed of the Camel, the half power wavelength is about 3 cm.

To resolve temperature microstructure, Gregg (1973) suggested that wavelengths of 1 cm should be resolved. This resolution could be achieved with these thermistors if the response function were known accurately, since it is a rather simple task to multiply the Fourier transform of the temperature gradient signal by the response function of the microbead to obtain the spectral form of the actual temperature gradient. This procedure has been used by various researchers to resolve the temperature microstructure, but one should know the response function of each individual thermistor. These response functions were not available for our measurements. Also, the noise level of the temperature gradient signal (.002°C/cm) may interfere with signal recovery.

Another factor, often neglected with these thermistors, is fouling by plankton. When using the response function of a thermistor to recover the temperature gradient between 3 and 1 cm, a small accumulation of plankton on the thermistor can change the response function, and introduce large errors in the calculated gradient. Fortunately, it has no effect on the average temperature. The Equatorial Atlantic waters are relatively clear of plankton. The temperature gradients are used only in a qualitative way in this thesis and plankton fouling presents no problem for this purpose. The gradient signals have not been corrected for

the signal attenuation at small wavelengths.

The thermistors were calibrated on board ship prior to use. Temperatures obtained from the thermistors used on the Camel matched those of the CTD within 0.5°C absolute, and their precision was 0.2°C over a range from 10°C to 26°C based upon comparisons from regions of small temperature change with depth.

Conductivity

A new conductivity probe was developed during 1973, based upon the design by C.S. Cox and M.C. Gregg at Scripp's Institute of Oceanography. (Gregg and Cox, 1971). It provides records of conductivity gradient in the microstructure range, but the conductivity itself showed a drift which was depth dependent. At the equator, conductivity is determined mainly by temperature, and the two signals for temperature and conductivity gradients are remarkably similar. Indeed, they are so similar that only the temperature gradient output, which has lower noise levels, will be shown in the discussion of the results.

The drift of output voltage of the conductivity probe with depth prevented an accurate determination of density from the temperature and conductivity signals. Any graphs of σ_T in later sections are derived only from the CTD data of Dr. Eli Katz.

Pressure

A vibrotron installed in the upper end cap measures static pressure as the Camel free falls. The frequency of a vibrating wire in the vibrotron varies about a standard IRIG frequency as the ambient pressure

alters the tension of the wire. A signal of this frequency is transmitted to the ship, giving depth.

The fall speed is computed by a computer program which rejects spikes in the digitized record, computes a linear fit to the data from successive 4 metre sections of data, and calculates the fall speed over the section. A detectable fall speed change (greater than 3%), likely due to a bubble in the conductivity bellows was observed only once at depths below 20 metres.

The vibrotrons are somewhat temperature sensitive, with the calibration curves shifting for changes in temperature. Two vibrotrons were used at separate times, and the maximum expected error in average fall speed due to this effect is 1%.

Direction

A flux gate type compass installed in the spring of 1974 measured the orientation of the Camel relative to magnetic north, and hence the orientation of the individual beams in the shear probe relative to magnetic north. The compass was mounted inside the Camel pressure case. Output was converted to an FM signal and transmitted to the ship with the other signals.

3.2 Procedure

The cruise tracks of the ATLANTIS II in June and July 1974 are shown in figure 8. The peculiar zig-zag pattern results from a combination of two types of measurements. The short paths across the equator are those followed when an instrumented "fish" was towed behind the ship. This device used by Dr. E. Katz sampled temperature, conductivity, and the two components of velocity in the horizontal. The long sections at 10°W, 16°W, 22°W, 28°W, 33°W are those of the hydrographic stations. The Camel was used on these sections, along with a CTD, Nansen or Atlas bottles, and current meters. The data to be shown here come from the sections at 28°W (profiles 20 and 22-25) and 33°W (profiles 28, 29) as well as one profile at 24°W (profile 18). For most Camel launches, a CTD profile and current meter profile were taken within a few hours near the same spot (within a few nautical miles). A current meter profile was not taken at 24°W.

The Camel samples from the surface to between 300 and 400 metres. Readings near the surface are often contaminated by oscillations of the Camel caused by the launching. Low noise measurements of velocity gradient begin between 8 to 20 metres depth. For a Camel launch, the ship drifted, with starboard side up-wind. The Camel was hoisted over the starboard side, lowered part way into the water, and released from the launching mechanism. The ship drifted during the free fall of the Camel to avoid cutting the XWL on the propellor. A radio on the Camel signalled its surfacing but the direction finder did not work well on the steel-hulled ship. The Camel was located visually by looking up-wind. Recovery of

the Camel was achieved by snapping a line onto the recovery hoops and hoisting the Camel on board.

There were twelve free falls of the Camel during the cruise. Those with reliable shear data are shown in section 4.

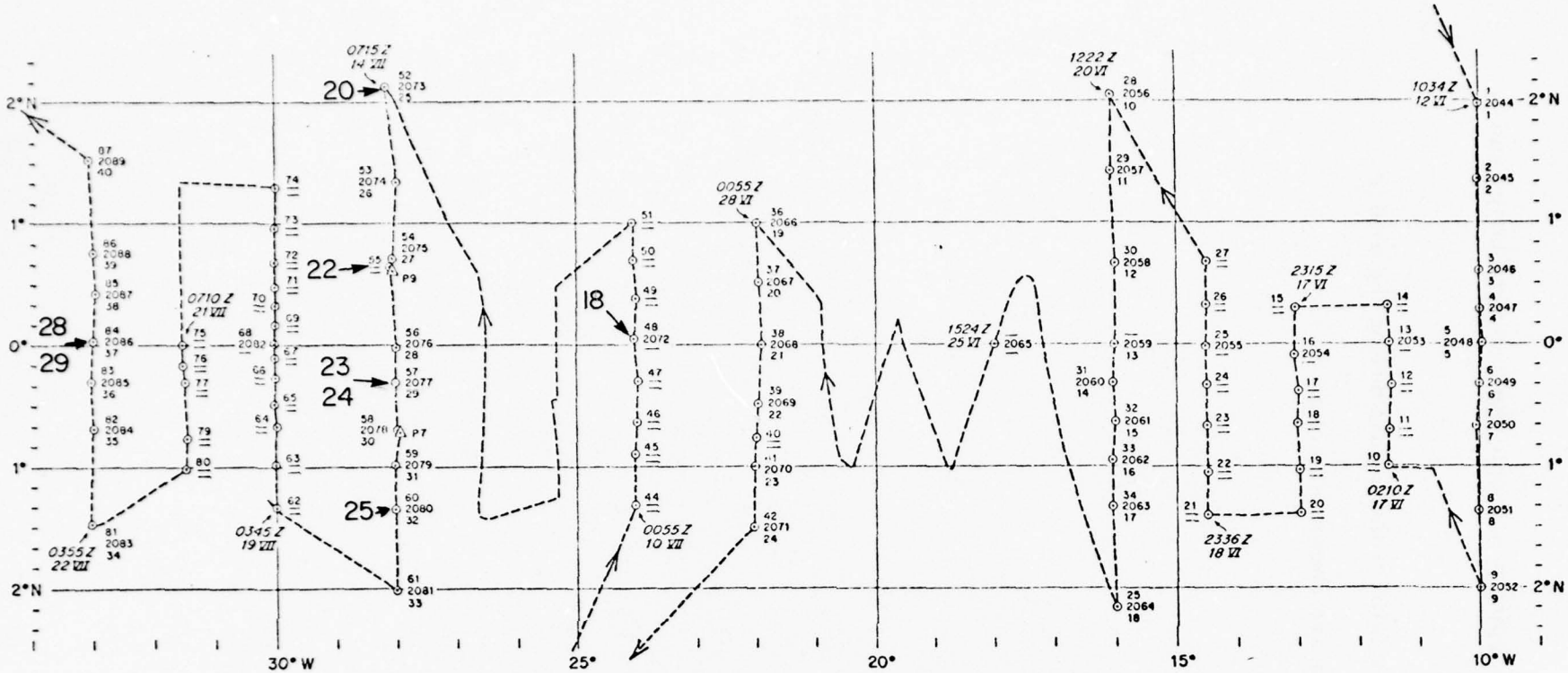

Atlantis II, cruise 83

June, July 1974

Legend

STD station number

⊙ Hydrographic station number

Current meter station number

note: Dash indicates no station

Figure 8 Cruise 83 of ATLANTIS II. The Camel profiles are indicated by arrows. (from Bruce and Katz, 1976)

Profile	Date	Longitude	Latitude
18	July 10	24°0'W	0°2'N
20	July 14	28°11'W	2°9'N
22	July 15	28°03'W	0°37'N
23	July 16	28°01'W	0°18'S
24	July 16	28°03'W	0°17'S
25	July 17	28°0'W	1°21'S
28	July 23	32°59'W	0°2'N
29	July 23	32°59'W	0°2'N

Table I Camel profiles during ATLANTIS II cruise

4 RESULTS

4.1 Qualitative Aspects of the Microstructure

Chart records of seven of the observed profiles are shown in figures 9 to 15. (A current meter profile was not taken near the location of profile 18, and this profile is omitted, although dissipations for profile 18 are shown later.) For these visual displays of the qualitative aspects, the traces of the gradients shown have not been corrected for the variations of the sensitivities of the probes with temperature, and for the variations in fall speed of the Camel. The sensitivity of the shear probe changes by $\pm 7\%$ over the range of temperature found through the profiles, being more sensitive in warmer waters near the surface. The thermistors are more sensitive to temperature gradients in colder waters at depth, changing by +4%. Fall speed changes below 20 metres depth are less than 3%, except for profile 24 where an increase of 7% in the fall speed was found between the depths of 20 and 160 metres.

The shear signals have been band passed between 1 and 18 Hz (40 and 2 cm) to reduce both low and high frequency noise in the visual displays of figures 9-17. (These filters are in addition to the filters in the electronics, described in Appendix C.) The temperature gradients are limited by the response of the thermistor to wavelengths greater than about 3 cm, and have no low frequency (low wavelength) filtering. The temperature signals have been low passed with a 1 Hz filter to reduce noise. Both temperature and temperature gradient signals are derived from the same probe. Note that both shear and temperature gradient

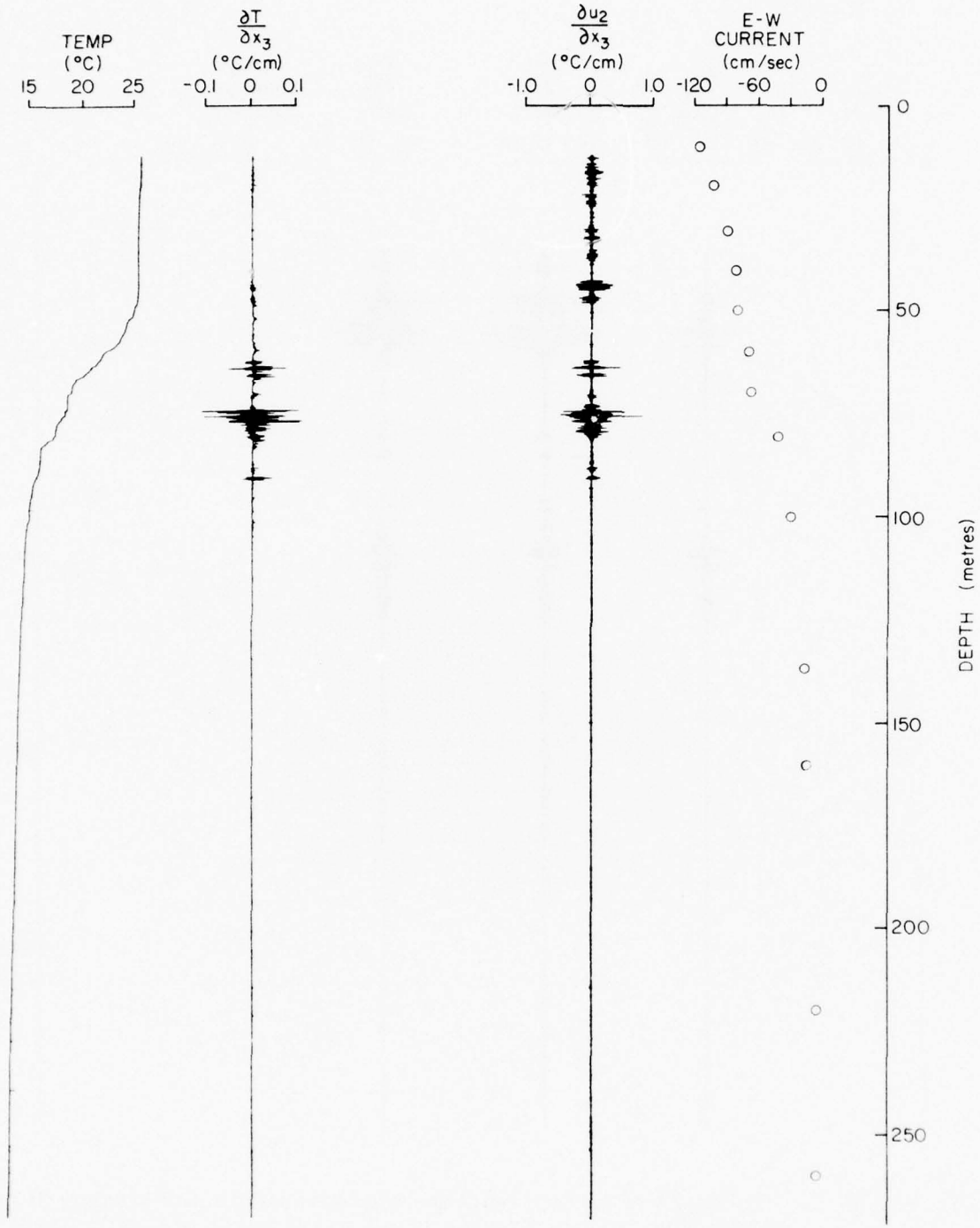

Figure 9 Profile 20 of microstructure measurements and temperature at 28°11'W, 2°9'N and the large scale current profile measured by J. Bruce.

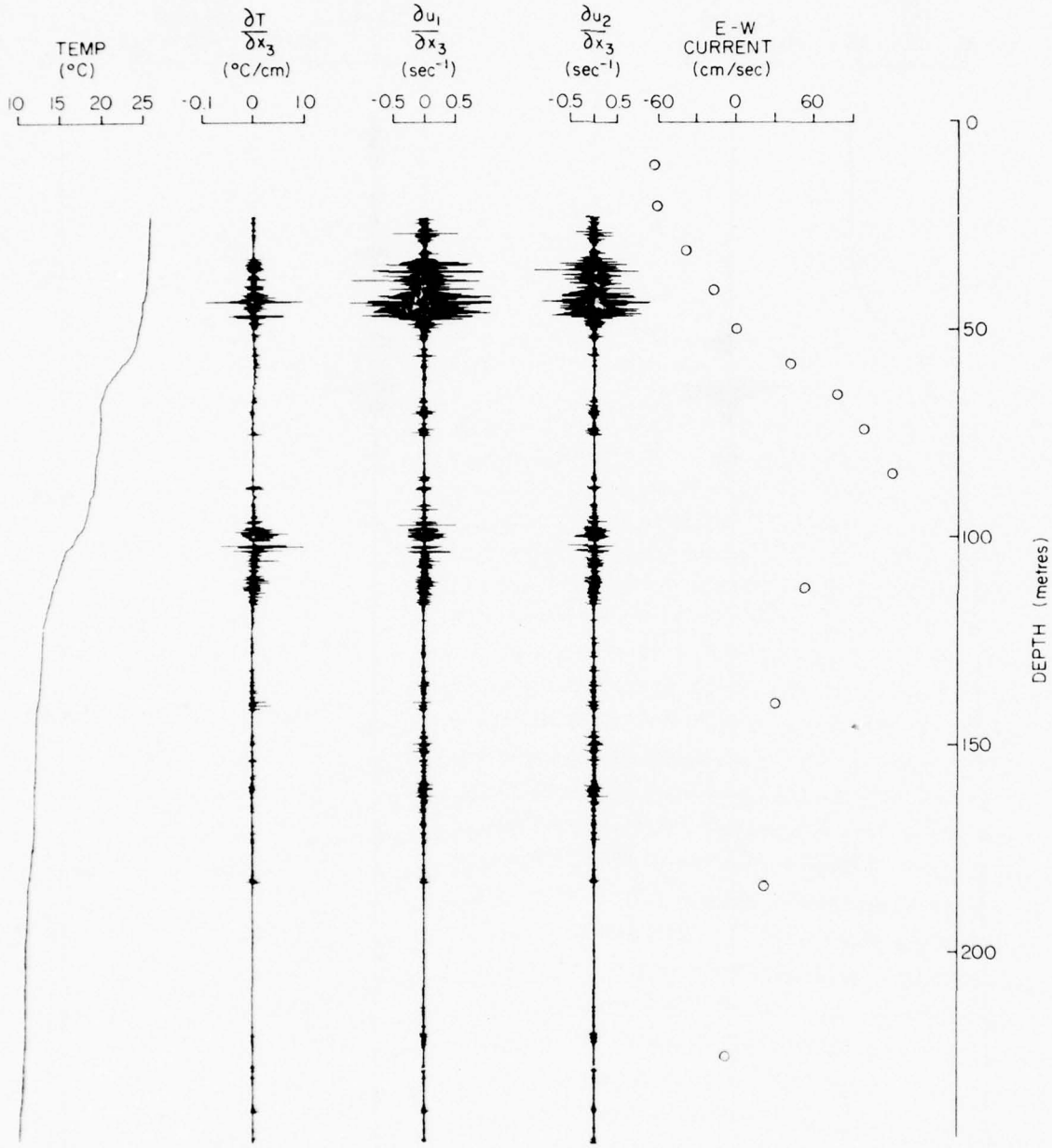

Figure 10 Profile 22 of microstructure measurements and temperature at 28°03'W, 0°37'N and the large scale current profile measured by J. Bruce.

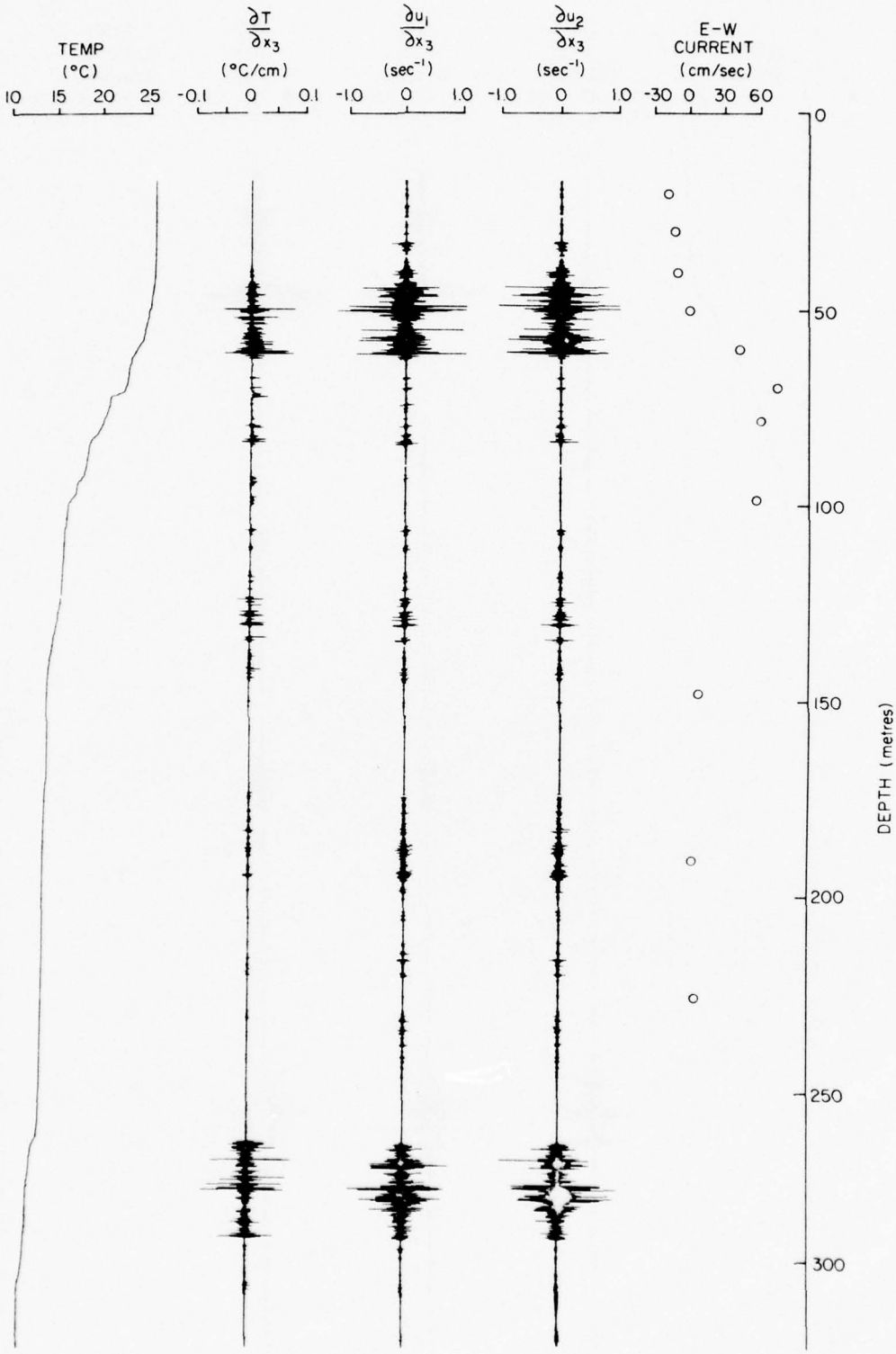

Figure 11 Profile 23 of microstructure measurements and temperature at 28°01'W, 0°18'S and the large scale current profile measured by J. Bruce.

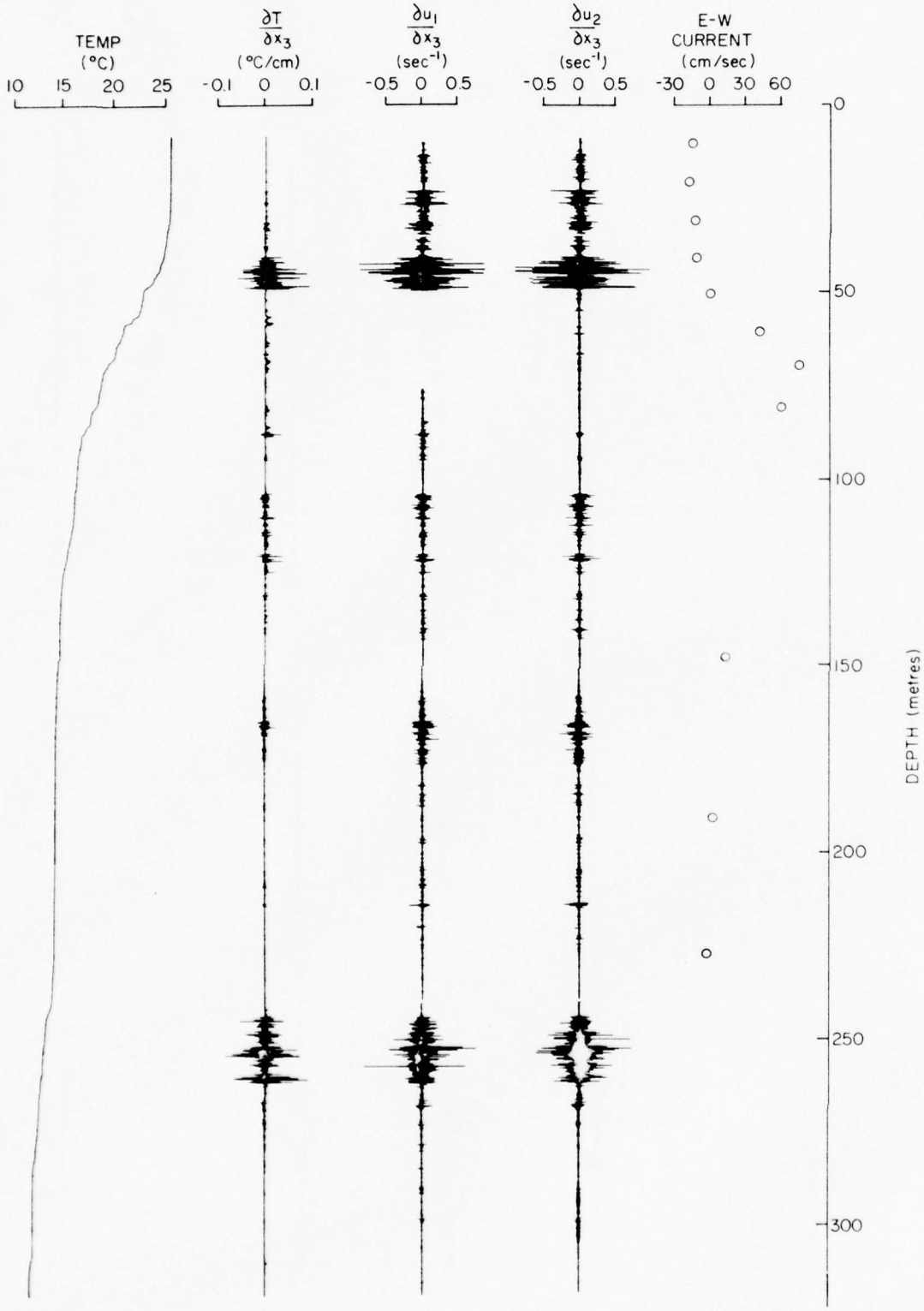

Figure 12 Profile 24 of microstructure measurements and temperature at 28°03'W, 0°17'S and the large scale current profile measured by J. Bruce.

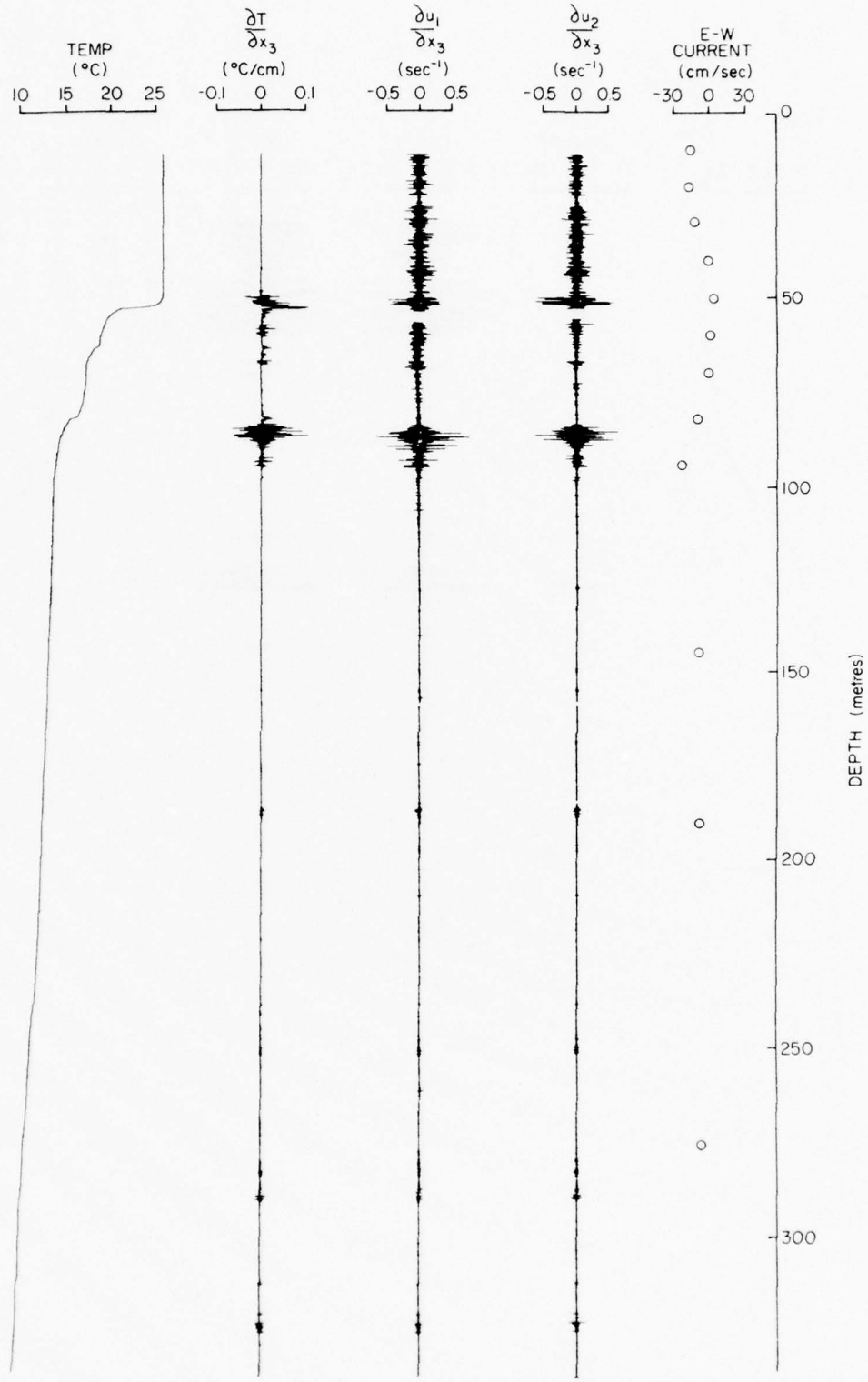

Figure 13 Profile 25 of microstructure measurements and temperature at 28°0'W, 1°21'S and the large scale current profile measured by J. Bruce.

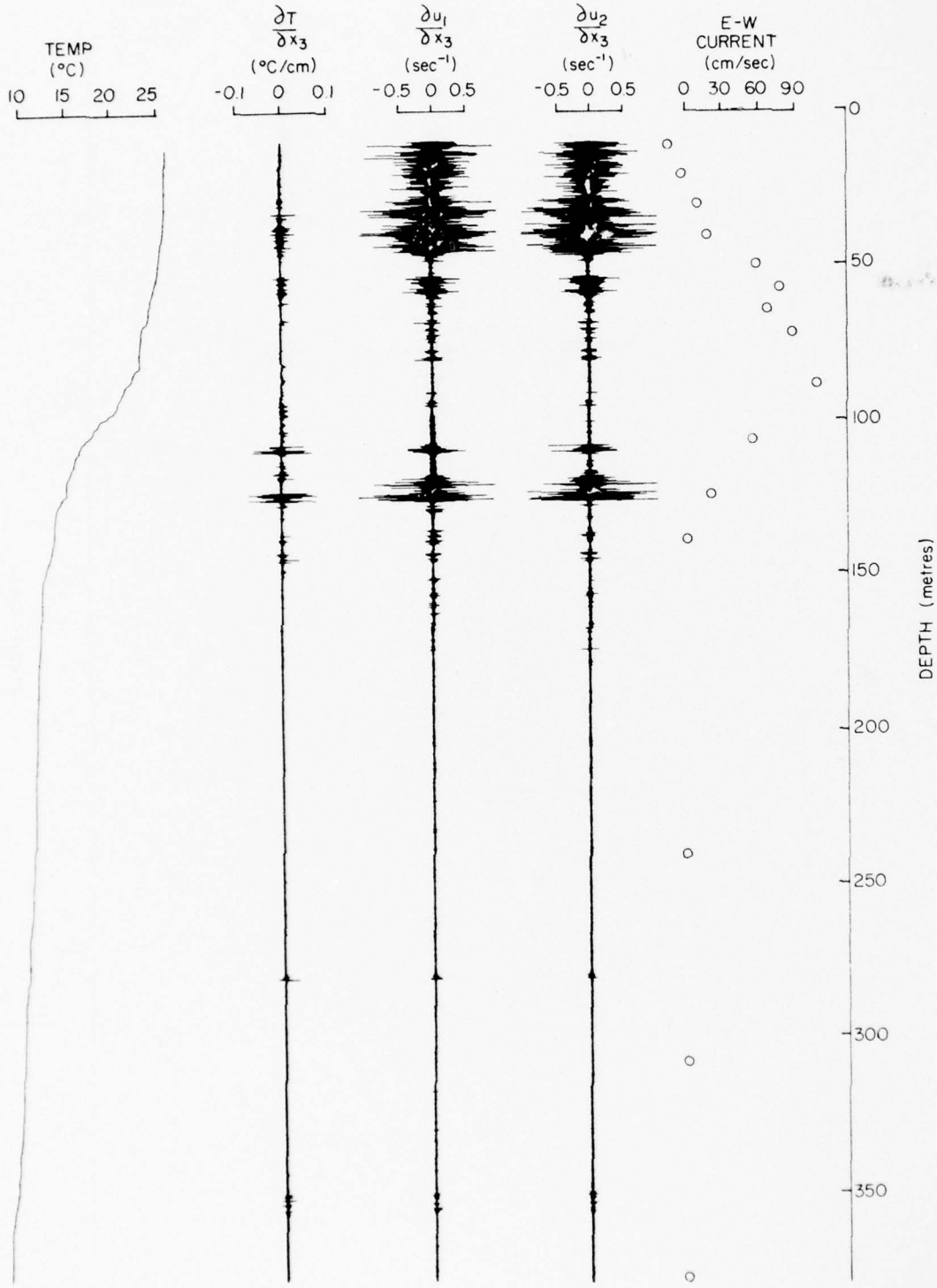

Figure 14 Profile 28 of microstructure measurements and temperature near 32°59'W, 0°2'N and the large scale current profile measured by J. Bruce.

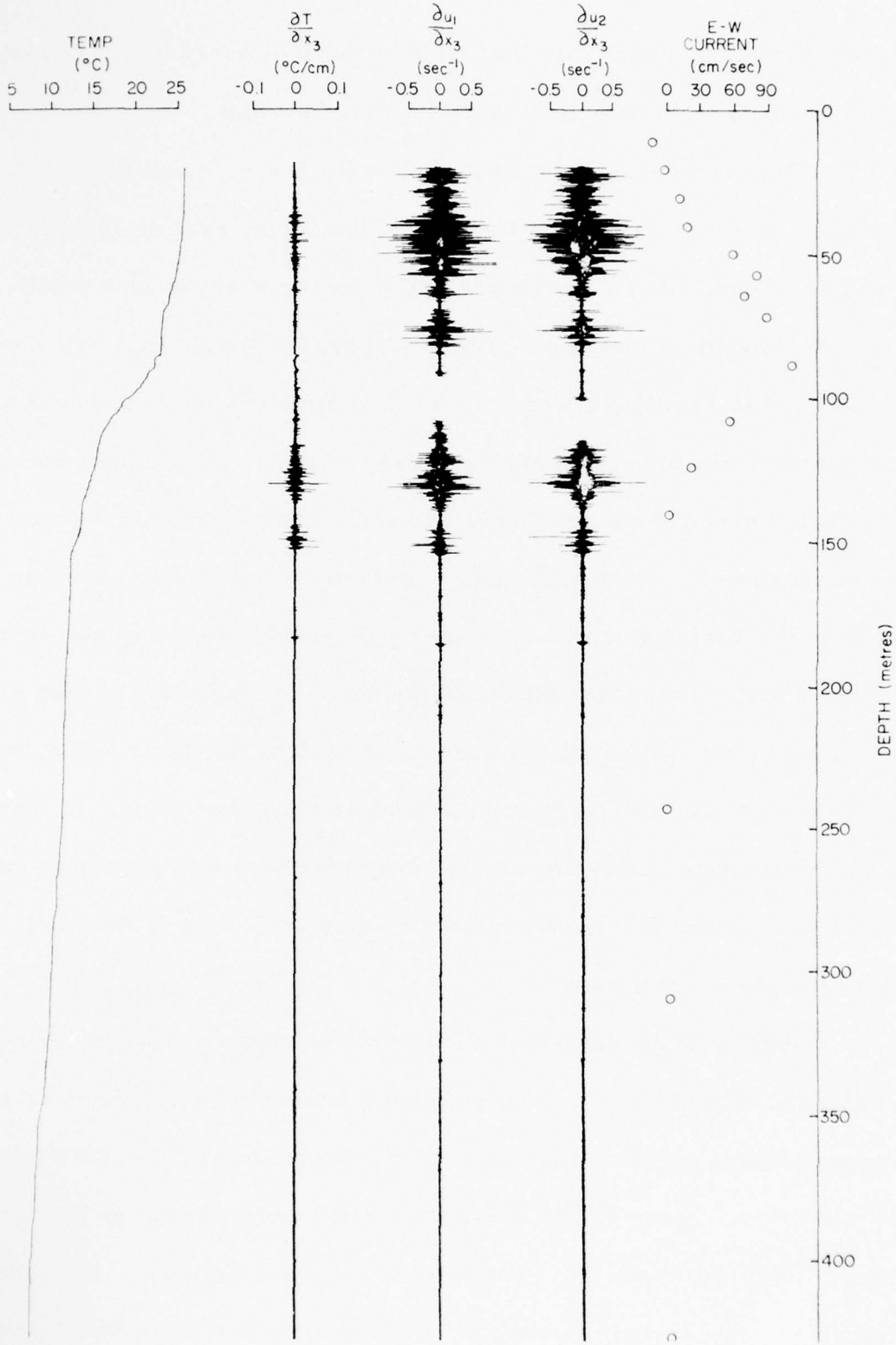

Figure 15 Profile 29 of microstructure measurements and temperature near 32°59'W, 0°2'N and the large scale current profile measured by J. Bruce.

signals include most but not all of their respective microstructure ranges, with the small scale limitation being the more serious.

All the profiles except number 20 were taken through the undercurrent. The positions of the Camel profiles are marked on figures 2 to 4 to give an indication of the nature of the undercurrent at each profile. Also, the velocities measured by Mr. J. Bruce of Woods Hole are shown in figures 9 to 15. These were recorded within a few hours and several kilometres of the microstructure profiles, with the largest difference for profile 22 where the currents were measured about 5 hours before and 5 kilometres away. To measure these currents, a 6-10 minute average reading of a Braincon model 252 meter was taken, and magnitudes indicated are relative to the current at 300 metres. The large scale velocities measured by the current meter were not sensed by the shear probe, which can only measure velocity gradients at microstructure scales. Gradients at microstructure scales are usually associated with turbulence, as noted in section 2. Conversely, the microstructure scale shears were not sensed by the current meter.

In Table II the difference Richardson numbers (calculated using equation 2.34) are listed. They have been determined from the current meter readings and from the values of σ_T determined by Dr. Katz from the CTD data. These values should be treated with caution, as the current meter, CTD and Camel were not lowered together, but were each separated in time and space from the other by several hours and kilometres. Any shift in depth of the undercurrent between readings of current and density

Profile 20		Profile 22		Profiles 23,24		Profile 25		Profiles 28,29	
depth (m)	Ri_Δ	depth (m)	Ri_Δ	depth (m)	Ri_Δ	depth (m)	Ri_Δ	depth (m)	Ri_Δ
10		10		10		10		10	
	0.2		0.3		0.1		0.6		0.0
20		20		20		20		20	
	0.4		0.2		0.1		0.0		0.1
30		30		30		30		30	
	0.6		0.3		7.		0.0		0.8
40		40		40		40		40	
	10.		0.6		2.		3.		0.1
50		50		50		50		50	
	5.		0.2		0.2		5.		0.2
60		57.5		60		60		57.5	
	8.		0.2		0.8		300.		0.7
70		65		70		70		65	
	0.5		0.3		0.6		4.		0.3
80		72.5		77.5		80		72.5	
	4.		0.4		10.		2.		2.
100		85		98		100		90	
	0.8		0.4		1.		1.		0.5
137		112.5		148		145		107.5	
	2.		0.3		2.		70.		0.4
160		140		190		190		125	
	4.		1.		0.3		100.		0.4
222		185		225		275		140	
	8.		0.1						1.
260		225						170	
	4.		1.						1.
290		265						242.5	

Table II Difference Richardson numbers corresponding to microstructure profiles

could cause errors in the values of Ri_{Δ} .

The profiles through the undercurrent all show similar features. The most intense turbulence, as indicated by the mean square microstructure velocity gradients, is usually at the base of the upper mixed layer, near the top of the thermocline. In all cases, the velocity core of the undercurrent is much less turbulent. This core corresponds roughly to the region where the large scale temperature gradient is highest. Below the velocity core of the undercurrent, the turbulence is more intense than at the core, but less intense than the turbulence above the core. Below this third region, the profiles are marked by intermittent turbulence separated by quieter regions.

Profile 20 is outside the undercurrent, and profile 25 must be at the extreme southern edge, as the peak eastward velocity is 5 cm/sec. Profile 25 shows intense turbulence at the top and bottom of a very sharp thermocline. Profile 20 has its most intense turbulence in the thermocline.

All profiles through the undercurrent show the most active turbulence at the top of the thermocline; but the nature of the turbulence near the ocean surface varies from the very low levels found in profiles 23 and 24 above 30 metres to the quite high levels found in profiles 28 and 29.

Other evidence showing the most active turbulence to be in the upper thermocline is available. For example, an examination of the temperature microstructure profiles obtained during the ATLANTIS II cruise by Mr. L. Bilodeau using small free-falling instruments, shows that all eight profiles through the undercurrent were similar to those of the Camel in the upper thermocline, where they show large temperature gradients at

microstructure scales. Similar features were found in the Pacific by Gregg (1976), who measured temperature in the Pacific Equatorial Undercurrent. He concluded that turbulence was most intense above the velocity core and much weaker in the velocity core. It appears then, that the turbulence levels are generally highest in the upper thermocline.

The large scale shears have values as large as .06 sec^{-1} in this region, and rms turbulence shears are up to .3 sec^{-1} averaged over 10 m depths. The calculated values of Ri_{Δ} in the upper thermocline, shown in Table II are sometimes below 0.25. Hence the large scale shears in the upper thermocline of the undercurrent may be sufficient to maintain turbulence.

In all profiles, turbulence shears in the velocity core were low. Because the large scale density gradients are high here, and the velocity gradient must change sign, there must be a maximum in the dynamic stability. The magnitudes of the turbulence shears increase in the lower portion of the thermocline, below the velocity core. All the temperature microstructure profiles obtained by L. Bilodeau show small microstructure temperature gradients in the middle of the thermocline, and larger values in the lower thermocline. The values of Ri_{Δ} are a maximum in the velocity core, and smaller below the velocity core.

Below both the Pacific and Atlantic Equatorial Undercurrents a region of nearly uniform temperatures has been observed, with tempera-

tures near 13°C. This feature, referred to as the thermostad, is most evident for profiles 23 and 24 at 170 to 270 and 170 to 245 metres, respectively. The value of Ri_{Δ} between 190 and 225 metres is 0.3. The accuracy of any one of these values of Ri_{Δ} is not sufficient to allow one to predict whether turbulence may be present. If this value for the Richardson number were to be present throughout the region, then shear instabilities would not generate turbulence. However, it is possible that shears are concentrated on several surfaces within the thermostad, and patches of turbulence may develop from shear instabilities as noted in section 2.6. Below the thermostad of profiles 23 and 24, intense turbulence is found, with turbulence shears almost as large as those in the upper thermocline. Other profiles do not show thermostads as extensive as observed in profiles 23 and 24, nor do any have such intense turbulence below 200 metres.

Two pairs of profiles, 23, 24 and 28, 29 were taken consecutively. Profile 23 was at 28°01'W, 0°18'S at 1322 GMT on July 16; profile 24 was at 28°03'W, 0°17'S at 1435 GMT as determined from the closest satellite fixes. The turbulent patch size and intensity of the two profiles are similar. However, the depths of the features of profile 24 are 10 to 30 metres shallower than those of profile 23. The depths of features of profile 23 agree to within a few metres with those recorded by the CTD meter at 28°01'W, 0°18'S at 1219 GMT to 1305 GMT. There may be some disturbance or wave compressing or raising the features of the water column sampled by these profiles. If it is large scale and long period, it might

produce quasi-steady shears which could maintain a uniform level of turbulence over the time and space intervals observed. The high levels of turbulence observed in the thermostad for these profiles may have been enhanced by this disturbance, and may not be due only to the long term average current.

The pair of profiles 28 and 29 were taken near 32°59'W, 0°2'N at 0917 GMT and 1029 GMT respectively on July 23. Only one satellite fix was available for this pair, but I believe that actual positions of the profiles could differ by several kilometres. For these profiles, the depths of features as indicated by the temperature signals are similar. Above the core, the turbulence level is similar for these profiles. In the lower thermocline, the region of turbulence is thicker for profile 29. Below the thermocline, the two thin patches of turbulence at 280 metres and 360 metres observed for profile 28 have decreased in intensity for profile 29. The noise levels of the gradient outputs near 18 Hz for these profiles are higher than found on other profiles, and may have masked some weak turbulence.

An expanded chart record of profile 23 is shown in figures 16a and 16b. These expanded gradient profiles show the relationship between the velocity and temperature microstructure. It can be seen that where temperature microstructure is present, and both positive and negative microscale temperature gradients are observed, there is always velocity microstructure (and hence turbulence). Turbulence requires fluctuations of all three components of velocity and mixes a fluid. Hence a large

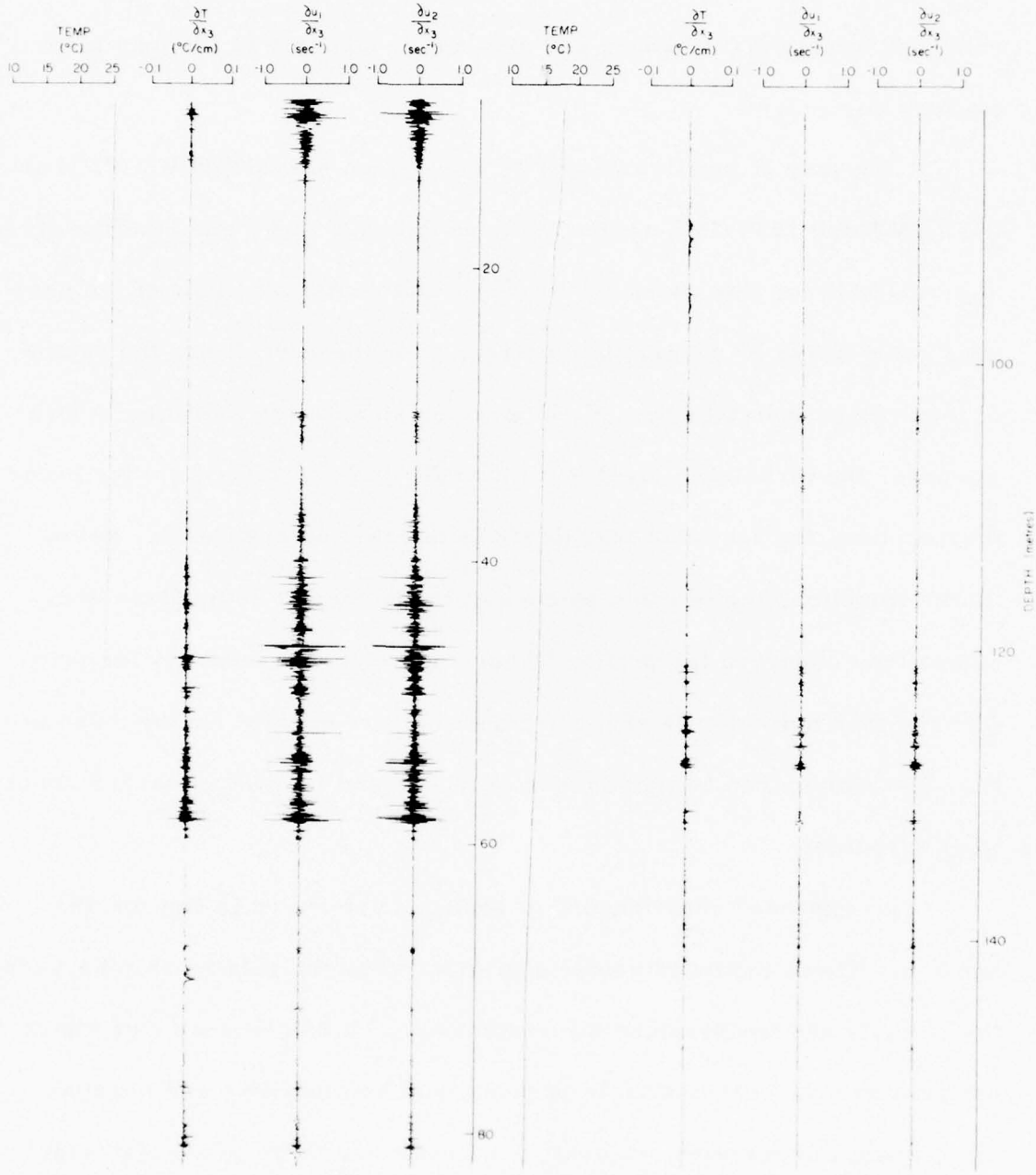

Figure 16a Profile 23 of microstructure measurements from 10 metres to 160 metres.

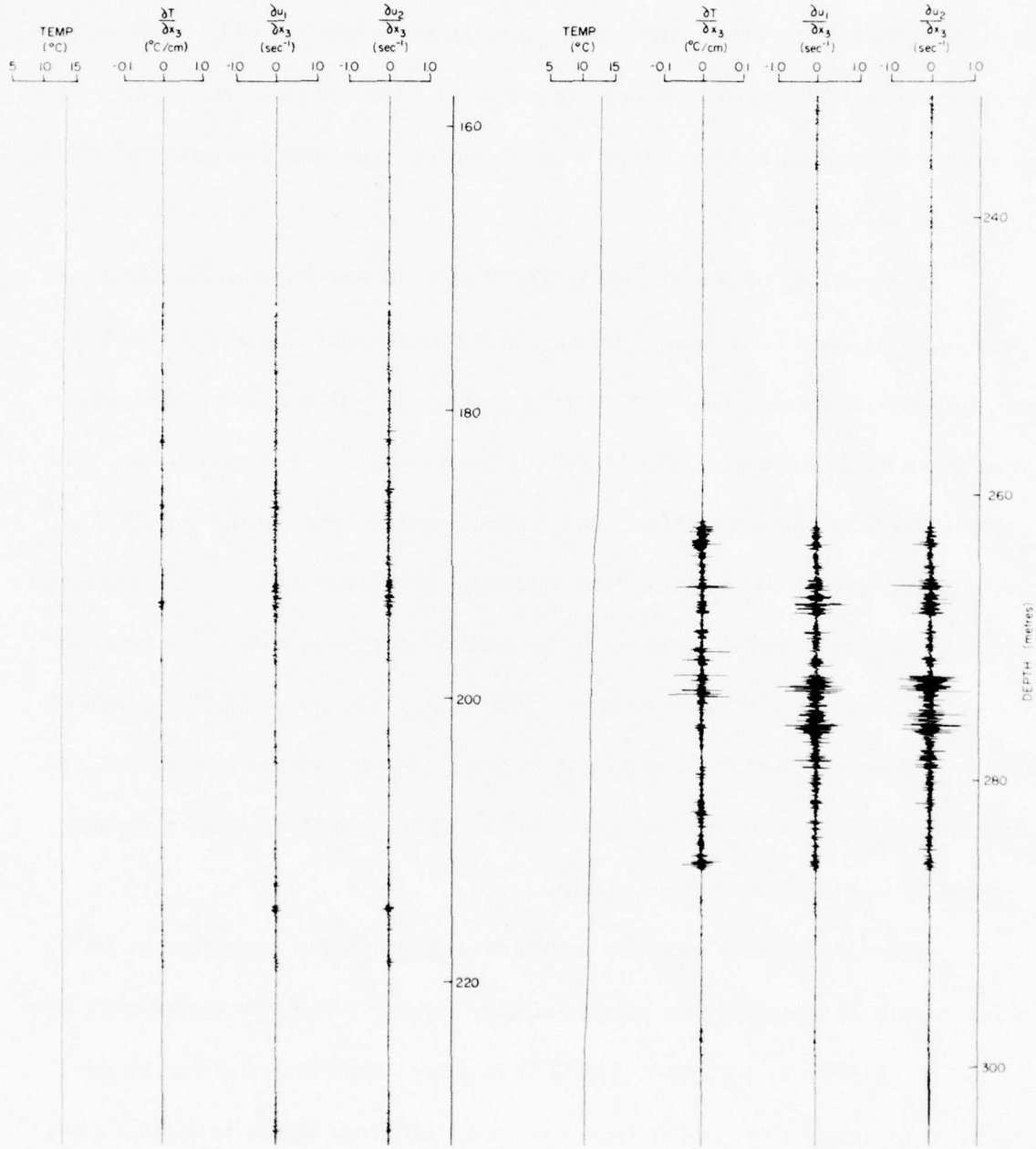

Figure 16b Profile 23 of microstructure measurements from 160 metres to 305 metres.

scale temperature gradient will be broken up into many smaller gradients, and the vertical turbulent velocities will transport colder fluid up, warmer fluid down and cause the positive and negative temperature gradients observed. Where temperature microstructure is present, but only positive temperature gradients are observed, there is no velocity microstructure observed. Examples of this latter type of microstructure are found at 69-70, 91 and 96 metres.

The portion of the record near 69 metres has been expanded even further in figure 17. Here, a large scale temperature gradient has two maxima which extend over 1.5 metres. Many small positive gradients, separated by about 4 cm, are found within this large scale gradient. The velocity microstructure here is below the noise level. In the patch of microstructure at 65 metres, both negative gradients and some turbulence are found. This region from 65 to 80 metres corresponds to the core of the undercurrent, where one expects dynamic stability to be the greatest. The interface at 69 metres also marks the salt core of the undercurrent. Below this point, salinity decreases with depth, and the double diffusion regime of salt fingering is possible.

The small scale positive temperature gradients observed at 69 metres may be the remains of a mixing event for which the turbulence has decayed. Linden and Turner (1975) have shown that internal waves can carry away from a turbulent region a small fraction of the turbulent energy if there is a stably stratified region above or below. The turbulence above the core may generate such waves which propagate down through the core and generate instabilities in the core, or sharpen already

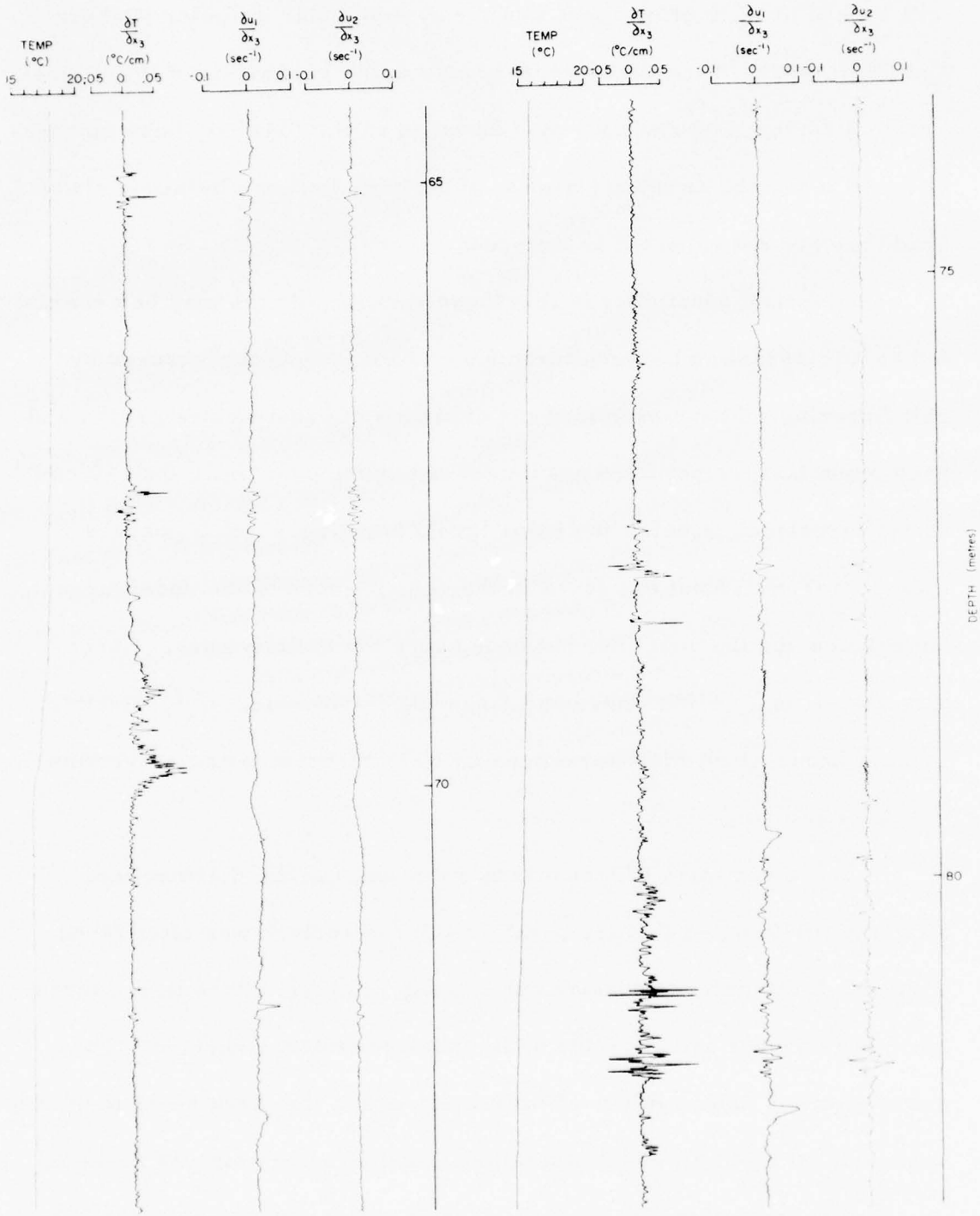

Figure 17 Profile 23 of microstructure measurements from 64 metres to 83 metres. Low frequency noise has not been removed, and is especially noticeable at 70 metres. The 18 Hz low pass filter partially smoothed noise spikes at 72, 75.5, 79 and 82 metres.

existing temperature gradients. An infinitely sharp temperature gradient will spread to 5 cm after about an hour by molecular diffusion (Osborn and Cox, 1972). This length corresponds to the separation of these small gradient spikes, and one hour may be taken as the "age" of these spikes, although it may be an over-estimate of the time because infinitely sharp gradients are not expected in the ocean.

A second possibility is that these small gradients may be generated by an interaction between turbulence and the convection caused by salt fingering. I have examined the expanded microstructure graphs and have found that temperature gradients, extending over more than 50 cm, where turbulence is below the noise level, have these small positive spikes on them. Most are found in the velocity core of the undercurrent, some below the thermocline, but none above the salinity core. Hence they are all in a region where salt fingering is possible. Unfortunately, little is known about the interactions between turbulence and convection set up by salt fingering.

In his summary of measurements in the Pacific thermocline, Nasmyth (1970) noted that temperature microstructure was often found without velocity microstructure but velocity microstructure (i.e., turbulence) was always accompanied by temperature microstructure. The Camel profiles show regions of turbulence where the large scale temperature gradient is small and temperature microstructure signals lie below the noise level (0.002 C°/cm) of the circuit. The upper mixed layer of profile 25 above 45 metres shows this behaviour, as does a portion of profile 23 at 240 m, in the thermostad. In almost all other regions of

active turbulence, temperature microstructure is also found.

Because turbulence was always observed in the thermocline, above and below the velocity core, it may be that the seasonal scale velocity gradient is sufficiently large to maintain turbulence in this region. Even in the velocity core, the "age" of the temperature gradients is less than an hour, and there appears to be some process present to stir these waters — either shear instabilities or double diffusion or some combination of these two.

4.2 Spectra of Turbulence

Spectra of turbulence were computed to estimate dissipation, evaluate the degree of isotropy and provide a useful check on sensor response. If turbulence is locally isotropic at wavenumbers corresponding to the dissipation range, then equation 2.22 can be used to calculate viscous dissipation from a few measurements. If turbulence was locally isotropic over a range of wavenumbers, then the resolution of the sensor could be determined from a comparison of the known spectral shape with the measured. For the measurements of turbulence using the Camel, neither the resolution of the probe, not the degree of isotropy are well known. However, by comparing spectra from various depths, the resolution can be determined to an acceptable degree of accuracy.

There are several profiles of microstructure from the ATLANTIS II cruise which show regions in which one might expect sufficiently locally isotropic turbulence to lead one to expect a universal spectrum over

measurable wavenumbers. These regions are the upper mixed layers of profiles 25, 28 and 29. Here the stratification is low and the mean shear is high. Difference Richardson numbers approach zero for several 10 metre thick layers in these profiles. Of the two scale lengths noted in section 2.5 for the high wavelength limit of local isotropy, that of Ozmidov is most readily calculated. This length scale is

$$l_b = \bar{\epsilon}^{1/2} N^{-3/2} \qquad 2.32a$$

For the upper layers, this scale is longer than 50 cm for profile 25, 20 cm for profile 28 and 15 cm for profile 29. The stratification in the upper layer of profile 25 is so small that measureable temperature and conductivity gradients at microstructure scales have disappeared within the upper 50 metres, although velocity gradients are present at all scales.

The power spectra of velocity components for these regions are shown in figures 18 and 19. The method of calculation is outlined in Appendix B. The spectra are from three sections extending through about 16 metres, and one through about 8 metres, representing 8192 and 4096 data points respectively, and are band averaged as explained in Appendix B. They have been fitted to the universal $F_2(k/k_s)$ curve of figure 5 according to the method described by Stewart and Grant (1962) which is also outlined in Appendix B. This method of curve fitting yields an estimate of the value of the viscous dissipation $\bar{\epsilon}$, averaged over the depth corresponding to the spectrum, and this value of $\bar{\epsilon}$ is denoted as $\bar{\epsilon}_U$ to indicate how it is derived.

Figure 18 shows the fit of the spectra (normalized using

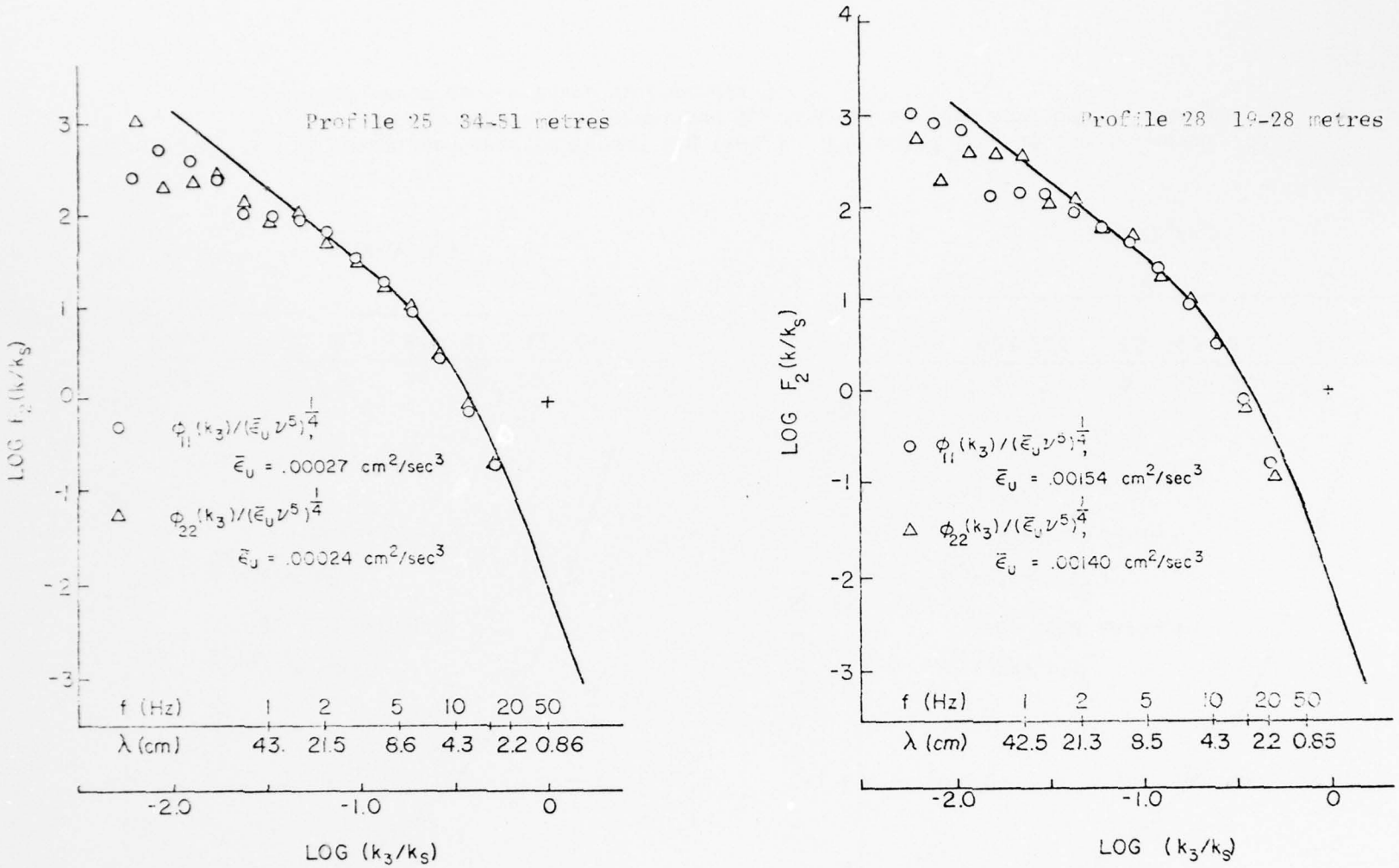

Figure 18 Log of normalized spectra versus log (k/k_s). The solid line is the universal log F_2 spectrum and the log of the normalized φ_{11} and φ_{22} spectra have been fitted to the universal curve as described in Appendix B.

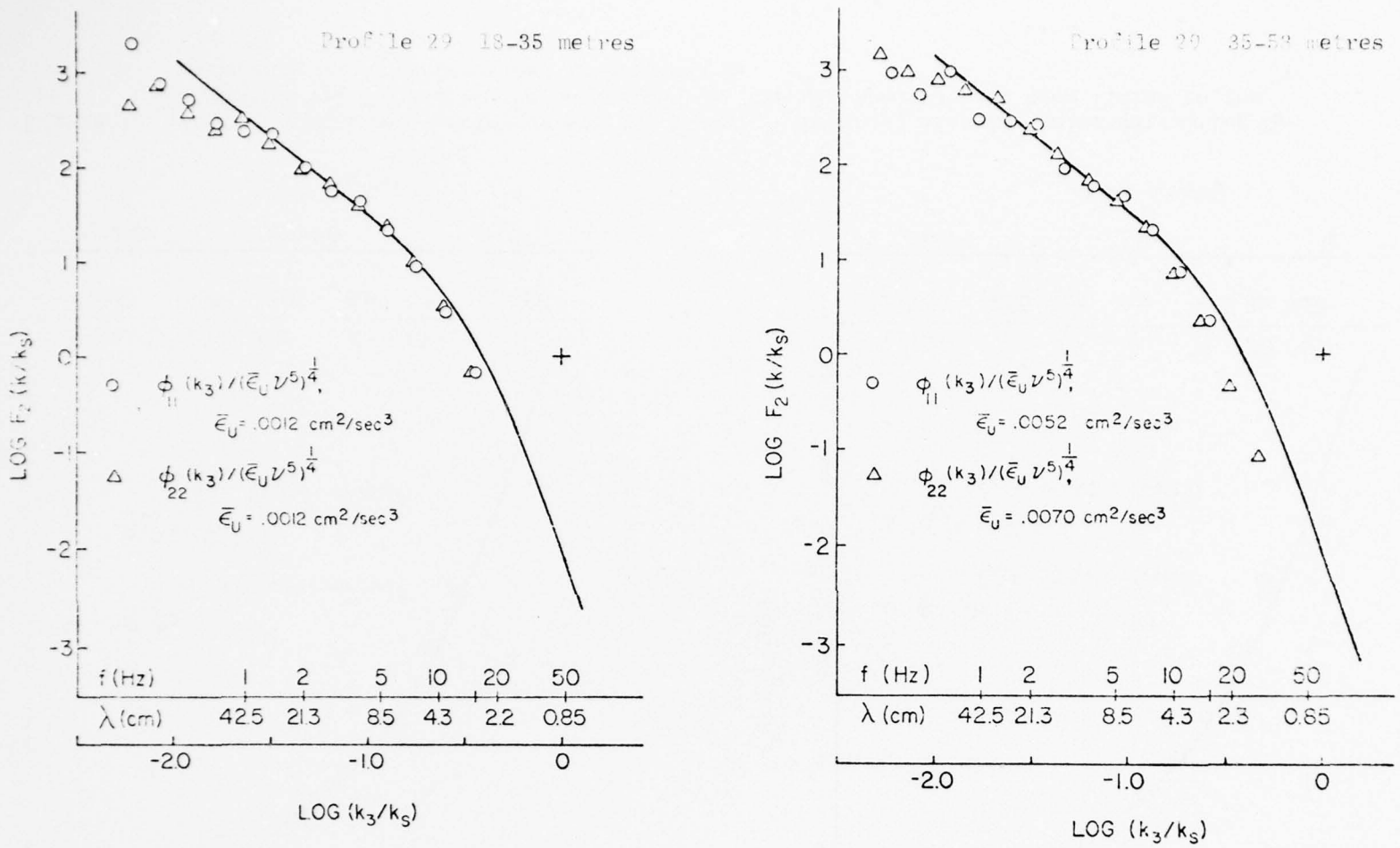

Figure 19 Log of normalized spectra versus log (k/k_s). The solid line is the universal log F_2 spectrum and the log of the normalized φ_{11} and φ_{22} spectra have been fitted to the universal curve as described in Appendix B.

$\bar{\epsilon}_u$) of profile 25 to the universal curve. There is reasonable agreement from log $(k_3/k_s) = 1.3$ to -0.5, which encompasses the centre of the dissipation spectrum $G_2(k/k_s)$. At lower wavenumbers the spectral coefficients fall below the F_2 curve, due to a high pass filter in the shear circuit which attenuates the signal at frequencies less than the half power point near 1 Hz. At values of log $(\frac{k_3}{k_s}) > -0.5$ the spectral coefficients fall below the universal curve. Beyond the last point shown, noise dominates the spectra. (The noise spectrum will be shown in figure 24.) The output covers a small range of wavenumbers. A broader range of wavenumbers would be desired for comparison with the universal curves.

Figures 18 and 19 also show power spectra of profiles 28 and 29 where more active turbulence was encountered. Here deviation of observed data from the universal curve begins at values of log $\frac{k_3}{k_s}$ greater than -0.7, just beyond the peak of the dissipation spectrum $G_2(k/k_s)$ which is near log $\frac{k_3}{k_s} = -0.8$.

In the power spectra of figures 18 and 19 the deviation of the measured values of the spectral coefficients from the universal curve is about -1 db (-20%) at 11 Hz (~4 cm), and -3 db (-50%) at 15 Hz (~3 cm). Because this behavior of the power spectra coefficients is nearly uniform over a wide range of values of $\bar{\epsilon}$, I believe that spatial averaging of the probe may be the cause. The criterion of Siddon (1969) is that the shear probe can resolve to wavelengths as small as four times the length scale of the probe, which is taken to be the diameter. The power spectra of figures 18 and 19 are about 1 db below the universal curve at wavelengths of eight times the probe diameter. The shear probes used in this study

were proportionately longer than those of Siddon, and it may be that these probes are sensitive to cross-stream flows in the region of the probe back from the tip, for which case the diameter is no longer the appropriate length scale.

Several other possibilities have been examined to explain the differences between the observed and universal spectra. The universal curve of Nasmyth was chosen for computation of $F_2(\overset{k}{\overline{k}}_s)$ because of the low scatter in his spectral coefficients over almost three decades of wavenumbers, the extremely large Reynolds number of the turbulence in the tidal channel where the measurements were taken, and the close agreement of his $F(\overset{k}{\overline{k}}_s)$ curve with those obtained by others. Over the range of non-dimensional wavenumbers used for comparison in figures 18 to 21, the differences in shape among the Nasmyth curve of $F(\overset{k}{\overline{k}}_s)$, an earlier curve by Grant et al.(1962), and later results by Boston (1970) are insignificant. Boston found that his data which had the greatest signal to noise ratio agreed best with Nasmyth's results.

Universal curves might depend upon the degree of intermittence of the turbulence; a dependence most noticeable as a change in curvature of the "knee" of the spectra (Pond, 1965 and Nasmyth, 1970 both discuss this). I have tested my spectra with a rough test used by Nasmyth (1970) on his data and found no appreciable difference in degree of intermittence between the two sets of data. If indeed the intermittency of the turbulence has reduced the curvature of the "knee" of the curve, it may affect Nasmyth's and my data in a similar way.

The transfer functions of all the filters and amplifiers have been checked (see Appendix C) and their high frequency roll-off cannot be the cause of the high frequency roll-off of my spectra. However, a better agreement can be found for these spectra if the actual sensitivity of the shear probes is greater than the calibration value. A higher sensitivity would give closer agreement between the $F_2(\overset{k}{\overline{k}}_s)$ curve and calculated spectra at high wavenumbers. For example, the separation between the calculated spectra and the $F_2(\overset{k}{\overline{k}}_s)$ curve decreases to about 1 db at 15 Hz for profile 29 if the sensitivity is increased by 40%. Such an increase is greater than the expected error in the calibration; it is unlikely that this effect can explain all the sudden roll-off of the spectra, but it may contribute some apparent roll-off.

There is the possibility that the turbulence does not follow a universal curve at the wavelengths sensed. The length ℓ_b noted at the beginning of this section is only a guideline, as no rigorous tests of local isotropy at wavelength ℓ_b have been made. There are several tests for local isotropy which can be applied (equations 2.18 and 2.19), which test for the conditions upon which the Kolmogoroff hypotheses are based. Of these, I can test only the relation

$$\varphi_{11}(k_3) = \varphi_{22}(k_3) \qquad 2.18$$

For the spectra shown in figures 18 and 19 the spectral values of $\varphi_{11}(k_3)$ and $\varphi_{22}(k_3)$ appear to be nearly equal. The ratio

$$\frac{\bar{\epsilon}_{11}}{\bar{\epsilon}_{22}} = \frac{\frac{15}{2}\nu\int_0^\infty k_3^2\,\varphi_{11}(k_3)\,dk_3}{\frac{15}{2}\nu\int_0^\infty k_3^2\,\varphi_{22}(k_3)\,dk_3} \qquad 4.1$$

determined from fitting each universal curve takes values of 1.1, 1.1, 1.0, 0.7 for figures 18 and 19. These values are as close to 1.0 as the errors in curve fitting will allow. This test gives support for the presence of local isotropy, but does not prove that it is present. The spectra do follow a universal curve at wavelengths greater than 4 cm, and fall below the universal curve at shorter wavelengths. I cannot prove that the calculated spectra are of locally isotropic turbulence or that they should follow a universal spectrum.

Such spatial averaging of the probe would attenuate fluctuations at high wavenumbers. This is not a problem for the turbulence found in the upper layer of profile 25 (figure 18) where the average value of $\bar{\epsilon}_u$ for the $\varphi_{11}(k_3)$ spectra is 2.7×10^{-4} $cm^2 sec^{-3}$. The peak of the dissipation spectrum is at $k = .16k_s = .16(\bar{\epsilon}\,\nu^{-3})^{\frac{1}{4}}$, which has a wavelength of 10 cm. However, the larger value of $\bar{\epsilon}_u$ determined from the spectrum of profile 29 from 35 to 51 m in figure 19 is $7.0\times10^{-3} cm^2 sec^{-3}$, and the peak of the corresponding dissipation spectrum is at 4 cm. This peak lies close to the wavelengths at which spatial averaging occurs, and velocity fluctuations at small wavelengths (high wavenumbers) will be missed.

In figure 20, a graph of $G_2(k/k_s)$ vs. k/k_s is shown for the three regions represented in figures 18 and 19 which have a large range in $\bar{\epsilon}_u$. Equation 2.26 is used to derive $G_2(\frac{k}{\bar{k}_s})$ from the measured spectra of

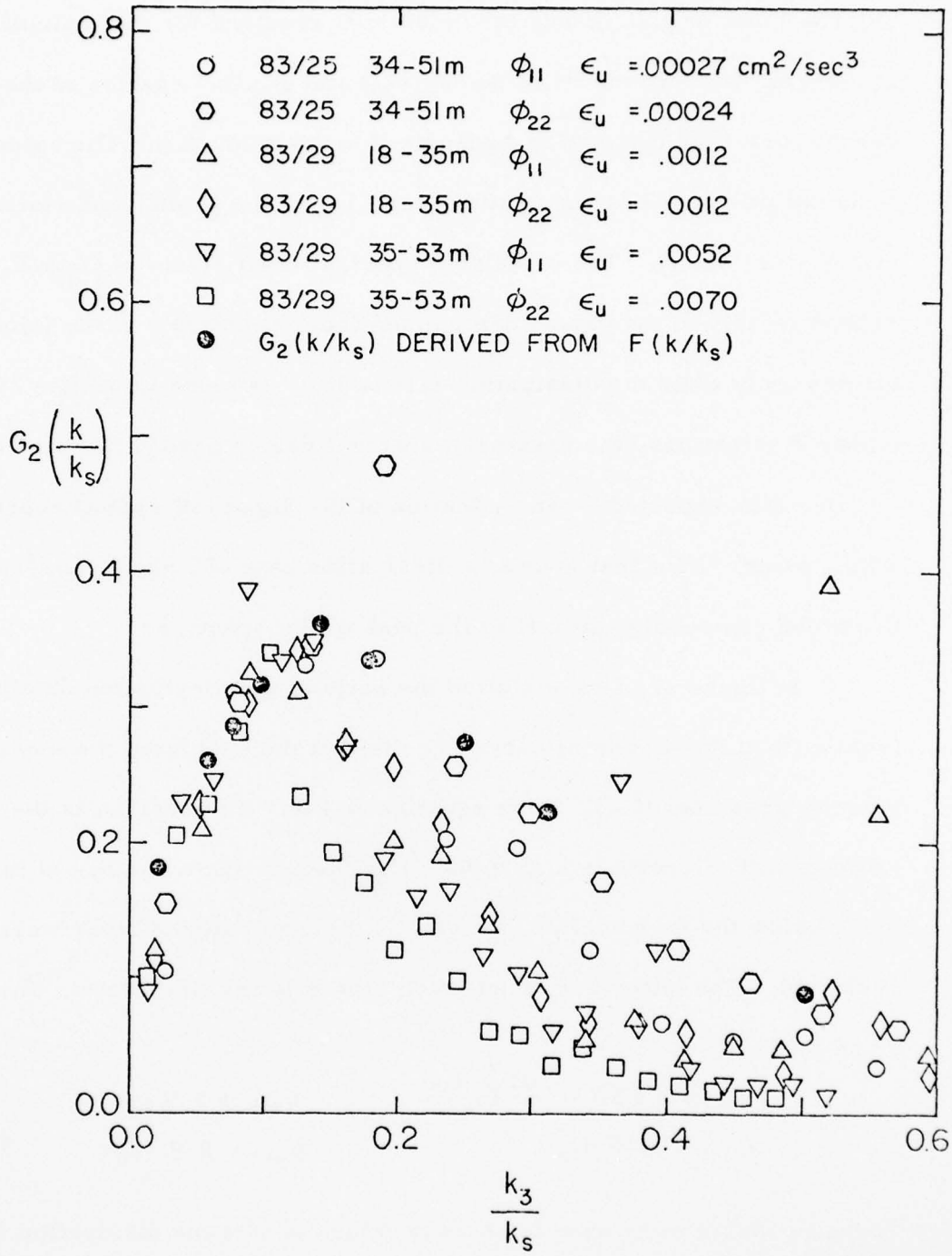

Figure 20 Normalized dissipation spectra $G_2(k/k_s)$ vs. k/k_s for three of the four regions of figures 18 and 19.

$\varphi_{11}(k_3)$ and $\varphi_{22}(k_3)$, and the value of $\bar{\epsilon}_U$ required for this calculation is determined from the fit of the $\varphi_{11}(k_3)$ and $\varphi_{22}(k_3)$ spectra to the universal curve, as outlined in Appendix B and section 2.4. The value of $\bar{\epsilon}_U$ is not influenced by the spatial averaging of the probe, and viscosity changes are small. The calculated spectral coefficients of $G_2(k/k_s)$ correspond closely to the values determined from Nasmyth's curve (closed circles) only when the dissipation rate is low, as found in profile 25. At higher dissipations, the measured spectral values beyond the peak are smaller than expected -- an indication of the degree of spatial averaging taking place. Note that even at a dissipation rate of $7.0 \times 10^{-3}\ cm^2 sec^{-3}$, the probe can resolve almost to the peak of the spectrum.

In figure 21, I have plotted the ratio of the dissipation obtained from a fit to the universal curve ($\bar{\epsilon}_U$) to that derived from the measured velocity gradients ($\bar{\epsilon}_M$), using equation B-14b. The absissa is the Kolmogoroff microscale $k_{sM} = (\epsilon_M \nu^{-3})^{\frac{1}{4}}$. Spectra from patches of turbulence below the thermocline, as well as the upper mixed layer were evaluated. The latter are found much closer to the line drawn, which is given by

$$\bar{\epsilon}_U = .638\, \nu^{-.432}\, \bar{\epsilon}_M^{\,1.14} \qquad k_{sM} > 2.8\ cm^{-1}$$

$$\bar{\epsilon}_U = 1.15\, \bar{\epsilon}_M \qquad k_{sM} < 2.8\ cm^{-1} \qquad 4.2$$

These formulae were used to correct values of viscous dissipation $\bar{\epsilon}_M$. The method of calculating $\bar{\epsilon}_M$ is discussed in section 4.3. The lower limit of $\frac{\epsilon_U}{\epsilon_M} = 1.15$, and some of the departure of data points from the fit are likely due to the method of calculating $\bar{\epsilon}_M$. The largest departures of data

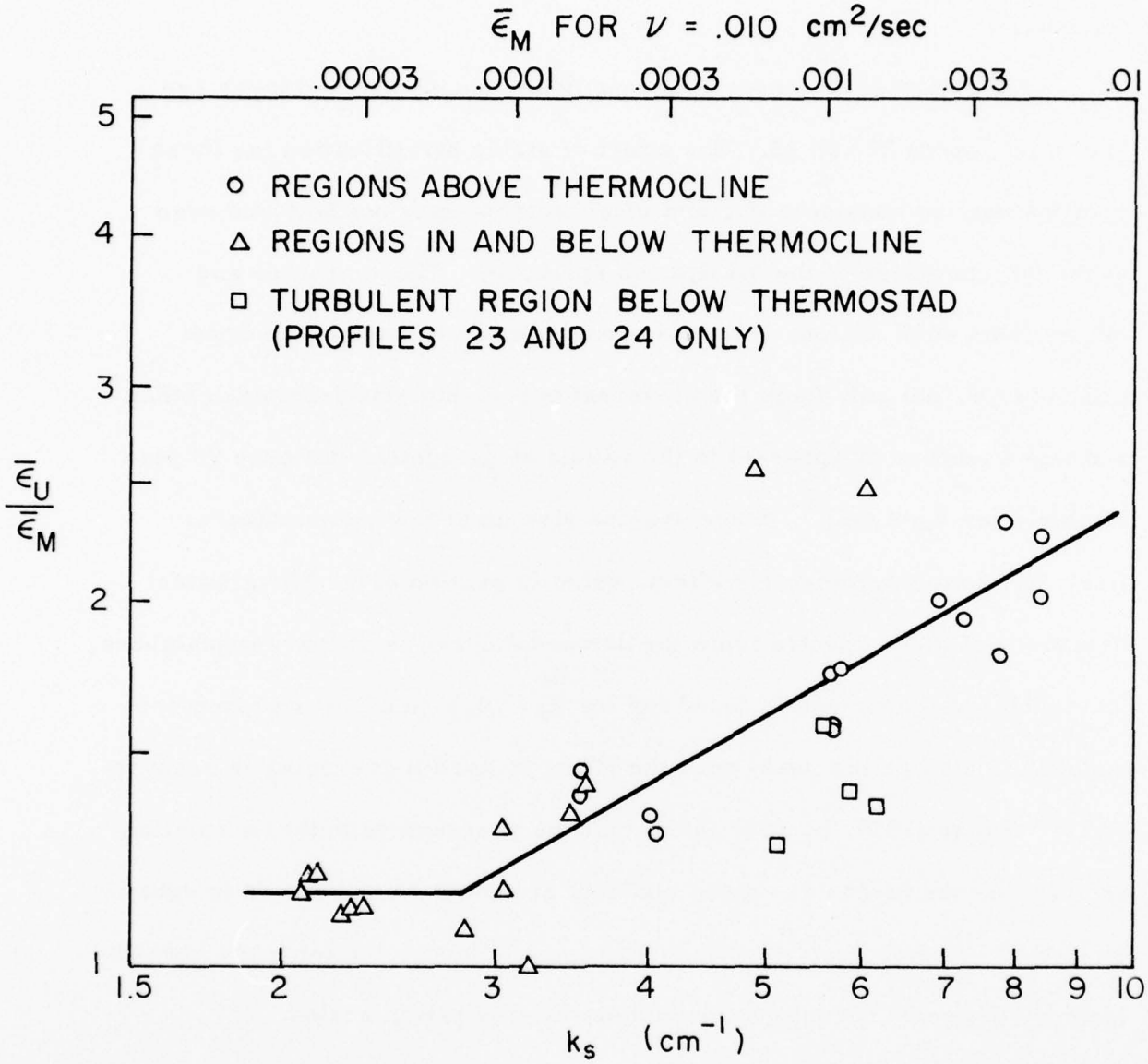

Figure 21 Ratio of dissipation ($\bar{\epsilon}_u$) determined from fit of measured spectra to the universal curve divided by dissipation ($\bar{\epsilon}_M$) determined from variance of microscale velocity gradients.

points from the line representing the correction formula are 50% or more, but almost all values of $\frac{\bar{\epsilon}_U}{\bar{\epsilon}_M}$ fall within $\pm 30\%$ of the value predicted by the formula.

Spectra of turbulence in regions below the well mixed layer are shown in figures 22 and 23. The effect of stable stratification for these profiles may be considerable, and local isotropy may not be found even at the wavenumbers of the dissipation spectrum. These spectra and others from such regions show more variation than those of the upper mixed layer, not only from the universal curve, but also from each other and this variation is apparent in the values of $\frac{\bar{\epsilon}_U}{\bar{\epsilon}_M}$ plotted in figure 23 particularly for $k_{SM} > 4\ cm^{-1}$. Some spectra rise up at low wavenumbers, likely due to the pyroelectric effect, noted in section 3.1. The greatest departure of these spectra from the universal curve is at low wavenumbers, and much less departure is found for $\log \frac{k_3}{\bar{k}_S} > -0.8$ (i.e., at wavenumbers beyond the dissipation peak) once the effect of spatial averaging is accounted for. Hinze (1959, p. 255) shows that the pressure velocity co-relation and the viscous forces are more efficient at higher wavenumbers in equalizing the three turbulent velocity components. Hence, the tendency toward isotropy is greater at high wavenumbers at dissipation scales.

4.3 Dissipation Profiles

For the digitized data of profiles during the cruise of the ATLANTIS II a fast-Fourier transform was computed for every consecutive 1024 data points (about 2 metres depth). The input signals of $\frac{\partial u_1}{\partial t}$ and $\frac{\partial u_2}{\partial t}$, were

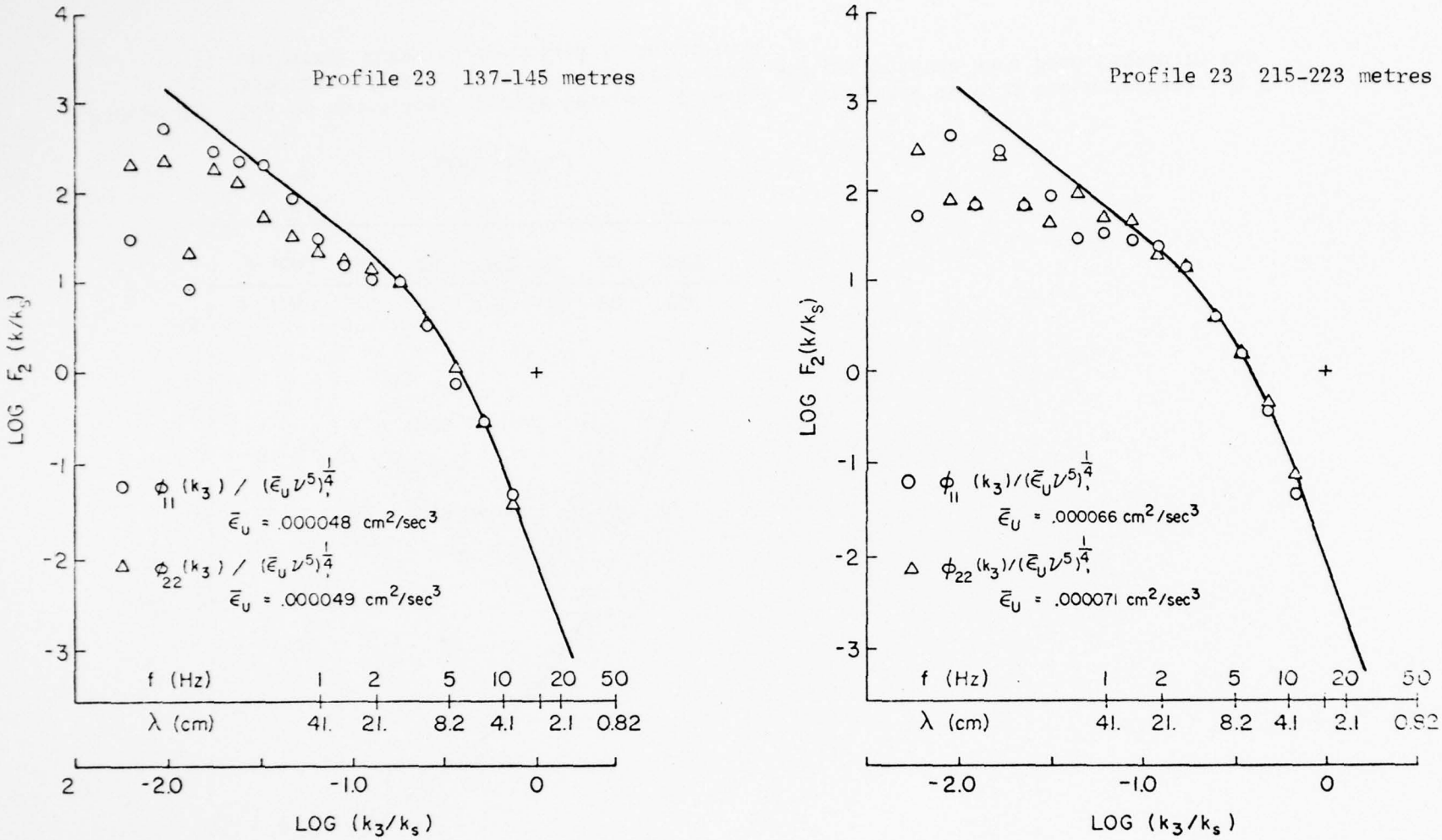

Figure 22 Log of normalized spectra versus log (k/k_s). The solid line is the universal log F_2 spectrum and the log of the normalized φ_{11} and φ_{22} spectra have been fitted to the universal curve as described in Appendix B.

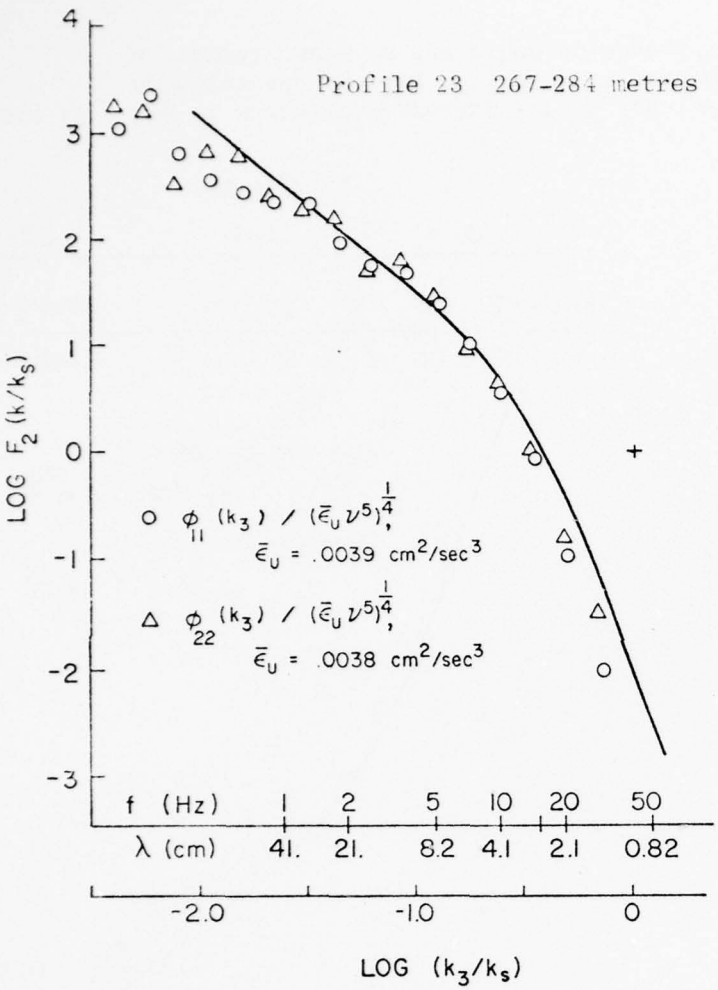

Figure 23 Log of normalized spectra versus log (k/k_s). The solid line is the universal log F_2 spectrum and the log of the normalized φ_{11} and φ_{22} spectra have been fitted to the universal curve as described in Appendix B

filtered as described in Appendix C. These filters consist of one high pass (-3db at 1 Hz) and two low pass filters (each is -3db at about 60 Hz). In addition the discriminators are -3db near 80 Hz and 60 Hz for $\partial u_1/\partial t$ and $\partial u_2/\partial t$ respectively, and roll off at 18db per octave at higher frequencies.

The measured dissipation $\bar{\epsilon}_M$ was estimated by use of the formula

$$\bar{\epsilon}_M = \frac{15}{2}\nu\overline{\left(\frac{\partial u_1}{\partial x_3}\right)^2} = \frac{15}{2}\nu\left(\frac{1.80}{250\rho S_1 V^2}\right)^2\left[\frac{2}{(1024)^2}\sum_{j=j_1}^{j=j_2} C(j)C^*(j)\right] \qquad \text{B-14b}$$

as explained in Appendix B. The values of j_1 and j_2 are the low and high limits of the transform values which are dominated by shear signals as explained below. A similar expression for $\partial u_2/\partial x_3$ is computed; each of these estimates of dissipation is corrected for spatial averaging of the probe using equation 4.2, and the average of these two corrected values is chosen as the dissipation of the two meter interval, and is referred to as $\bar{\epsilon}$. For calculating the values of $\frac{\bar{\epsilon}_U}{\bar{\epsilon}_M}$ in section 4.2, the uncorrected values of $\bar{\epsilon}_M$ are used.

The values C(j) are the transform values returned by the FFT. The advantage of calculating $\bar{\epsilon}_M$ in this way is that only transform values at frequencies where signal dominates noise are included in the summation (equation B-14-b) to estimate $\bar{\epsilon}_M$. To determine at which frequencies the signal dominates, the spectra of log $(k_3)^3 \varphi_{11}(k_3)$ and log $(k_3)^3 \varphi_{22}(k_3)$ versus log f were plotted for each FFT of 1024 data points, and some of these spectra are shown in figure 24. These spectra preserve the relative contributions to the variance of $(\partial u_1/\partial x_3)$ and $(\partial u_2/\partial x_3)$ at each frequency, and were employed only to determine these relative contributions;

hence the values of the ordinate axis are arbitrary.

The upper spectrum in figure 24 is typical of a region of very high dissipation. The shear signal dominates the noise at all frequencies up to about 30 Hz, and Fourier transform values at frequencies up to 30 Hz were summed, although values at frequencies above 20 Hz made a very small contribution to the total. The spectrum below, with $\bar{\epsilon}_M = .0021$ cm^2 sec^{-3}, has a peak at 23 Hz due to a vibration of the probe, and coefficients were summed only up to 20 Hz. The next spectrum, with $\bar{\epsilon}_M = .000025$ cm^2 sec^{-3}, shows a low peak in the shear spectrum, with the noise dominating the signal at frequencies above about 15 Hz, and coefficients at frequencies beyond 15 Hz were not included in the summation. Two spectra in the lower part of figure 24 show regions where the signal was weak at all frequencies. At some depths, where the temperature change was large and shear signals weak, a high pass digital filter was employed (-3db at about 1 Hz) to remove low frequency energy caused by the pyroelectric effect, which may have "leaked" to higher frequencies in the FFT computation and dominated shear signals. The dashed line in the spectrum at the bottom of figure 24 is from a record which has been digitally filtered. The solid line is a spectrum of the record before digital filtering. There is no peak in either spectrum between 1 and 15 Hz, and no dissipation could be estimated. It was found that for spectra where no peak appeared between frequencies of 1 and 10 Hz the estimated dissipation based upon the Fourier transform values between 1 and 10 Hz (of digitally filtered data if necessary) was less than 4×10^{-6} cm^{2}sec^{-3}. This dissipation was

AD-A045 825 BRITISH COLUMBIA UNIV VANCOUVER INST OF OCEANOGRAPHY F/G 8/3
TURBULENT ENERGY DISSIPATION IN THE ATLANTIC EQUATORIAL UNDERCU--ETC(U)
DEC 76 W R CRAWFORD N00014-76-C-0446

UNCLASSIFIED NL

2 OF 2
ADA045825

END
DATE
FILMED
11-77
DDC

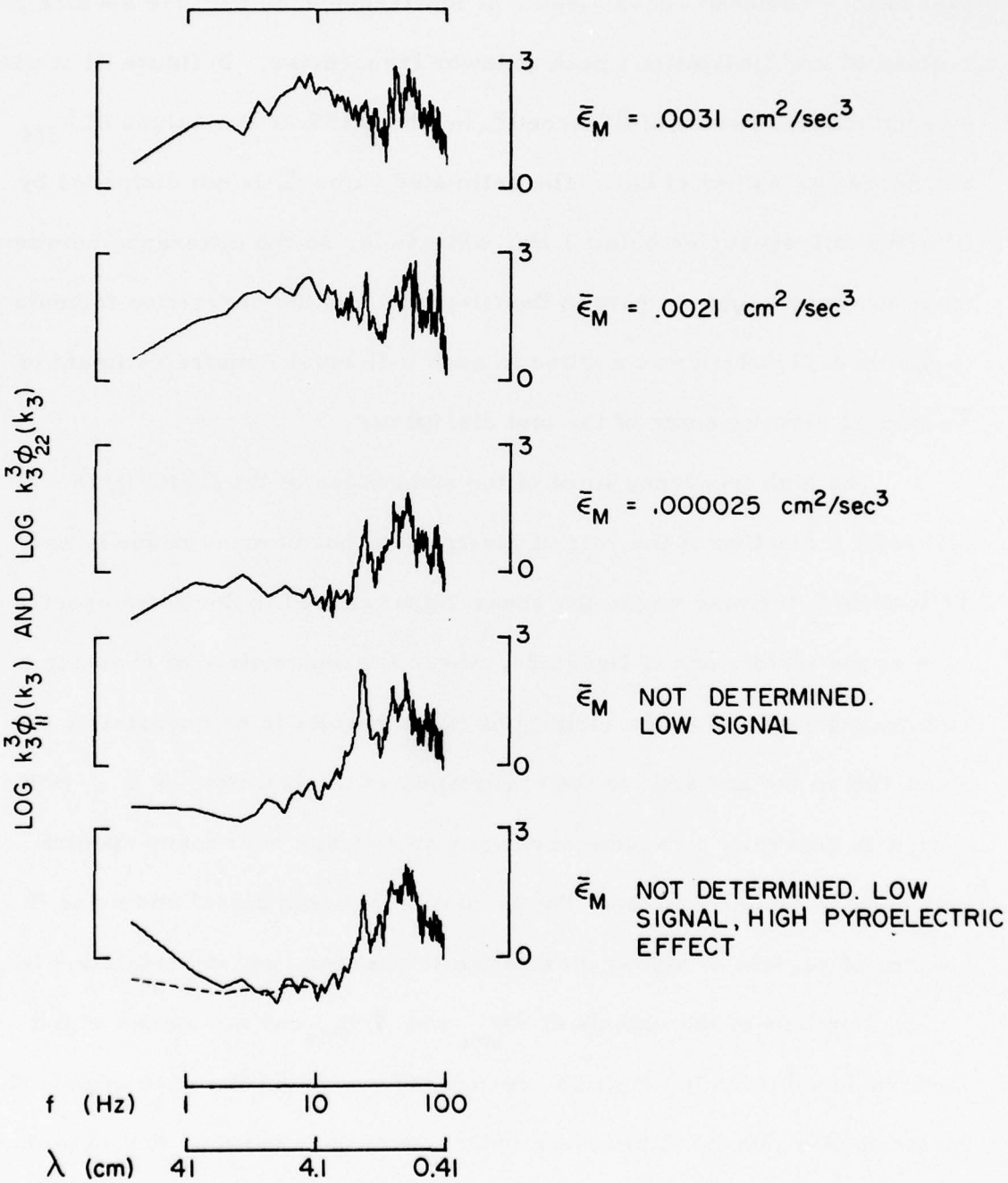

Figure 24 Dissipation spectra of various individual 2 metre sections of profile 23. A digital filter removed variance at low frequencies in the dashed line spectrum. The units on the vertical scale are arbitrary.

chosen to represent the background noise level.

It is likely, especially for regions of low dissipation, that the high pass filters removed shear signals at low frequencies because spectra in regions of low dissipations peak at lower frequencies. In figure 21 it can be seen that the values of $\bar{\epsilon}_U$ exceed $\bar{\epsilon}_M$ by about 15% at low values of k_{SM} and hence low values of $\bar{\epsilon}_M$. The estimated value $\bar{\epsilon}_U$ is not disturbed by filtering at frequencies below 1 Hz, while $\bar{\epsilon}_M$ is, so the difference between these two may be due in part to the filtering, and the correction formula (equation 4.21) which was applied to each individual 2 metre estimate of $\bar{\epsilon}_M$ should recover some of the lost dissipation.

The high frequency limit of the summation of the C(j)C*(j) is generally a function of the rate of dissipation, but in many cases it was difficult to determine where the shear signal ceased to dominate spectra such as the middle one in figure 24, where the uncertainty of choosing a high frequency limit in the vicinity of 10 Hz results in an uncertainty of about 10% in $\bar{\epsilon}_M$ and adds to the uncertainty of the estimate of $\bar{\epsilon}$. However, it is generally a random error and an average over many spectra may reduce the uncertainty. The transition between signal and noise in spectra of regions of higher dissipation is sharper, and uncertainties less.

Portions of the signals of $\partial u_1/\partial x_3$ and $\partial u_2/\partial x_3$ contain spikes which were removed from the digitized record before the FFT computation and replaced with zeros. Often these spikes were very narrow, due to a brief dropout in the signal leading into the discriminators. Because this signal was not low passed filtered, these spikes remained narrow, and disturbed

little of the surrounding digitized record. Where the spikes occupied a significant portion of the record for either of the $\partial u_1/\partial x_3$ or $\partial u_2/\partial x_3$ signals, the other was used alone to estimate $\bar{\epsilon}_M$. If both signals were fouled extensively, no dissipation was estimated.

The plots of these dissipations are shown in figures 25 to 30 together with the profiles of temperature, salinity and sigma-T provided by Dr. Katz and profiles of east-west current relative to the current at 300 metres provided by Mr. Bruce. The scale for the dissipation is logarithmic. The magnitude of the dissipation in the 2 metre depth intervals is indicated by the position of the right side of the bar. The left side is at $10^{-6} cm^2 sec^{-3}$ and the noise level of the system corresponds to a dissipation of $4 \times 10^{-6} cm^2 sec^{-3}$. In regions where no bars have been drawn, both shear signals were extensively contaminated by noise. This usually occurs just below a region of large temperature change.

The estimates of $\bar{\epsilon}_M$ rely upon the sensitivity of the shear probes and the kinematic viscosity of seawater, both of which change with temperature (the pressure effects may be neglected). To account for these changes, the temperature of each 2 metre spectrum, determined from the thermistor output, was used to correct the values of sensitivity and viscosity.

The viscosity was computed from the formula of Miyake and Koizumi (1948). Relative changes in density were less than 0.5% and the average density of all profiles was used for the estimates of $\bar{\epsilon}_M$. (The resulting error in $\bar{\epsilon}_M$ is less than 1% and has been neglected.)

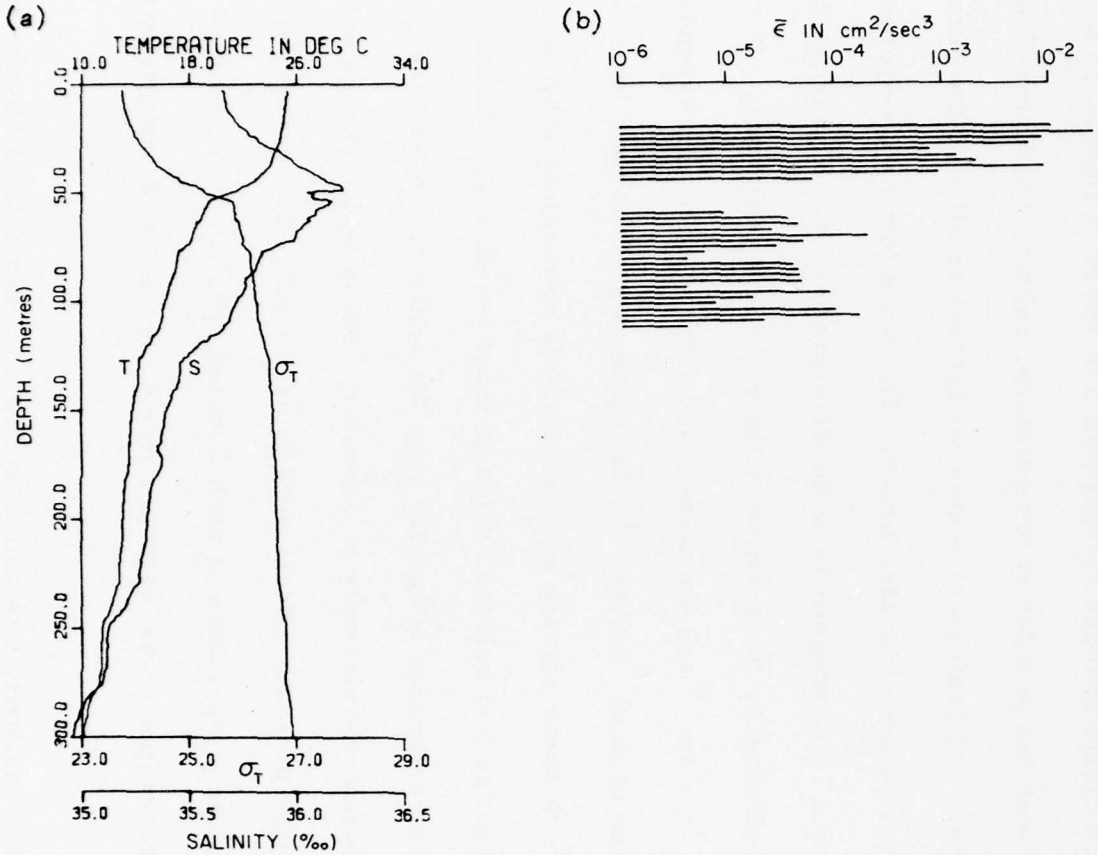

Figure 25 (a) Salinity, temperature and σ_T corresponding to profile 18 (data supplied by E. Katz).

(b) Estimate of the rate of viscous dissipation of profile 18 at 24°0'W, 0°2'N.

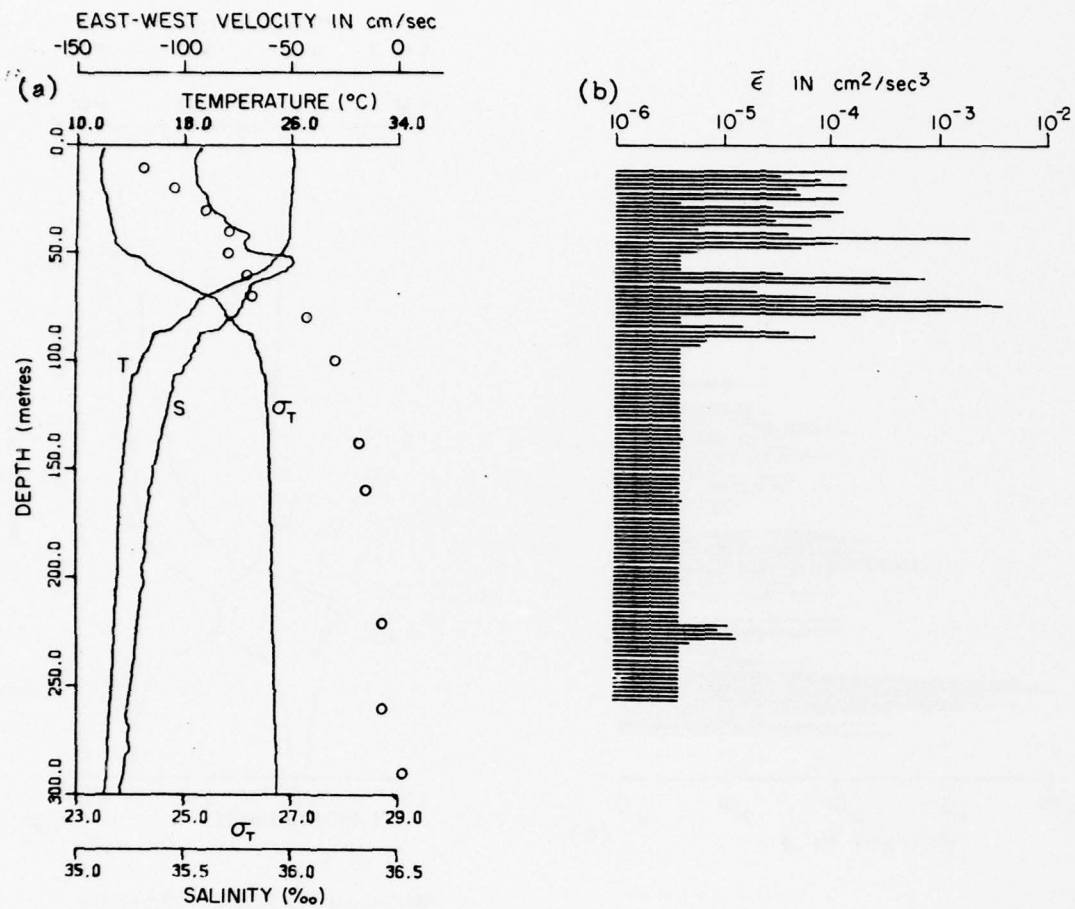

Figure 26 (a) Zonal current relative to 300 metres, salinity, temperature corresponding to profile 20 (data supplied by J. Bruce and E. Katz).

(b) Estimate of the rate of viscous dissipation of profile 20 at 28°11'W, 2°9'N.

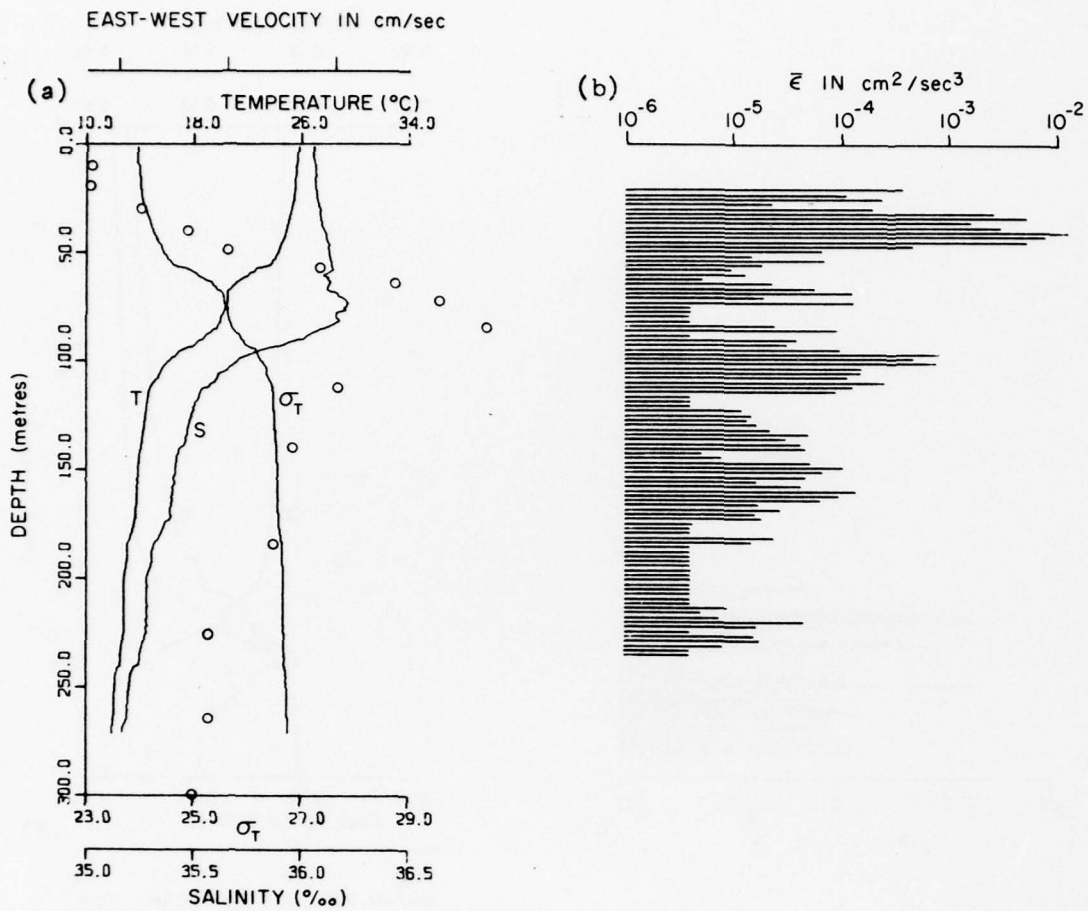

Figure 27 (a) Zonal current relative to 300 metres, salinity, temperature and σ_T corresponding to profile 22 (data supplied by J. Bruce and E. Katz).

(b) Estimate of the rate of viscous dissipation of profile 22 at 28°03'W, 0°37'N.

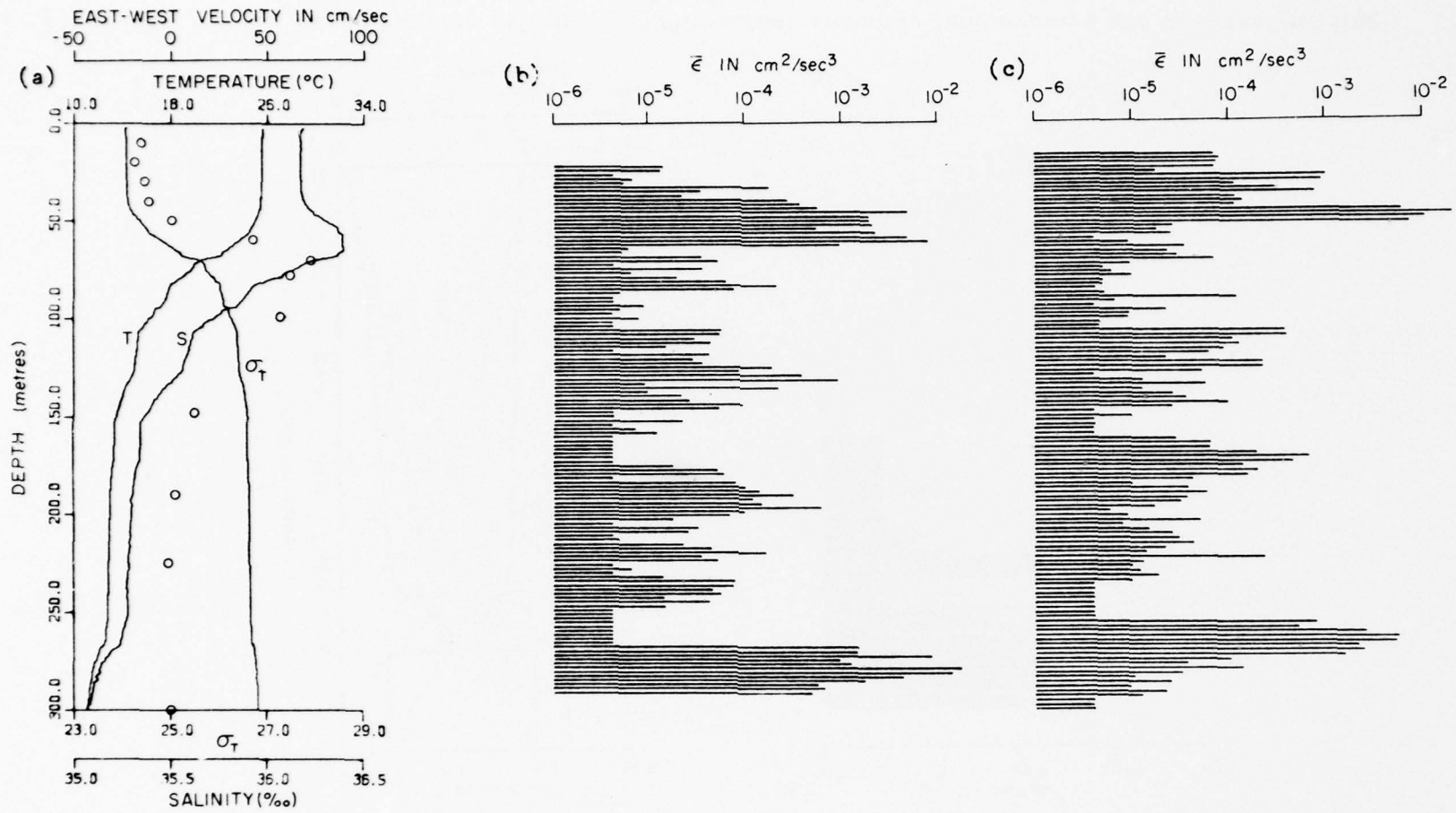

Figure 28 (a) Zonal current relative to 300 metres, salinity, temperature and σ_T corresponding to profiles 23 and 24 (data supplied by J. Bruce and E. Katz).

(b) Estimate of the rate of viscous dissipation of profile 23 at 28°01'W, 0°18'S.

(c) Estimate of the rate of viscous dissipation of profile 24 at 28°03'W, 0°17'S.

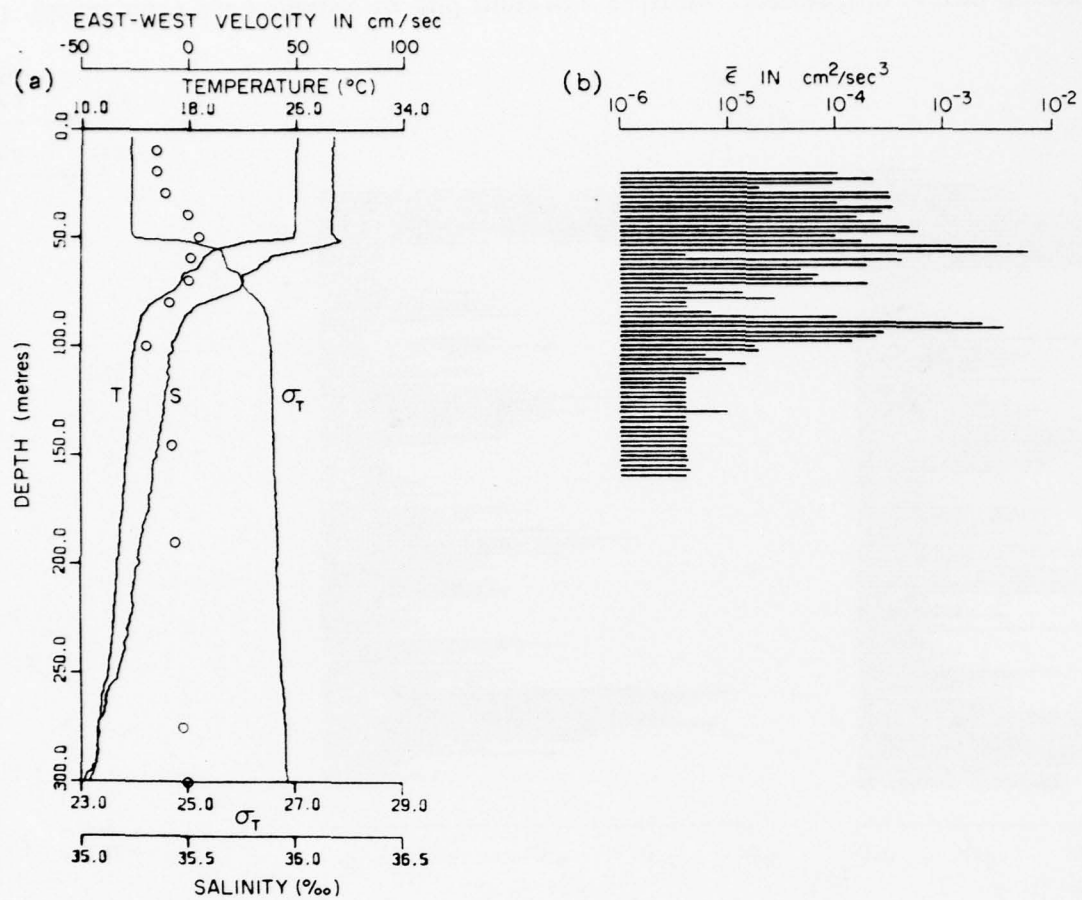

Figure 29 (a) Zonal current relative to 300 metres, salinity, temperature and σ_T corresponding to profile 25 (data supplied by E. Katz and J. Bruce).

(b) Estimate of the rate of viscous dissipation of profile 25 at 28°0'W, 1°21'S.

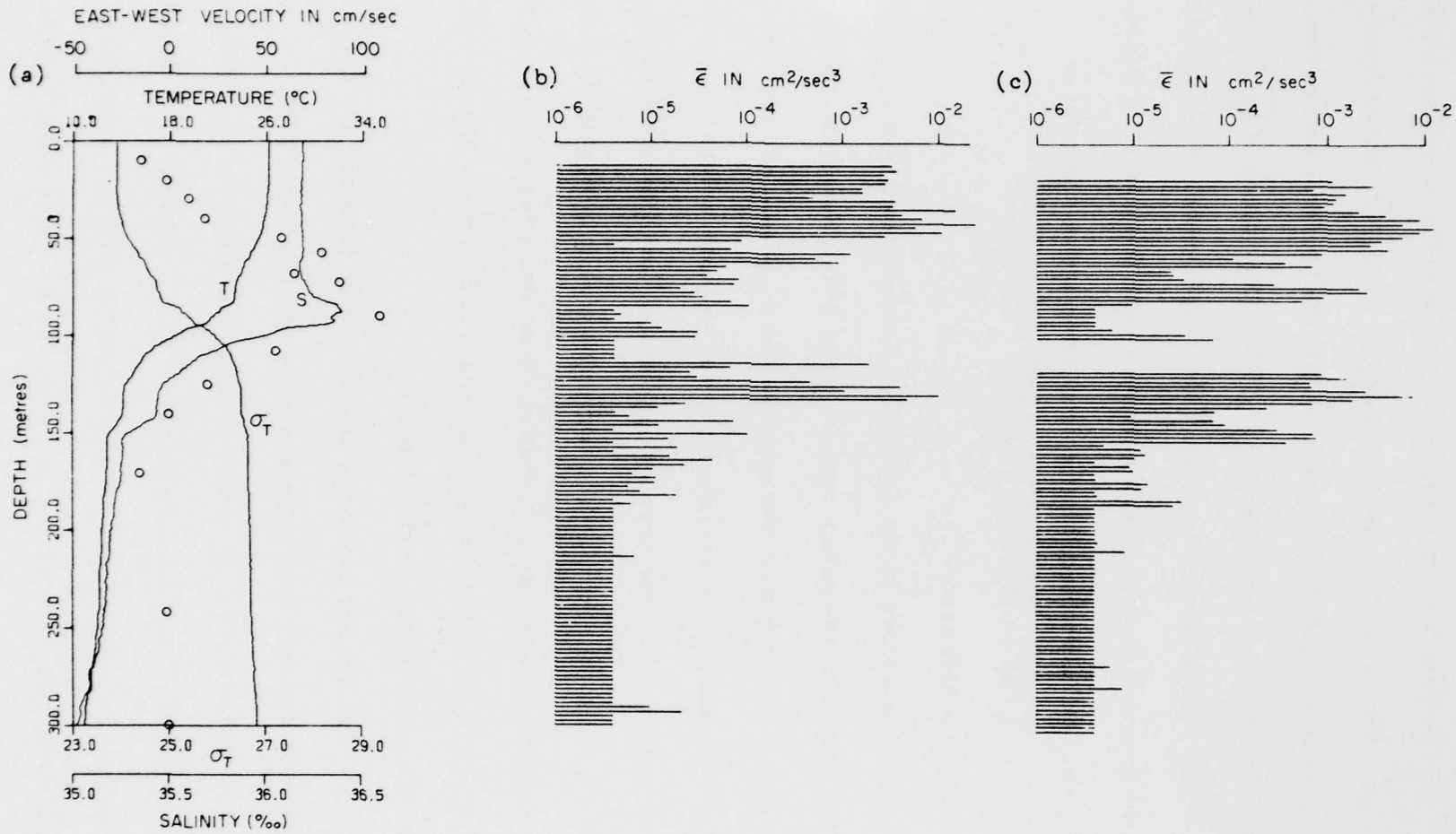

Figure 30 (a) Zonal current relative to 300 metres, salinity, temperature and σ_T corresponding to profiles 28 and 29 (data supplied by J. Bruce and E. Katz).

(b) Estimate of the rate of viscous dissipation of profile 28 near 32°59'W, 0°2'N.

(c) Estimate of the rate of viscous dissipation of profile 29 near 32°59'W, 0°2'N.

The largest factors contributing to the error in estimating $\bar{\epsilon}$ are:

(a) The errors in calculating $\overline{(\frac{\partial u_1}{\partial x_3})^2}$ and $\overline{(\frac{\partial u_2}{\partial x_3})^2}$ derive from errors in the sensitivity ($\pm 20\%$), fall speed ($\pm 3\%$), the spectral summation ($\pm 10\%$) and the circuit constants K_1 and K_2 ($\pm 5\%$). The values of $\overline{(\frac{\partial u_1}{\partial x_3})^2}$ and $\overline{(\frac{\partial u_2}{\partial x_3})^2}$ vary as the square of the sensitivity, the fourth power of the fall speed, the first power of the spectral summation, and the square of the circuit calibration, and assuming these errors are random the total is

$$\left[(.4)^2 + (.12)^2 + (.1)^2 + (.1)^2 \right]^{1/2} \approx .45$$

to give about a 45% error.

(b) The errors in the correction formula (equation 4.2) based upon the scatter of the points appears to be 30%. However, the value of $\frac{\bar{\epsilon}_c}{\bar{\epsilon}_m}$ depends linearly upon the sensitivities S_1 and S_2 and the circuit constants K_1 and K_2. A systematic error in these values could introduce additional errors into the correction formula, and I have allowed a value of 50% for the total errors. The correction formula boosts the value of $\bar{\epsilon}$ by a factor as large as 2.5; that is, it accounts for as much as 60% of the final estimate of the dissipation, and a 50% error in the formula will give a 30% error in the dissipation.

(c) The errors due to the assumption of isotropy are noted in section 2.5, and may lead to an overestimate of almost 50%.

A sum of the errors a+b+c gives a total error of somewhat more than a factor of 2, and the sum $(a^2+b^2+c^2)^{\frac{1}{2}}$ is somewhat less than 2 but it is unlikely that the errors would combine to give the worst case. It is also unlikely that the errors are random, as the sensitivity affects the

errors (a) and (b) in the same direction. Hence the possible error in the dissipations plotted in figures 25 to 30 is a factor of 2.

These dissipation profiles put in quantitative terms the profiles shown in figures 9 to 15. I have discussed the upper mixed layer and upper thermocline in section 4.1, and noted that it is always turbulent above the undercurrent core. As an indication of the relative magnitudes of the dissipations, I have calculated average dissipations over several regions, and compiled them in Table III. Of these eight profiles, six are at or reasonably close to the latitude of the velocity core. Profile 20 is outside the undercurrent, as indicated by the velocity profile in figure 26, and profile 25 was located in a region where the maximum eastward flow had a magnitude of 5 cm/sec. Accordingly, these two are not representative of the undercurrent, but they are of interest.

The question of how representative these six profiles are arises. These are samples through the undercurrent, and although more profiles would be desirable the variation in rates of dissipation above the core from one profile to the next is not large compared to the depth variation of the rate of dissipation for a given profile. For example, the average rate of dissipation in the region of intense turbulence above the core found in profile 18 is $3\frac{1}{2}$ times greater than found in the same region of profile 23, but 200 times greater than typically found in the core. I noted in section 4.1 that this pattern of turbulence was observed above and in the core by other investigators (Gregg, 1976 and Bilodeau, personal communication). This turbulence may be maintained by the Reynolds stress working on the local mean shear, and may not be intermittently generated.

Profile		18	22	23	24	28	29		20	25
Longitude		24°00'W	28°03'W	28°01'W	28°03'W	32°59'W	32°59'		28°11'W	28°00'W
Latitude		0° 02'N	0° 37'N	0° 18'S	0° 17'S	0° 2'N	0° 2'N		2° 9'N	1° 21'S
Intense turbulence above core	depths (m)	20-42	20-46	30-60	20-52	20-60	20-62	Above thermocline	20-45	20-55
	$\bar{\varepsilon}$ ($cm^2 sec^{-3}$)	$7x10^{-3}$	$3x10^{-3}$	$2x10^{-3}$	$3x10^{-3}$	$4x10^{-3}$	$3x10^{-3}$		$2x10^{-4}$	$7x10^{-4}$
Quiet region at core	depths (m)	42-60	46-80	60-103	53-106	60-110	62-115	In thermocline	45-90	55-92
	$\bar{\varepsilon}$ ($cm^2 sec^{-3}$)	—	$4x10^{-5}$	$3x10^{-5}$	$2x10^{-5}$	$3x10^{-5}$	—		$4x10^{-4}$	$4x10^{-4}$
Moderate turbulence below core	depths (m)	60-110	80-112	103-145	106-148	110-130	115-152	Below thermocline	—	92-110
	$\bar{\varepsilon}$ ($cm^2 sec^{-3}$)	$5x10^{-5}$	$2x10^{-4}$	$1x10^{-4}$	$1x10^{-4}$	$2x10^{-3}$	$1x10^{-3}$			$6x10^{-5}$
$\bar{\varepsilon}$ integrated above core ($cm^3 sec^{-3}$)		13	8	6	10	17	14			
$\bar{\varepsilon}$ integrated below core ($cm^3 sec^{-3}$)		.2	.7	.5	.4	4	4			

Table III Averages of estimated dissipation in the thermocline

If one measures a short term current profile through the undercurrent, say of the type taken by Mr. J. Bruce on the ATLANTIS II, it will not differ appreciably (i.e., by more than 50%) from a current averaged over a month or so at the same spot. Hence the large scale shear which generates the turbulence is greatly influenced by the long term average current, and variations in the intensity of turbulence (and also the rate of dissipation) may not be large.

Thus these rates of dissipation in Table III should be representative of the undercurrent. This situation is different than elsewhere in the oceans, where fluctuations of currents are usually much greater than the average.

These rates of dissipation are lower than reported in the literature. The highest average rate is 0.007 $cm^2 sec^{-3}$ for profile 18, and is lower than the rate of 0.08 $cm^2 sec^{-3}$ reported by Williams and Gibson (1974) in the Pacific Equatorial Undercurrent. Moreover, these investigators report similar dissipations at 0° and at 1° N, whereas the values in Table III suggest lower rates of dissipation away from the equator. Values of $\bar{\epsilon}$ reported by Belyaev et al. (1975b) are of order 0.1 $cm^2 sec^{-3}$, and allowing that their reported values for the Atlantic Equatorial Undercurrent represent regions of intense turbulence which may be a factor of ten higher in dissipation than an average over a large region, their values become 0.01 $cm^2 sec^{-3}$, which are greater by a factor of 3 than the average of my estimates. However, their values show no significant depth variation of $\bar{\epsilon}$ between 36 and 140 metres and the results noted in section 4.1 and in Table III indicate that

the rates of dissipation do vary by several factors of ten over these depths.

To attempt to establish the expected magnitude of $\bar{\epsilon}$ at the equator, I have determined the estimated values of rates of exchange of energy among the various terms in the energy balance for the average and fluctuating motions, and these are discussed in the next section.

4.4 Energy Balance in the Undercurrent

(a) Balance for the Fluctuating Motion

Some of the terms in the balance of energy for the average flow must be determined from the balance for the turbulent motion, and this latter balance will be discussed now. The full equation is:

$$\frac{dq^2}{dt} = -\frac{1}{\bar{\rho}}\frac{\partial \overline{u_i p'}}{\partial x_i} - \frac{\partial \overline{u_i q^2}}{\partial x_i} - \overline{u_i u_j}\frac{\partial U_i}{\partial x_j} - \bar{\epsilon} - \overline{\rho' u_3}\, g/\bar{\rho} \qquad 2.11$$

and an average at the latitude of the core over the meandering period of 16 days is desired so that $\frac{\partial}{\partial x_2} \approx 0$. Table IV shows values of $\partial U_1/\partial x_3$ derived from the current meter profiles of Bruce and Katz (1976) and labelled average shear, and the values of $\bar{\epsilon}$ from the Camel. Neither is a 16 day average, but if the individual measurements for the four profiles are averaged, they may represent more closely a long term average at the core. The depths of features of profile 24 do not match those of profile 23, nor those of the CTD, and so profile 24 was not considered.

For each depth interval, I have assumed that $\bar{\epsilon} \approx -\overline{u_1 u_3}\,\partial U_1/\partial x_3$, and have neglected the contribution of $\overline{u_2 u_3}\,\partial U_2/\partial x_3$ to the turbulent energy production. Hence $-\overline{u_1 u_3} \approx \bar{\epsilon}/(\partial U_1/\partial x_3)$ and the computed value is listed in Table IV. Over most depths, the value of $\frac{\partial U_2}{\partial x_3}$ is much

Profile 22

depth (m)	$\frac{\partial U_1}{\partial x_3}$ (sec^{-1})	$\bar{\varepsilon}$ ($\frac{cm^2}{sec^3}$) (x10^3)	$-\rho\overline{u_1u_3}$ ($\frac{cm^2}{sec^2}$) (x10^3)	ν_v ($\frac{cm^2}{sec}$)
20				
30	-.022	.16	-7.3	.3
40	-.023	4.2	-180	8
50	-.017	1.5	-88	5
57.5	-.057	.037	-.065	.01
65	-.049	.030	-.061	.01
72.5	-.027	.091	-3.4	.1
85	-.018	.020	-1.1	.06
112.5	.026	.24	9.2	.4

Profile 23

depth (m)	$\frac{\partial U_1}{\partial x_3}$ (sec^{-1})	$\bar{\varepsilon}$ ($\frac{cm^2}{sec^3}$) (x10^3)	$-\rho\overline{u_1u_3}$ ($\frac{cm^2}{sec^2}$) (x10^3)	ν_v ($\frac{cm^2}{sec}$)
20				
30	-.005	.009	-1.8	.4
40	-.002	.17	-85	40
50	-.012	2.2	-180	15
60	-.042	3.8	-90	2
70	-.031	.20	-6.5	.2
77.5	.023	.015	.65	.03
98	.00024	.037	154	6.4x10^5
148	.0088	.093	11	1

Profile 28

depth (m)	$\frac{\partial U_1}{\partial x_3}$ (sec^{-1})	$\bar{\varepsilon}$ ($\frac{cm^2}{sec^3}$) (x10^3)	$-\rho\overline{u_1u_3}$ ($\frac{cm^2}{sec^2}$) (x10^3)	ν_v ($\frac{cm^2}{sec}$)
20				
30	-.012	1.9	-160	10
40	-.008	7.0	-880	100
50	-.040	8.3	-210	5
57.5	-.020	.40	-20	1
65	-.010	.47	-47	5
72.5	-.027	.059	-2.2	80
90	-.0063	.032	-5.1	1
107.5	.031	.012	.39	.01
125	.020	.73	36	2
140	.013	2.0	150	11

Profile 29

depth (m)	$\frac{\partial U_1}{\partial x_3}$ (sec^{-1})	$\bar{\varepsilon}$ ($\frac{cm^2}{sec^3}$) (x10^3)	$-\rho\overline{u_1u_3}$ ($\frac{cm^2}{sec^2}$) (x10^3)	ν_v ($\frac{cm^2}{sec}$)
20				
30	-.012	1.6	-133	10
40	-.008	3.4	-425	50
50	-.040	7.3	-182	5
57.5	-.020	2.6	-130	7
65	-.010	.30	-30	3
72.5	-.027	.027	-1.0	.001
90	-.0063	.67	-106	20
107.5	.031	.015	.48	.02
125	.020	.69	35	2
140	.013	1.4	107	8

Table IV Values of $\partial U_1/\partial x_3$ from data of Bruce and Katz(1976) and $\bar{\varepsilon}$, and derived values of $-\overline{u_1u_3}$ and ν_v, the vertical eddy viscosity.

smaller than $\frac{\partial U_1}{\partial x_3}$, and $\overline{u_2 u_3}$ will also be smaller (assuming the stress varies as the shear). There are some depths where $\frac{\partial U_2}{\partial x_3}$ is comparable to $\frac{\partial U_1}{\partial x_3}$, but these are in the core or shallow depths away from the region of highest dissipation, and will not greatly influence the evaluation of terms in equation 2.11, which is discussed in the following paragraphs. The assumption that production equals dissipation over the depth interval may not be strictly true, as the other terms may be significant. However, production and dissipation must be the same magnitude and use of this approximation allows estimates of other terms which allows justification of the assumption.

Above the core a typical derived value of $|\overline{u_1 u_3}|$ is then about .25cm^2/sec^2 in the region of highest dissipation and this is the square of the friction velocity u_*. Monin and Yaglom (1971, p. 401) estimate for a turbulent shear flow in a stratified medium that $\overline{q^2 u_3}$ and $\overline{p' u_3}/\bar{\rho}$ are of order u_*^3. Smith (1974) has found $\overline{u_3 q^2} \leq .05 u_*^2 U_1$ in the surface layer of the atmosphere and since $U_1 \approx 25 u_*$ his data yield $\overline{u_3 q^2} \approx u_*^3$, a result consistent with Monin and Yaglom's statement. I shall take $2u_*^3 = .25$ cm^{3}sec^{-3} as an estimate of the terms $\overline{u_3 q^2}$ and $\overline{p' u_3}/\bar{\rho}$.

Gradients of quantities in the x_1 direction will be much smaller than gradients in the x_3 direction, and may be neglected (except for $\frac{U_1 \partial q^2}{\partial x_1}$ which must be similar to $U_3 \partial q^2/\partial x_3$). For a coefficient of correlation of 0.1 between u_1 and u_3, one has $(\overline{u_1^2}\,\overline{u_3^2})^{\frac{1}{2}} \approx 10\ |\overline{u_1 u_3}| \approx 2.5$ cm^2/sec^2 and $(\overline{u_1^2})^{\frac{1}{2}} \approx (\overline{u_3^2})^{\frac{1}{2}} \approx 1.6$ cm/sec. (Actually one expects $(\overline{u_1^2}) > (\overline{u_3^2})$, but for scaling choose them to be equal.) Hence $q^2 \approx 4$ cm^{2}sec^{-2}.

A scale height may be taken as the depth from a region of large $\bar{\epsilon}$ to one where $\bar{\epsilon}$ is low, about 20 metres, and a mean velocity scale of about 80 cm/sec may be assumed; and choose 10° longitude as a zonal length scale and 1 day as a time scale. The value of U_3 is about 10^{-3} cm/sec and will be discussed in the next section. The buoyancy term is assumed about 0.15 of the production term (Turner, 1973) although experimental evidence in free shear flows is sparse . (The ratio of buoyancy to production terms is the flux Richardson number, discussed in section 2.5.) Equation 2.11 is now

$$\frac{\partial q^2}{\partial t} + U_3\frac{\partial q^2}{\partial x_3} + U_1\frac{\partial q^2}{\partial x_1} = -\frac{1}{\bar{\rho}}\frac{\partial \overline{u_3 p'}}{\partial x_3} - \frac{\partial \overline{u_3 q^2}}{\partial x_3} - \overline{u_1 u_3}\frac{\partial U_1}{\partial x_3} - \bar{\epsilon} - \overline{\rho' u_3}\, g/\bar{\rho}$$

$$\frac{4}{10^5} \quad \frac{10^{-3}\times 4}{2\times 10^3} \quad \frac{80\times 4}{10^8} \quad \frac{0.25}{2\times 10^3} \quad \frac{0.25}{2\times 10^3} \quad 3\times 10^{-3} \quad 3\times 10^{-3} \quad 5\times 10^{-4}$$

I have chosen most scales to give an upper limit to the terms compared to $\bar{\epsilon}$. For example, 0.1 is probably a low correlation coefficient. In the atmospheric surface layer a value of 0.3 is typical. The advective terms are so small that the value used is not critical. It is conceivable that the buoyancy term could be up to .2 of the production term, but this value is not significant considering the uncertainty of the values $\bar{\epsilon}$ and $\partial U_1/\partial x_3$, so the basic balance is local production of turbulence equals local dissipation.

Below the core, for most profiles, $\bar{\epsilon}$ is smaller by a factor of 3 to 10, but other terms drop correspondingly and the balance is still dissipation ≈ production.

(b) Vertical Eddy Viscosity

In a turbulent shear flow, the Reynold's stress is often expressed

as

$$-\rho\overline{u_1 u_3} = \rho \nu_v \frac{\partial U_1}{\partial x_3} \qquad 4.3$$

(Hinze, 1959, p. 466) where ν_v is the vertical eddy viscosity. Hence

$$\nu_v = -\frac{\overline{u_1 u_3}}{\partial U_1/\partial x_3} = \frac{\bar{\epsilon}}{(\partial U_1/\partial x_3)^2} \qquad 4.4$$

I have calculated values of ν_v for the depths between the current meter readings for profiles 22, 23, 28 and 29 in Table IV. The value of ν_v peaks at between 8 and 100 in the high dissipation regions, and decreases in magnitude near the core to values less than 0.1. The magnitude increases somewhat below the core to values ranging between 0.4 and 11 $cm^2 sec^{-1}$. It is expected that the value of vertical eddy viscosity decreases as stratification increases (Turner, 1973) and the lower values of ν_v in the core correspond to regions of largest average density gradients. Thus it does not seem possible to assign a single value to ν_v for the undercurrent. However, in the region of large dissipation and large average shear, the order of magnitude of ν_v is 10 $cm^2 sec^{-1}$. Much of the large scatter is due to the different sampling times and durations for the large scale currents and the microscale shears.

(c) Balance for the Average Motion

Again, a time average over the meander period is desired, and meridional terms (i.e., in the x_2 direction) are assumed small at the equator. In this case, there are observations of several components of terms in the energy balance averaged over the GATE Phases of about 20

days each. A compendium of measurements of anomalies of dynamic heights along the equator for each of the three Phases of GATE has been prepared by Katz et al (1976) and the first two Phases are illustrated in figure 31. The dynamic heights shown correspond to zonal pressure gradients $\frac{1}{\bar{\rho}}\frac{\partial \bar{P}}{\partial x_1}$, of -3.2 and -2.2×10^{-5} dynes/gm for the surface and 50 decibar depths during and before Phase I, and -7.3 and -5.3×10^{-5} dynes/gm during Phase II.

The change in slopes between Phases I and II is large, and is mainly based upon measurements west of 35°W during Phase II, not available during Phase I. It can be seen that the slope of equal pressure surfaces decreases with depth through the undercurrent. A diagram of the change of zonal pressure with depth has been prepared by Bubnov et al.(1975) and is shown in figure 32 along with velocity profiles from moored current metres.

The equation for the balance of kinetic energy of the average flow is

$$\frac{\partial Q^2}{\partial t} = -\frac{U_i}{\bar{\rho}}\frac{\partial \bar{P}}{\partial x_i} - \frac{\partial U_i Q^2}{\partial x_i} - \frac{\partial U_i \overline{u_i u_j}}{\partial x_j} + \overline{u_i u_j}\frac{\partial U_i}{\partial x_j} \qquad 2.7$$

We can try the scales estimated in the treatment of the fluctuating flow to determine the magnitude of the divergence term $-\frac{\partial U_i \overline{u_i u_j}}{\partial x_j}$ in equation 2.7, however the individual components in this term are also those in the last term $\overline{u_i u_j}\frac{\partial U_i}{\partial x_j}$, and only the position of the derivative is changed for the terms. Scaling will not show which term is larger.

To handle the term $-\frac{\partial U_i \overline{u_i u_j}}{\partial x_j}$, equation 2.7 may be integrated over a

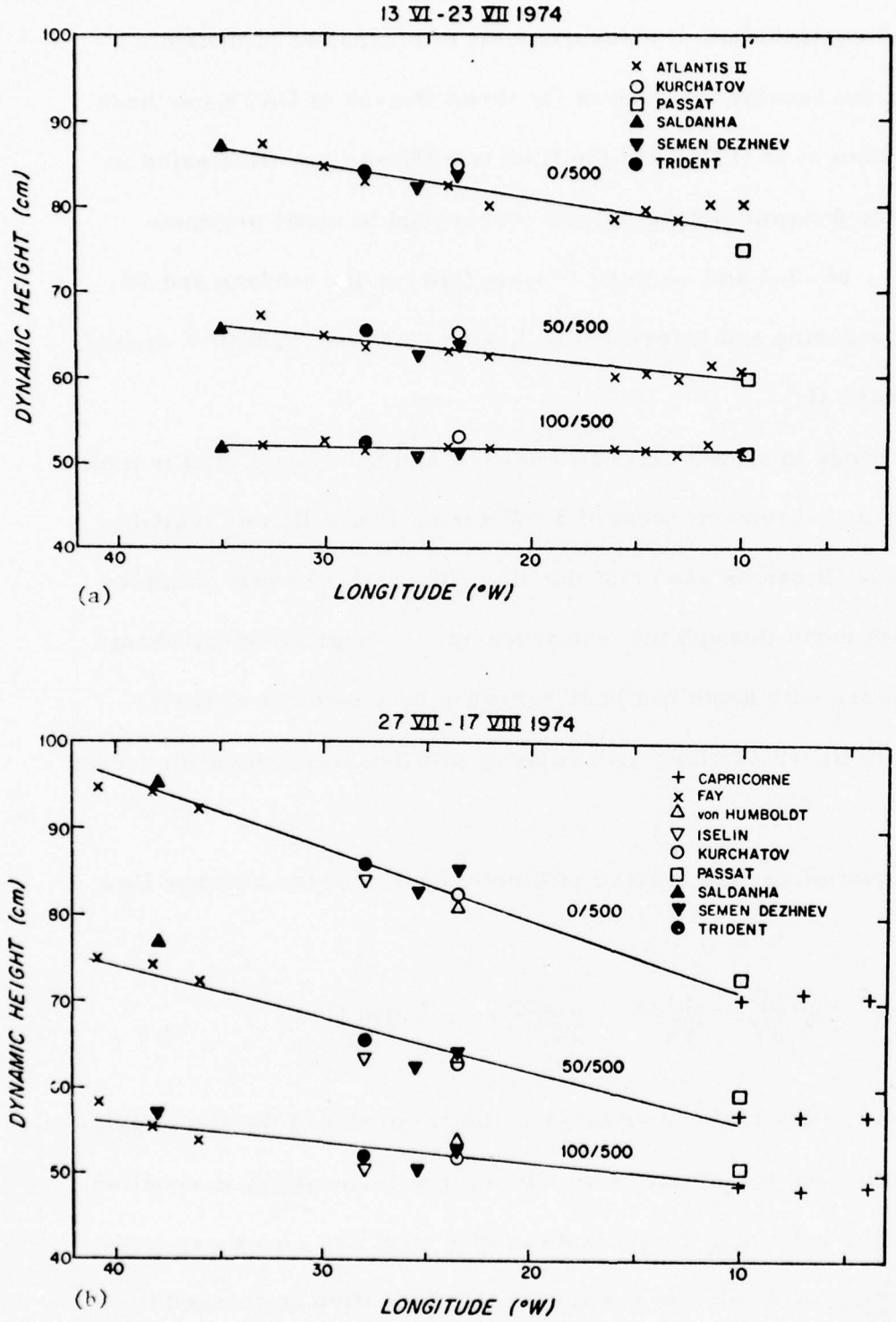

Figure 31 Anomaly of dynamic height of the 0, 50 and 100 dbar surfaces relative to the 500 dbar surface (a) before and during Phase I of GATE and (b) during Phase II of GATE. Data points east of 10°W are excluded from the regression (from Katz et al, 1976).

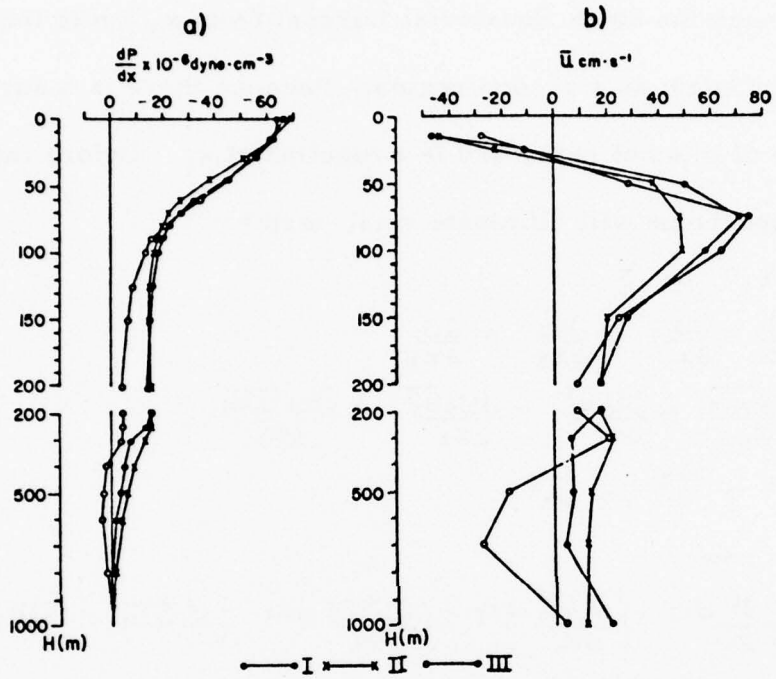

Figure 32 Vertical distribution of (a) mean east-west pressure gradient between 23°30'W and 10°W and (b) mean profile of the zonal current at 23°30'W. (Düing 1975, figures provided by V.Bubnov) The change in velocity for Phase II is likely due to a shift of the undercurrent to the south.

depth range in the x_3 direction. An integral from the core of the undercurrent at $x_3 = a$ (about 90 to 60 metres depth) to the depth where $U_1 = 0$ at $x_3 = b$ (about 35 metres) may be considered as one region, and an integration through the South Equatorial Current from $x_3 = b$ to the surface at $x_3 = c$ may be taken as a second region. Because there is a surface slope the value of c is not zero, and is a function of x_1. Before integrating, some comparisons will eliminate small terms.

$$
\begin{aligned}
& U_3 \ll U_1 \\
& \frac{\partial U_3}{\partial x_1} \ll \frac{\partial U_1}{\partial x_1} \approx \frac{\partial U_3}{\partial x_3} \ll \frac{\partial U_1}{\partial x_3} \\
& \frac{\partial U_3 \overline{u_1 u_3}}{\partial x_1} \ll \frac{\partial U_1 \overline{u_1^2}}{\partial x_1} \approx \frac{\partial U_3 \overline{u_3^2}}{\partial x_3} \ll \frac{\partial U_1 \overline{u_1 u_3}}{\partial x_3} \qquad 4.5 \\
& \overline{u_1^2} \approx \overline{u_2^2} \approx \overline{u_3^2}
\end{aligned}
$$

The equation is now

$$
\int \frac{\partial Q^2}{\partial t} dx_3 = -\int \frac{U_1}{\bar{\rho}} \frac{\partial \bar{P}}{\partial x_1} dx_3 - \int \frac{\partial U_1 Q^2}{\partial x_1} dx_3 - \int \frac{\partial U_3 Q^2}{\partial x_3} dx_3 - \left[U_1 \overline{u_1 u_3} \right] + \int \overline{u_1 u_3} \frac{\partial U_1}{\partial x_3} dx_3 \qquad 4.6
$$

The magnitude of the last term is about the same as the dissipation, as shown in the last sub-section. From Table III, the average integrated value of $\bar{\epsilon}$ from 20 metres depth to the core is somewhat less than 12 cm^3 sec^{-3} and only profiles 28 and 29 have large dissipations above 20 metres depth, so 12 $cm^3 sec^{-3}$ may represent a typical value from the surface to core. There is no clear tendency for this dissipation to be concentrated more strongly in either the undercurrent or the South Equatorial Current.

To evaluate the terms in equation 4.6, average values over the region of integration should be considered. I can assume that an average value of Q^2 between a and b is $80^2/4$ cm^2/sec^2 as Q^2 is $\frac{80^2}{2}$ at the core ($x_3 = a$) and 0 at the level of no zonal motion ($x_3 = b$) and the variation in

Q^2 between $x_3 = a$ and $x_3 = b$ is reasonably close to linear. An average value for the thickness of the upper portion of the undercurrent is 40 metres. The term $-\int_a^b \frac{\partial Q^2}{\partial t} dx_3$ is, assuming a change of flow of 10% per month for the undercurrent $\frac{\left(\frac{90^2}{4} - \frac{80^2}{4}\right)}{3 \times 10^6} \times 4 \times 10^3 \approx \pm 1 \text{ cm}^3 \text{sec}^{-3}$. A significant change in transport of the undercurrent has not been reported for the three Phases of GATE. I have assumed that a change of more than 10% per month in the flow of the undercurrent would have been observed. In the South Equatorial Current, a larger percentage change may have taken place, but the velocities were somewhat lower, and this term is of similar magnitude.

The term $-\int \frac{U_1}{\bar{\rho}} \frac{\partial \bar{P}}{\partial x_1} dx_3$ may be determined from the graphs of U_1 and $\frac{\partial \bar{P}}{\partial x_1}$ in figure 32, or from the anomalies of dynamic height in figure 31 plus estimates of U_1 from other sources. The pressure gradient is derived from the anomaly of dynamic height $\Delta D(P)$ by assuming the reference level is indeed on a constant geopotential surface; then

$$-\int_a^b \frac{U_1}{\bar{\rho}} \frac{\partial \bar{P}}{\partial x_1} dx_3 = 10^3 \int_{\bar{P}(a)}^{\bar{P}(b)} \frac{U_1}{g\bar{\rho}} \frac{\partial \Delta D(P)}{\partial x_1} d\bar{P} \qquad 4.7$$

where $\Delta D(P)$ is in dynamic centimetres, and a similar expression is found for the integral from $x_3 = b$ to $x_3 = c$. From figure 32, it can be seen that the integrand changes sign at the level of no motion. The estimated values of this term over the two regions are

$$\int_b^c \frac{U_1}{\bar{\rho}} \frac{\partial \bar{P}}{\partial x_1} dx_3 \approx -6 \text{ cm}^3 \text{sec}^{-3}$$

$$\int_a^b \frac{U_1}{\bar{\rho}} \frac{\partial \bar{P}}{\partial x_1} dx_3 \approx +5 \text{ cm}^3 \text{sec}^{-3}$$

based upon a simple integration of the values in figure 32, which have been

modified in the following way: the values for U_1 in figure 32 are derived from averages of three current meters at 32'S, 40'N and 01'N. The average current at the equator may be greater than the indicated value of 70 cm/sec in figure 32 by about 10 cm/sec, and accordingly a speed of 80 cm/sec has been taken for scaling the core velocity. Also the speed near the surface may be too high. The current meters were attached to surface floats, which may have increased apparent surface speeds by wave "pumping". A typical value for surface currents measured from the ATLANTIS II is about -30 cm/sec and this value has been used.

Note that the slopes of the 0, 50 and 100 dbar surfaces in figure 31 indicated by those ships (KURCHATOV and PASSAT) which obtained the data of figure 32 lie between the slope indicated for Phase I and that of Phase II, and thus are representative of the average pressure gradients observed by all ships during the first two Phases of GATE. The observations of figure 32 have been used for analysis because they show the variation of $\frac{\partial \bar{p}}{\partial x_1}$, with depth in greater detail.

The two divergence terms may be considered together, and may be rewritten as

$$\int_{a(x_1)}^{b} \frac{\partial U_1 Q^2}{\partial x_1}\, dx_3 = \frac{d}{dx_1} \int_{a(x_1)}^{b} U_1 Q^2\, dx_3 + \frac{\partial a(x_1)}{\partial x_1} \left[U_1 Q^2 \right]^{x_3 = a(x_1)}$$

$$\int_{a(x_1)}^{b} \frac{\partial U_3 Q^2}{\partial x_3}\, dx_3 = \left[U_3 Q^2 \right]_{a(x_1)}^{b} \qquad 4.8$$

I have denoted the level of the velocity core as $a(x_1)$, because the core rises toward the east in the Atlantic. Bruce and Katz (1976) observed the core of the undercurrent to rise by about 30 metres between 33° W and 10°W, and this figure is supported by other data (Düing, 1975). There

is no evidence that the level of no zonal velocity ($x_3 = b$) is a function of x_1. There is also evidence that the vertical velocity <u>at</u> the core is the vertical velocity <u>of</u> the core; in other words, there is no net transport upward through the core. The salinity maximum associated with the velocity core would likely decay at a more rapid rate than observed if there was a significant upwelling velocity through the core. Also, one would expect the isotherms to ridge or trough at the depth of the core if upwelling or downwelling were significant.

In this case, the upward slope of the undercurrent core toward the east is the ratio: $\frac{\partial a(x_1)}{\partial x_1} = \frac{U_3}{U_1}$ and two terms in equation 4.8 cancel

$$\frac{\partial a(x_1)}{\partial x_1}\left[U_1 Q^2\right]^{x_3 = a(x_1)} = \left[U_3 Q^2\right]_{x_3 = a(x_1)}$$

The value of U_3Q^2 at $x_3 = b$ is zero because $Q^2 \approx 0$ there. Thus, there remains only the term

$$\frac{d}{dx_1}\int_{a(x_1)}^{b} U_1 Q^2 \, dx_3$$

Two effects contribute to this term: because the core of the undercurrent rises and the level of no motion remains reasonably uniform, there will be a change in the value of the integral along the x_1 direction; secondly, the average value of U_1Q^2 may change in the x_1 direction. To evaluate the first effect, assume that the thickness of the portion of the undercurrent between $x_3 = a$ and b decreases by 30 metres from 33° W to 10° W, but the average energy density there remains the same: $\frac{(80^2)}{4}\frac{\text{cm}^2}{\text{sec}^2}$. The term becomes

$$-\frac{d}{dx_1}\int_{a(x_1)}^{b} U_1 Q^2 \, dx_3 = -\frac{\frac{80}{\sqrt{2}}\left(80^2/4\right)(-3\times 10^3)}{2.3\times 10^8} \approx 1 \ \frac{\text{cm}^3}{\text{sec}^3}$$

To evaluate the effect of a change in flow speed, assume that U_1 changes by 10% in 10° of latitude between 33°W and 10°W. Reported measurements during GATE show no clear trend for a change in U_1 along the equator, and I am assuming that a change of more than 10% per 10° longitude would have been sensed. The term in this case is

$$\frac{d}{dx_1}\int_{a(x_1)}^{b} U_1 Q^2\, dx_3 = \pm \frac{\left[\frac{88}{\sqrt{2}}\left(\frac{88^2}{4}\right) - \frac{80}{\sqrt{2}}\left(\frac{80^2}{4}\right)\right] 4\times 10^3}{10^8} = \pm 1 \frac{cm^3}{sec^3}$$

where the average values of U_1 over the limit of integration are taken as $88/\sqrt{2}$ and $80/\sqrt{2}$. Of course, at the eastern and western extremes of the undercurrent, $U_1 = 0$, and this term will become larger. In the South Equatorial Current this term is an order of magnitude smaller, because the value of U_1 is much less.

The term $-U_1\overline{u_1 u_3}$ may be determined from the average velocity at the surface ($U_1 \approx -30$cm/sec). A yet to be published survey by Dr. A. Bunker of Woods Hole of atmospheric winds at the equator gives an average value of the zonal wind stress $-\rho\overline{u_1 u_3} \approx -0.5$ dynes/cm^2 (Katz et al, 1976) and so $-\overline{u_1 u_3} \approx -.5$ cm^{2}sec^{-2} at the surface. Hence $-U_1\overline{u_1 u_3} \approx 15$ cm^3 sec^{-3} at the surface. At the core, $\overline{u_1 u_3} = 0$ should hold because $\partial U_1/\partial x_3 = 0$ and $\overline{u_1 u_3}$ changes sign through the core. At the level of no zonal velocity $U_1\overline{u_1 u_3} = 0$, because $U_1 = 0$.

Table V shows the estimated values of the significant terms of equation 4.6. These values may be considered typical between 10°W and 33°W for the currents in July 1974. I have portioned the terms between the South Equatorial Current and the Atlantic Equatorial Undercurrent above the core. The pressure gradient varies by about 100% from Phase I

$$\int \frac{\partial Q^2}{\partial t}\, dx_3 = -\int \frac{U_1}{\bar{\rho}} \frac{\partial \bar{P}}{\partial x_1}\, dx_3 \quad -\frac{d}{dx_1}\int U_1 Q^2\, dx_3 \; - [U_1 \overline{u_1 u_3}] \quad + \int \overline{u_1 u_3} \frac{\partial U_1}{\partial x_3}\, dx_3$$

$x_3=c$					+15	
South Equatorial Current	±1	=	-6	0		-6
$x_3=b$					0	
Equatorial Undercurrent	±1	=	5	1±1		-6
$x_3=a$					0	

Table V Estimates of the vertically integrated rates of average energy transfer at the equator. Each term has units of $cm^3 sec^{-3}$.

to Phase II in figure 31 and estimates of $\bar{\epsilon}$ are available only for the western portion (24°W, 28°W and 33°W), and may be in error by a factor of 2 and other values are not likely to be more accurate.

It is difficult to estimate the magnitude of the meridional terms. The averaging has been considered at the equator, where the terms $\frac{U_2}{\rho}\frac{\partial \bar{P}}{\partial x_2}$ and $\overline{u_1 u_2}\frac{\partial U_1}{\partial x_2}$ are zero, and for the case where a meander was present, but not growing in amplitude. The meridional terms $\frac{\partial U_1 \overline{u_1 u_2}}{\partial x_2}$ and $\frac{\partial U_2 Q^2}{\partial x_2}$ are not zero at the equator, but could be small compared to terms such as $\frac{U_1}{\rho}\frac{\partial \bar{P}}{\partial x_1}$. Rather than try to evaluate these terms, one can consider the rate of energy loss from the average flow to a meander which is growing in amplitude. These sixteen day meanders were the most energetic of the large scale fluctuations observed during GATE, and the rate of energy flow to a growing meander may give an upper limit to the meridional terms at the equator.

As the meander in the undercurrent grows and sweeps back and forth across the equator, it reduces the average velocity observed at the core from about 100 cm/sec to about 80 cm/sec. If the meander period of 16 days is a time scale for growth of the meander, then

$$\int_a^b \frac{\partial Q^2}{\partial t}\, dx_3 = \frac{\left[\frac{80^2}{4} - \frac{100^2}{4}\right] 4 \times 10^3}{1.3 \times 10^6} = -3 \text{ cm}^3/\text{sec}^3$$

represents the rate of energy loss from the average flow, integrated from the core to the depth of no motion. The magnitude of the term is one half of the integrated zonal pressure gradient term, so one can expect that in some cases, the meridional terms may not be negligible.

A theoretical study of these meanders by Philander (1976) indicates that the Atlantic Equatorial Undercurrent is likely stable to meanders, but

the westward flowing South Equatorial Current could be unstable, and "perturbations generated by the instability in the surface layers will cause the subsurface undercurrent to meander". The energy flow for this meander is from the average flow of the undercurrent to the meander.

Although the meridional terms may be important in the energetics of the undercurrent, the region I have chosen for consideration at the equator between the core and the surface is where the zonal and vertical terms will be relatively large, and the meridional terms relatively small, and except for the case of a growing meander, meridional terms should be unimportant. Away from the equator, and at the depth of the core, these meridional terms must contribute to the energy balance, and I expect that some of the current meters moored during GATE may give estimates of these terms.

The terms shown in Table V for the balance of energy of the average motion indicate that the wind stress puts energy into the pressure field found in the South Equatorial Current, and a portion of it is dissipated. In the Atlantic Equatorial Undercurrent above the core, the basic balance is between energy removed from the pressure field, advected by the flow and lost by dissipation. The values in Table V do not balance exactly, but do agree within the error limits.

For the portion of the undercurrent below the core, the rate of dissipation is smaller than the rate found above the core. The zonal pressure gradient is also smaller here, and puts energy into both the viscous dissipation and the advective acceleration terms (this region

becomes thicker downstream and flows faster and both effects take energy from the pressure gradient).

The general agreement of the terms in Table V is encouraging, and increases confidence in the degree to which the eight microstructure profiles are representative of the nature of the undercurrent at the equator.

I believe this is the first time that measurements for this type of energy balance have been taken, and the undercurrents are the only currents for which a balance as simple as this may be considered. In other current systems, the balance of energy is not as simple, due to the relatively small values of the mean velocities compared to fluctuating velocities, and the difficulty in measuring the relatively small cross-isobar flows. However, it is worthwhile to measure the rates of dissipation in the oceans, and for special regions such as the upper mixed layer it may be that terms such as $\overline{u_1 u_3}\frac{\partial U_1}{\partial x_3}$ may be computed from the estimates of $\bar{\epsilon}$, and the scales at which mixing takes place may be determined.

SUMMARY AND CONCLUSIONS

During the GATE project in 1974, undertaken in the tropical Atlantic Ocean, a free-fall instrument was employed to measure vertical microstructure gradients of temperature and horizontal velocity. These gradient measurements are at size scales where the turbulent energy is converted to heat by viscous dissipation, and temperature gradients are smoothed by molecular diffusion. A portion of the rate of viscous dissipation can be measured directly by a probe on the instrument and the remaining portion is estimated, and because regions where the rate of viscous dissipation is large are generally regions of large turbulent intensity, one can compare the relative turbulent intensities at various depths.

The microstructure measurements at the equator show the most intense turbulence is at the boundary between the upper mixed layer and the undercurrent, where the average shear $\frac{\partial U_1}{\partial x_3}$ is large. Through the core the turbulence is much less active and is distributed intermittently through this region. Below the core of the undercurrent, at the base of the thermocline, moderately intense turbulence was always observed. Below the thermocline the turbulence is of variable intensity, usually weak, but occasionally, as found in profiles 23 and 24, some turbulence as active as that found above the undercurrent was observed.

Spectra of turbulence in the upper mixed layer show a consistent roll-off from the expected universal Kolmogoroff curve at frequencies above 10 Hz (wavelengths less than 4 cm). I have interpreted this roll-

off as due to spatial averaging of the shear probe, and have compared rates of dissipation $\bar{\epsilon}_U$ estimated from the fit of the measured spectra to the universal curve with the dissipation $\bar{\epsilon}_M$ determined directly from the measurements of $\frac{\partial u_1}{\partial x_3}$, and $\frac{\partial u_2}{\partial x_3}$, and found $\bar{\epsilon}_U$ was consistently greater than $\bar{\epsilon}_M$. In regions of very intense turbulence, where dissipations are high and scales of turbulence in the dissipation range extend to very small wavelengths, $\bar{\epsilon}_U/\bar{\epsilon}_M$ is large, up to 2.5 for Kolmogoroff wavenumbers of 10 cm^{-1}. A correction formula has been determined to boost the estimates of dissipation to account for this spatial averaging. Thus, the assumption of isotropy is invoked to predict the magnitude of the unmeasured terms in the expression for $\bar{\epsilon}$, and also to compensate for the high wavenumber portion of the $\frac{\partial u_1}{\partial x_3}$ and $\frac{\partial u_2}{\partial x_3}$ signals which was missed because of spatial averaging. The expected error in $\bar{\epsilon}$ is a factor of 2.

It is possible to estimate terms in the energy balance for the fluctuating motion and for the average motion from these microstructure scale measurements and measurements of large scale features by other investigators. When the terms in the energy equation for the fluctuating flow are scaled, it is found that a balance between local production and local dissipation of turbulent energy exists where turbulence levels are high. Other terms in the equation are about a factor of ten smaller in magnitude. This balance allows estimation of the loss to turbulence in the average energy equation.

Measurements of large scale features during GATE (as noted by Düing et al, 1975) revealed a 16 day $\pm$2 day meander of the undercurrent.

As measurements by many investigators extend over an entire 20 day or so Phase of GATE, it is possible to average some readings over the meander period. Katz et al.(1976) have summarized the zonal pressure gradient data for each of the three Phases of GATE. Bubnov (Düing, 1975) has averaged the zonal velocity at 23.5°W and the pressure gradient between 23.5° and 10°W over each of the three Phases of GATE. These measurements, together with the microstructure measurements allow estimates of the zonal and vertical terms in the equation for the kinetic energy of the average flow, and terms are evaluated in the region of the equator above the core of the undercurrent where meridional terms are expected to be relatively small.

When the equation for the average flow is integrated between the ocean surface and the depth of no zonal velocity, it is found that the rate of kinetic energy gain from the zonal wind stress is balanced by the rate of transfer of energy into the pressure field and the rate of viscous energy dissipation. An integration from the core to the depth of no zonal velocity shows that the rate of increase of kinetic energy from the zonal pressure gradient, which now drives the current, is balanced by the rate of energy loss by viscous dissipation. The advection of kinetic energy by the flow is probably smaller but may not be negligible.

REFERENCES

Abramovich, G. N. (1963) The Theory of Turbulent Jets. MIT Press, Cambridge, Mass.

Allen, H. J. and E. W. Perkins (1952) A study of effects of flow over slender inclined bodies of revolution. National Advisory Council for Aeronautics Report No. 1048.

Batchelor, G. K. (1959) Small scale variation of convected quantities like temperature in turbulent fluid. Part 1: General discussion and the case of small conductivity. J. Fluid. Mech. 5 113-133.

Belyaev, V. S., A. N. Gezentsvey, A. S. Monin, R. V. Ozmidov and V. T. Paka (1975a) Spectral characteristics of small scale fluctuations of hydrophysical fields in the upper layer of the ocean. J. Phys. Oc. 5 492-498.

Belyaev, V. S., M. M. Lubimtzev and R. V. Ozmidov (1975b) The rate of dissipation of turbulent energy in the upper layer of the ocean. J. Phys. Oc. 5 499-505.

Boston, N. E. J. (1970) An investigation of high wavenumber temperature and velocity spectra in air. Ph. D. Thesis, Inst. of Oceanography, University of British Columbia.

Bowden, K. F. (1962) Turbulence. The Sea Volume I ed. by M. H. Hill Interscience Publishers, New York, 802-825.

Bradshaw, P. (1964) Experimental Fluid Mechanics MacMillan, New York, 210 pp.

Bruce, J. G. and E. J. Katz (1976) Observations in the Equatorial Atlantic during GATE, June and July 1974 from Atlantis II. Woods Hole Oc. Inst. Tech. Rep. 76-54 90pp.

Bubnov, V. A., K. V. Moroshkin and V. D. Egorikhin (1975) Variability of current structure and associated oceanographic fields in the Equatorial Atlantic. Report to GATE Equatorial and A-Scale Informal Workshop held at WMO, Geneva.

Cromwell, T., R. B. Montgomery and E. D. Stroup (1954) Equatorial Undercurrent in Pacific Ocean revealed by new methods. Science, 119 648-649.

Düing, W. (1975) Report of the Equatorial and A-Scale Informal Workshop. Held at WMO, Geneva.

Düing, W., P. Hisard, E. Katz, J. Meinke, L. Miller, K.V. Moroshkin, G. Philander, A.A. Rybnikov, K. Voigt and R. Weisberg (1975) Meanders and long waves in the Equatorial Atlantic. Nature 257 280-284.

Gargett, A. E. (1976) An investigation of the occurrence of oceanic turbulence with respect to finestructure. J. Phys. Oc. 6 139-156.

Garrett, C. and W. Munk (1972) Oceanic mixing by breaking internal waves. Deep Sea Res. 19 823-832.

Grant, H. L., R.W. Stewart and A. Moilliet (1962) Turbulence spectra from a tidal channel. J. Fluid Mech., 12 241-263.

Grant, H. L., A. Moilliet and W.M. Vogel (1968) Some observations of the occurrence of turbulence in and above the thermocline. J. Fluid Mech. 34 443-449.

Gregg, M. C. (1973) The microstructure of the ocean. Sc. Am. 228 64-77.

Gregg, M. C. (1975) Oceanic fine and microstructure. Rev. of Geophys. and Space Phys. 13 586-593.

Gregg, M. C. (1976) Temperature and salinity microstructure of the Pacific Equatorial Undercurrent. J. Geophys. Res. 81 1180-1196.

Gregg, M. C. and C.S. Cox (1971) Measurements of oceanic microstructure of temperature and electrical conductivity. Deep Sea Res. 18 925-934.

Hinze, J. O. (1959) Turbulence. McGraw Hill, New York 586 pp.

Jones, J. H. (1973) Vertical mixing in the equatorial undercurrent. J. Phys. Oc. 3 286-296.

Kaimal, J. C., J. C. Wyngaard, Y. Izumi and O.R. Cote (1972) Spectral characteristics of surface-layer turbulence. Quart. J. Roy. Meteor. Soc. 98 563-589.

Katz, E. J., R. Belevitsch, J. Bruce, V. Bubnov, J. Cochrane, W. Düing, P. Hisard, H.-U. Lass, A. deMesquita, L. Miller, A. Rybnikov (1976) Zonal pressure gradient along the Equatorial Atlantic. J. Mar. Res. (to be published in May, 1978).

Koop, C. G. (1976) Instability and turbulence in a stratified shear layer. Ph. D. Thesis, Dept. of Aerospace Engineering, University of Southern California, Los Angeles.

Lee, C. M. (1974) UBC FOURT: discrete Fourier transforms with applications to Fourier series and convolution integrals. Documentation by the Computing Centre, University of British Columbia.

Linden, P. F. and J. S. Turner (1975) Small-scale mixing of stably stratified fluids; a report on Euromech 51. J. Fluid Mech. 67 1-16.

Lock, C. N. H. and F. C. Johansen (1931) Wind tunnel interference on streamline bodies; theory and experiments. Aeronautical Research Committee Reports and Memoranda No. 1451.

Lueck, R. G., O. Hertzman and T. R. Osborn (1976) The spectral response of thermistors. Submitted to Deep Sea Res.

Lumley, J. L. and J. F. McMahon (1967) Reducing water tunnel turbulence by means of a honeycomb. Trans. of the ASME, paper no. 67-fe-5.

Metcalf, W. G., A. D. Voorhis and M. C. Stalcup (1962) The Atlantic Equatorial Undercurrent. J. Geophys. Res. 67 2499-2508.

Miles, J. W. and L. N. Howard (1964) Note on a heterogeneous shear flow. J. Fluid Mech. 20 331-336.

Monin, A. S. and A. M. Yaglom (1971) Statistical Fluid Mechanics: Mechanics of Turbulence V-1. MIT Press, Cambridge, Mass. 769pp.

Monin, A. S. and A. M. Yaglom (1975) Statistical Fluid Mechanics: Mechanics of Turbulence V-2. MIT Press, Cambridge, Mass. 874 pp.

Montgomery, R. B. and E. D. Stroup (1962) Equatorial waters and currents at 150°W in July-August 1952. Oceanogr. Study 1 Johns Hopkins University, Baltimore.

Miyake, Y. and M. Koizumi (1948) The measurement of the viscosity coefficient of seawater. J. Mar. Res. 7 63-66.

Nasmyth, P. W. (1970) Oceanic Turbulence. Ph. D. Thesis, Inst. of Oceanography, University of British Columbia.

Neshyba, S. and V. T. Neal (1971) Temperature and conductivity measurements under ice island T-3. J. Geophys. Res. 76 8107-8120.

Neumann,G. and W. J. Pierson (1966) Principles of Physical Oceanography. Prentice-Hall, N. J. 545 pp.

Obukhov, A. M. (1959) The influence of hydrostatic forces on the structure of the temperature field in turbulent flow. Dok. Akad. Nauk. SSSR 125 1246-1248.

Orlanski,I. and K. Bryon (1969) Formation of the thermocline step structure by large amplitude internal gravity waves. J. Geophys. Res. 74 6975-6983.

Osborn,T. R. (1974) Vertical profiling of velocity microstructure. J. Phys. Oc. 4 109-115.

Osborn,T. R. and C. S. Cox (1972) Oceanic fine structure. Geophys. Fluid Dyn. 3 321-345.

Osborn,T. R. and T. E. Siddon (1975) Oceanic shear measurements using the airfoil probe. Proceedings Third Biennial Symposium on Turbulence in Liquids, Rolla, Missouri.

Ozmidov,R. V. (1965) Energy distribution between oceanic motions of different scales. Izv. Atmos. and Oceanic Physics, Series 1 853-860.

Pankhurst, R. C. and D. W. Holder (1952) Wind-Tunnel Technique. Pitman, London 702 pp.

Philander, S. G. H. (1973) Equatorial undercurrent: measurements and theories. Rev. Geophys. and Space Phys. 11 513-570.

Philander, S. G. H. (1976) Instabilities of zonal equatorial currents. J. Geophys. Res. 81 3725-3735.

Pond, S. (1965) Turbulence spectra in the atmospheric boundary layer over the sea. Ph. D. Thesis, Institute of Oceanography, University of British Columbia.

Pond,S. (1973) Turbulence, Physics 540. A course taught at the University of British Columbia.

Rinkel,M. O., P. Sund and G. Neumann (1966) The location of the termination area of the equatorial undercurrent in the Gulf of Guinea based on observations during Equalant III. J. Geophys. Res. 71 3893-3901.

Rybnikov, A. A. (1975) Current measurements at the equator during GATE. Report submitted to GATE Equatorial and A-Scale Informal Workshop. Held at WMO, Geneva.

Sanford, T. B. (1975) Observations of the vertical structure of internal waves. J. Geophys. Res. 80 3861-3871.

Seitz, R. C. (1973) Observations of intermediate and small scale turbulent water motion in a stratified estuary. Parts I and II. Ref. 73-2 Chesapeake Bay Institute, The Johns Hopkins University.

Shur, G. N. (1962) Experimental investigations of the energy spectra of atmospheric turbulence. Trudy Tsentr. Aerol. Obs. No. 43 79-80.

Siddon, T. E. (1965) A turbulence probe utilizing aerodynamic lift. University of Toronto Inst. for Aerospace Studies. Tech. note 88.

Siddon, T. E. (1969) On the response of pressure measuring instrumentation in unsteady flow. University of Toronto Inst. for Aerospace Studies. Report No. 136.

Simpson, J. H. (1972) A free fall probe for the measurement of velocity microstructure. Deep Sea Res. 19 331-336.

Smith, S. D. (1974) Eddy flux measurements over Lake Ontario. Boundary Layer Meteor. 6 235-255.

Smith, R. H. and C. Wang (1944) Contracting cones giving uniform throat speeds. J. of the Aeronautical Sci. 11 356-360.

Stewart, R. W. (1959) The problem of diffusion in a stratified fluid. Adv. in Geophys. 6 303-311.

Stewart, R. W. (1969) Turbulence and waves in a stratified atmosphere. Radio Science. 12 1269-1278.

Stewart, R. W. and H. L. Grant (1962) Determination of the rate of dissipation of turbulent energy near the sea surface in the presence of waves. J. Geophys. Res. 67 3177.

Tennekes, H. and J. L. Lumley (1972) A First Course in Turbulence. MIT Press, Cambridge, Mass. 300pp.

Thorpe, S. A. (1973) Turbulence in stably stratified fluids: a review of laboratory experiments. Bound. Layer Meteor. 5 95-119.

Turner, J. S. (1973) Buoyancy Effects in Fluids. Cambridge at the University Press. 366 pp.

van Mieghem, J. (1973) Atmospheric Energetics. Clarenden Press, Oxford. 306 pp.

Vinnichenco, N. K. (1969) Recent investigations of clear-air turbulence in the U. S. S. R. In Clear Air Turbulence and its Detection, Proceedings of a Symposium in Seattle, 1968. Plenum Press, New York. 246-270.

Weiler, H. S. and R. W. Burling (1967) Direct measurements of stress and spectra of turbulence in the boundary layer over the sea. J. Atmos. Sci. 24 653-664.

Williams, A. J. (1974) Salt fingers observed in the Mediterranean outflow. Science. 185 941-943.

Williams, R. B. and C. H. Gibson (1974) Direct measurements of turbulence in the Pacific Equatorial Undercurrent. J. Phys. Oc. 4 104-108.

Woods, J. D. and G. G. Fosberry (1969) The structure of the thermocline. Underwater Assoc. Report 5-19.

Wyrtki, K. and E. B. Bennett (1963) Vertical eddy viscosity in the Pacific Equatorial Undercurrent. Deep Sea Res. 10 449-455.

APPENDIX A

Shear Probe Calibration

For a slender body of revolution in an inviscid flow of speed U and angle of attack α, (assumed small) Allen and Perkins (1952) give the cross force per unit length

$$f \sim \left(\tfrac{1}{2}\rho U^2\right)\frac{dA}{dx}\sin 2\alpha \qquad \text{A-1}$$

f cross force per unit length

ρ density of f

$\frac{dA}{dx}$ rate of change in body cross sectional area with longitudinal distance along the body.

The authors compare this theoretical result with the force observed on a model of a dirigible, and find that near the forward tip of the dirigible, for $\alpha = 6°$, the measurements agree well with theory, and viscous effects are small. At $\alpha = 12°$ and $18°$, the theory underestimates the force slightly. This portion of the dirigible is very similar to the tip of the shear probe, and if equation A-1 is integrated along the length of the shear probe from the tip to where $\frac{dA}{dx}$ is 0, then the total cross force is

$$F \sim \left(\tfrac{1}{2}\rho U^2\right)A\sin 2\alpha \qquad \text{A-2}$$

(They note that at small angles, one can approximate $\sin 2\alpha \approx 2\alpha$, and this approximation has been made by Simpson(1972). There is a secondary cross force which varies as $\sin^2\alpha$ and is felt all along the body, not just at the tip where $\frac{dA}{dx} \neq 0$ and this force has been neglected for small values of α.

The configuration of α, U and the shear probe were shown in figure 7. The ability of the shear probe to measure the cross-stream velocity u is evident if equation A-2 is rewritten using the double angle relation for sin 2α.

$$F_c \sim (\tfrac{1}{2}\rho U^2) A 2 \sin\alpha \cos\alpha$$
$$= \rho A V u \qquad \text{A-2}$$

where V and u are shown in figure 7. It can be seen that the force is linear with u.

Another approach, described by Osborn and Siddon (1975) also yields an output linear with u, but in a slightly different way. They assume

$$F_c \sim (\tfrac{1}{2}\rho U^2) A \left(\frac{dC_L}{d\alpha}\right) \alpha \qquad \text{A-4}$$

Where $\frac{dC_L}{d\alpha}$ is the change in lift coefficient with angle of attack, and is assumed constant for wavelengths much larger than the effective length of the sensor. Equation A-4 is derived from an extension to airfoil theory for a finite width airfoil. At small angles, $U^2\alpha \approx Vu$ and this expression for F_c approaches the form of equation A-3.

The two perpendicular components of the cross stream velocity u are sensed by orthogonal biomorph beams within the probe which generate voltages proportional to the cross force. To calibrate the probes, these voltages are passed to identical calibration preamplifiers whose output voltages are recorded.

Two water flow devices for calibration of the shear probes have been used. One operates at flow speeds of 100-150 cm/sec, and has been

described by Osborn and Siddon (1975). The calibration preamplifiers cannot amplify d.c. voltages, so a flow is directed at the probe by a rotating nozzle inclined at 5° to the axis of the probe. This calibration device operates poorly at flow rates below 100 cm/sec and rotation rates less than 16 Hz; and it gives no check of linearity of response with the cross stream velocity.

A second calibrator, shown in figure A-1, incorporates major changes to allow slower flow speeds and rotation rates. A jet is discharged vertically into a tank of water, with the tip of the probe mounted just above the centre of the outlet at an angle α. Water for the jet passes through a mesh and honeycomb arrangement to reduce the scale size and intensity of turbulence. The honeycomb also reduces large scale vorticity which would produce disastrous effects when advected through the reducer. A design of Smith and Wang (1944) was used for the reducer to create a uniform flow at the nozzle. The diameters at the wide and nozzle ends of the reducer are 10 cm and 2 cm respectively, to give an area reduction ratio of 25.

The probe is tilted successively at $2\frac{1}{2}°$ intervals from 10° left to 10° right, and rotated about its axis, generating sinusoidal voltages from each beam which are carried to the preamplifiers mounted behind the probe. Slip rings bring positive and negative supply voltages from the preamp, and tap the signals from the two channels of the preamp. A fifth ring is for ground. The output signals are sent through a low pass (-3db at 10 Hz) unity gain filter to an oscilloscope to check for any bumps or spikes in the

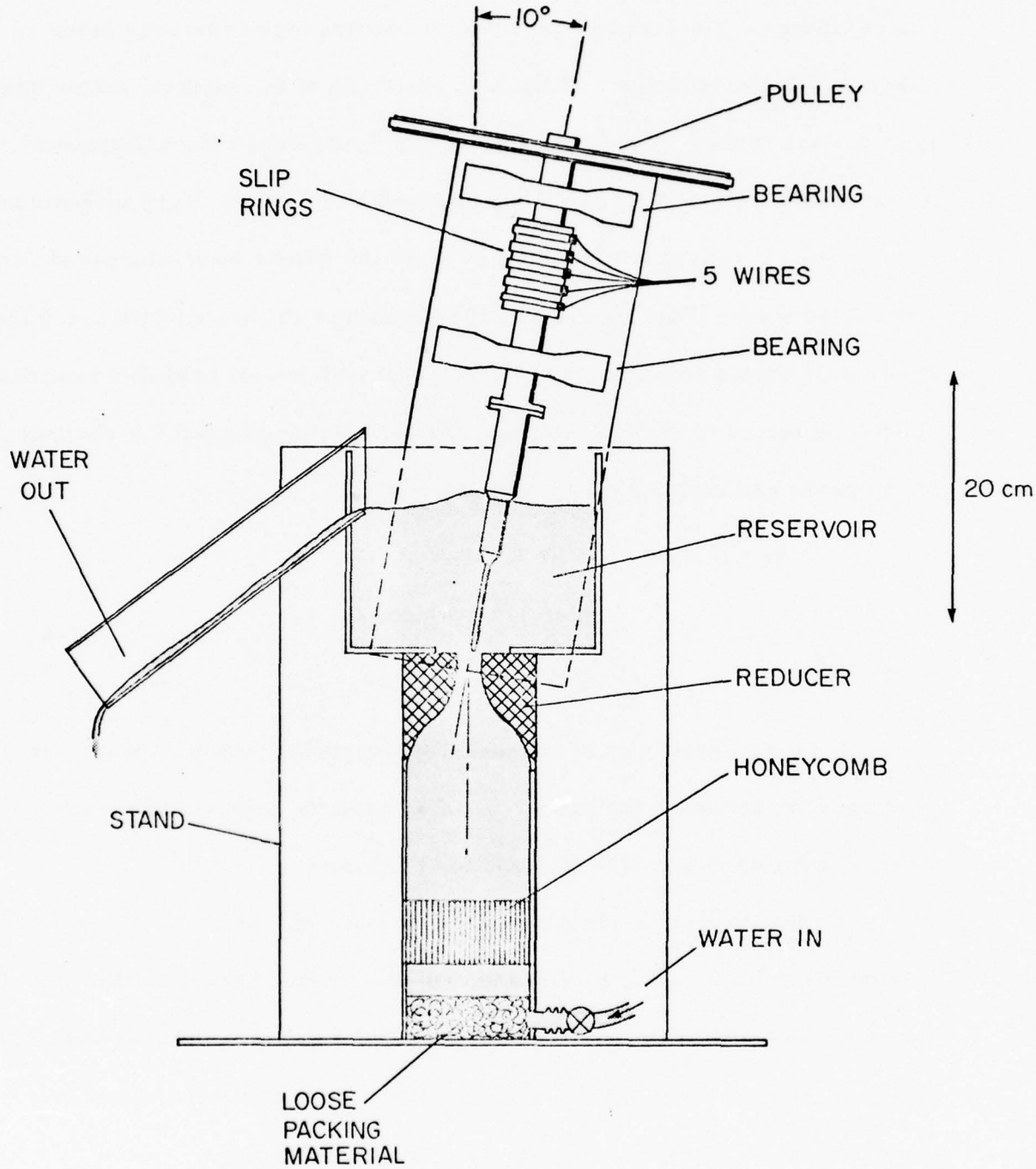

Figure A-1 The shear probe calibrator

output voltage. The filter is required to remove high frequency noise generated by the vibrations of the slip rings and of the electric motor used to rotate the probe. A rotation rate of 2.5 Hz was used for calibrations. An increased rate of 5 Hz produced no change of output voltage magnitude.

The sinusoidal output voltages from the filters were measured with a true rms meter (Disa model 55 D35) which was calibrated with a 2.5 Hz sine signal whose amplitude was determined with a well calibrated oscilloscope. In terms of the rms voltage, the peak voltage output for channel 1 of the probe and calibration preamplifier is

$$\begin{aligned} U_{c1} = \sqrt{2}\, U_{rms} &= \tfrac{1}{2} \rho S_1 U^2 \frac{\sin 2\alpha}{2} \\ &= \tfrac{1}{2} \rho S_1 U^2 \sin\alpha \cos\alpha \\ &= \tfrac{1}{2} \rho S_1 V u \end{aligned} \qquad \text{A-5}$$

where S_1 is the sensitivity of channel 1 of the probe, which depends not only upon the nature of the probe, but also upon the gain of the preamplifier. A similar expression is found for channel 2.

On board ship, a pump was used to drive the jet. The water recirculated through the system. On land, an overflowing bucket on the roof of one of the Oceanography huts at UBC provided a uniform pressure head to drive the jet. The use of this calibrator to provide accurate values of sensitivities requires the consideration of several factors.

(a) Gravity

The probe tip is more dense than water. When the probe is rotated with the tank full of water, but with no jet flowing, the force of gravity

downward on the probe produces a sinusoidal voltage at the output terminals. This force is present when the jet flows past the probe. It is 180° out of phase with the force of the jet. The ratio of the voltages from the probe caused by these forces at 40 cm/sec flow speed in the calibrator is

$$\left|\frac{Lj}{Lg}\right| \sim 3$$

Lj is the lift due to the jet (always upward).

Lg is the gravitational force (always downward).

The ratio varies with V^2. *This large effect was not forseen in building* the calibrator. With the jet flowing, the net lift is Lj - Lg. With no jet flowing, but the probe immersed in water, the net lift is Lg. The corresponding output rms voltages were measured at various angles and added together to produce the voltage expected from Lj alone. This procedure is satisfactory for sinusoidal signals, but any noise or stray signals generated would be added doubly by this method. The flow speed was increased to 70-80 cm/sec, where $|Lj/Lg| \approx 10$ and stray noise became much less troublesome. Most calibrations were at these flow speeds.

(b) Boundary layer in the nozzle

It would appear at first that the flow speed through the nozzle would be the volume flow rate in cm^3/sec divided by the area of the nozzle. The flow rate can be measured easily, but a boundary layer in the nozzle may reduce the effective cross-sectional area of the flow. This area must be known to calculate the flow speed U. The sensitivity varies as the square of this speed, and the measured dissipation $\bar{\epsilon}_M$ varies as the square of the sensitivity. Thus the dissipation depends on the 4th power of effective

cross-sectional area of the flow. Small boundary layers or bubbles on the walls of the nozzle can cause large errors in the estimates of dissipation.

Some method is required to accurately measure the speed. The most satisfactory solution found is to measure the dynamic pressure $\frac{1}{2}\rho U^2$ in the jet with a manometer and pitot tube. This system has the advantage of measuring U^2 directly. A large bore inclined manometer gave accurate readings of the height of the water column. For a pitot tube, a plastic pipet was used, with part of the tip cut away to leave a 4 mm end to be directed into the flow. The dynamic pressure was found to be uniform across the core of the jet. Pressures outside the jet were uniform also. Abramovich (1963) states that observed static pressures in a submerged jet such as observed here are the same inside and outside the jet. Therefore, the difference in the pressures observed is the dynamic pressure of the flow in the core of the jet. Figure A-2 shows the flow speed for various volume flow rates. The value of U^2 given by the manometer should be accurate to better than 1% (Bradshaw, 1964). The repeatability of results was within 2% to 4% and should be the error in measurements. There is no reason for the fit to be linear, but the line drawn does fit the points well. It was also noted that the flow speed increased slowly in time during a steady volume flow rate, due to an accumulation of bubbles in the nozzle. Flow speeds could be increased by 5% due to this effect. During the ATLANTIS II cruise, no check was made on this accumulation of bubbles, and resulting errors in sensitivity can be up to 10%. For more recent calibrations, the nozzle has been brushed clean of bubbles.

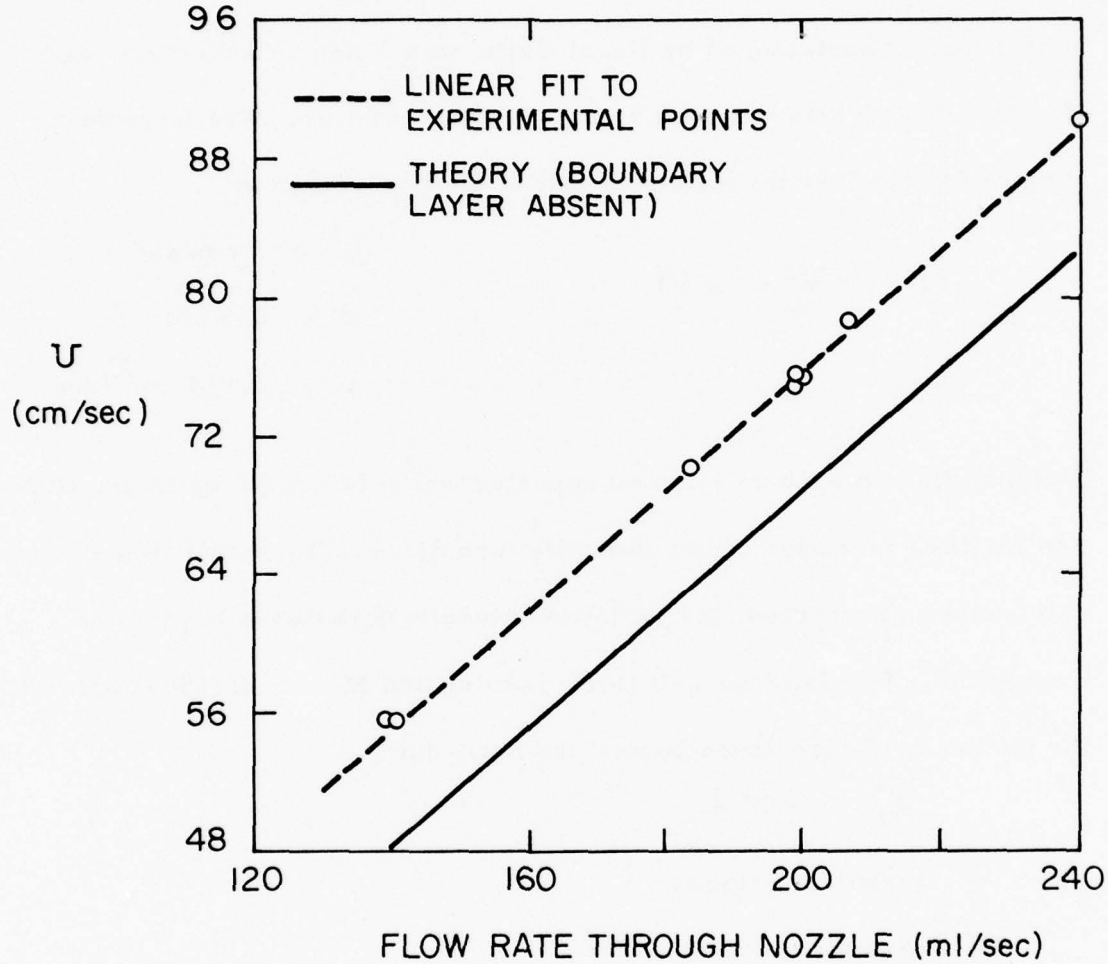
96
88
80
72
64
56
48
U
(cm/sec)
LINEAR FIT TO
EXPERIMENTAL POINTS
THEORY (BOUNDARY
LAYER ABSENT)
120
160
200
240
FLOW RATE THROUGH NOZZLE (ml/sec)

(c) Turbulence

The large scale turbulence was reduced by using packing material in the bottom of the calibrator, and aluminum honeycomb or straws. The honeycomb, manufactured by Hexel Corp. was 3 mm cell diameter and 50 mm deep. It was mounted 9 cm below the reducer. The Reynolds number for the flow through each cell of the honeycomb is

$$R_e = \frac{Ud}{\nu} = 64 \qquad \begin{aligned} U &= 3 \text{ cm/sec} \\ d &= 0.3 \text{ cm} \\ \nu &= 0.014 \text{ cm}^2/\text{sec} \end{aligned} \qquad \text{A-6}$$

Laminar flow in each cell can be expected which is not the optimum situation for the generation of low intensity turbulence. Turbulent flow in each cell would be preferred, giving lower intensity turbulence beyond the honeycomb. For laminar cell flow, Lumley and McMahon (1967) predict, for the decay of turbulence beyond the honeycomb

$$\frac{\overline{u'^2}}{U^2} \sim \frac{0.03\, d}{x} \qquad \text{A-7}$$

u' turbulent velocity

U average velocity

d honeycomb diameter

x distance downstream

From the honeycomb to the reducer is 30 diameters and $\frac{\overline{u'^2}}{U^2}$ should be 0.001 at the reducer. Pankhurst and Holder (1952) give $\overline{u'^2}$ as roughly constant in a reducer, and U^2 increases by $(25)^2$, pushing turbulent intensities even lower.

The shear probe itself is a good detector of turbulence. I tried a

simple test to determine the turbulence level in the flow of water. With the jet flowing and the probe inclined at 10° to the flow, the rms voltage observed with the probe not rotating was 2% of the rms voltage observed during rotations.

The signal from the rotating probe varies as $U^2 \frac{\sin 20°}{2}$. The non-rotating probe will not detect the mean cross flow because signals at frequencies less than 0.1 Hz are filtered by the preamplifier. The output signal will only contain the higher frequencies of cross flows, due to turbulence, which vary as $Vu' \sim Uu'$. The ratio of the signals is

$$\frac{Uu'}{U^2 \frac{\sin 20°}{2}} = 0.02$$

from which $\sqrt{\overline{u'^2}}/U \sim 0.3\%$ which indicates low levels of turbulence at scales and frequencies which the probe and filters will pass.

(d) Water tunnel blockage effects

In the ocean the probe falls through the ocean at speed V. In the calibration tank an open jet of water 2 cm across is directed at the probe. The deflection of streamlines in the jet is not the same as in the ocean. The jet streamlines spread more easily around the probe, reducing the effective dynamic pressure. If the probe is inclined in the jet, the lift is not the same as experienced in the ocean. Pankhurst and Holder (1952) have described the following corrections for these effects for wind tunnels.

When an airfoil is introduced into a wind tunnel, the solid blockage at the mid-point along the length of the airfoil is conveniently expressed by

$$U_F = U_T (1 + \varepsilon_s) \qquad \text{A-8}$$

U_T tunnel speed far from the model

U_F tunnel speed at the midpoint of the chord of the model

For the case of the shear probe, one wishes to find the blockage near the tip of the probe, where $\frac{dA}{dx} \neq 0$ (i.e., where the probe is most sensitive to the cross-flow). One possible way to examine the blockage near the probe tip is to consider only the rubber portion of the probe as the airfoil, and the stainless steel tubing behind the probe as a solid wake. This distinction is rather arbitrary, and the resulting fineness ratio of 5 is higher than the value derived if only the sensitive portion of the probe is considered as being an airfoil. Pankhurst and Holder have cited results of Lock and Johansen (1931) who found the effect of wake blockage small when compared to the solid blockage of an airfoil. In the absence of better information, I assume this to be a valid assumption here, and will proceed with the fineness ratio of 5.

Pankhurst and Holder (1952) have published values of ε_s for various flows. For an open axisymmetric jet blocked by an axisymmetric body, ε_s is given by

$$\varepsilon_s = \tau_N \lambda_A \left(\frac{A}{C}\right)^{3/2} \qquad \text{A-9}$$

$\frac{A}{C}$ = ratio of cross-sectional area of probe to cross-sectional area of nozzle.

τ_N = constant characteristic of nozzle = -0.206 for open circular jet.

λ_A = constant characteristic of airfoil. This is chosen as 5 which is the value for a Rankine Ovoid of fineness ratio 5, and

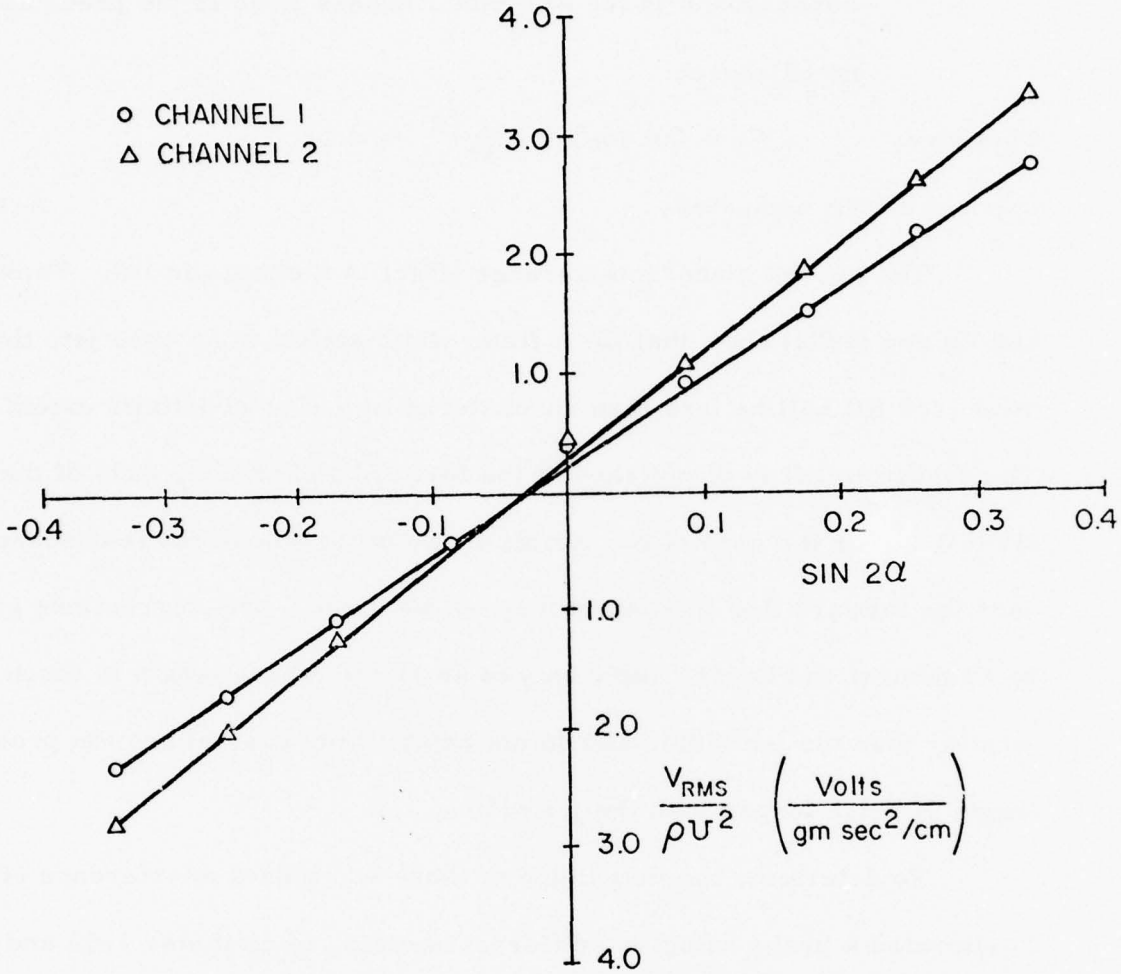

Figure A-3 Calibration curve of the shear probe

corresponds to the assumed fineness ratio of the probe as noted above.

This gives $$\varepsilon_s = (-0.206)(5)\left(\frac{1}{16}\right)^{3/2} \approx 0.02$$

which has been neglected. A-10

The second tunnel interference effect is a change in lift. Pankhurst and Holder (1952) show that for a finite width airfoil in an open jet, the measured lift will be less than encountered in a flow of infinite extent. The change in lift is diminished at the forward and trailing ends of the airfoil, so for the case of the airfoil shear probe whose lift is concentrated near the forward tip, this effect may not be large. The corrections given by Pankhurst and Holder apply only to an airfoil whose length is much smaller than the jet width, and do not apply in my case where the probe length is much longer than the jet width.

To determine the magnitude of these two tunnel interference effects, I calibrated a probe using two different nozzles, of diameter 1.92 and 3.00 cm, and found, for similar flow speeds that outputs with the larger nozzle were about 4% to 5% greater. The ratio of the nozzle areas is .41. The blockage effect varies inversely as the three-halves power of the area of the nozzle (equation A-9) and the lift effect varies inversely as the area (Pankhurst and Holder, 1952) and an upper limit of the total error due to these two effects in the smaller nozzle is found by assuming the sum of these two errors to vary inversely as the nozzle area. In such a case, for the smaller nozzle, this total error is 6% to 8% of the measured lift. All calibrations were done with the smaller nozzle, and no correction has been made for this error.

Probe Sensitivities

As the probe rotates in the jet, the lift on the probe remains constant, but the lift on the individual beam varies sinusoidally. The peak output voltage is for channel 1:

$$U_{c1} = S_1 \left(\tfrac{1}{2}\rho U^2\right) \frac{\sin 2\alpha}{2} \qquad \text{A-4}$$

In practice, the rms voltage is measured and the peak voltage derived. To find S_1 and S_2, the values of $\frac{(U_{c1})_{rms}}{\rho U^2}$ are plotted versus sin 2α as in figure A-3. The flow rate is measured easily by trapping the overflow from the tank. The speed U is determined from the flow rate and the graph in figure A-2. The output voltage is linear with sin 2α beyond $\alpha = 2.5°$ but is higher at small angles. This deviation is due to non-perfect alignment of the axis of the probe with the axis of the jet, such that $\alpha = 0°$ cannot be achieved. The relative angle of the jet can be measured accurately (better than 0.2°) but the absolute angle, as shown in figure A-3 was out by 1° . That is, the reading at 10° to the right was actually at 11° , and the reading at 10° to the left was actually at 9° , etc. One would expect that because sin 2α is not a linear function of α at angles near 10° that an error would result from mislabeling the angles in this way; however, the error is small (< 1%).

A larger error results from a tilt of the entire plane of inclination relative to the jet axis. I checked this angle before a calibration, but could not be sure that it was less than 1° . If the plane of inclination is tilted forward at an angle of say 1° , then a true angle of 1° is present for

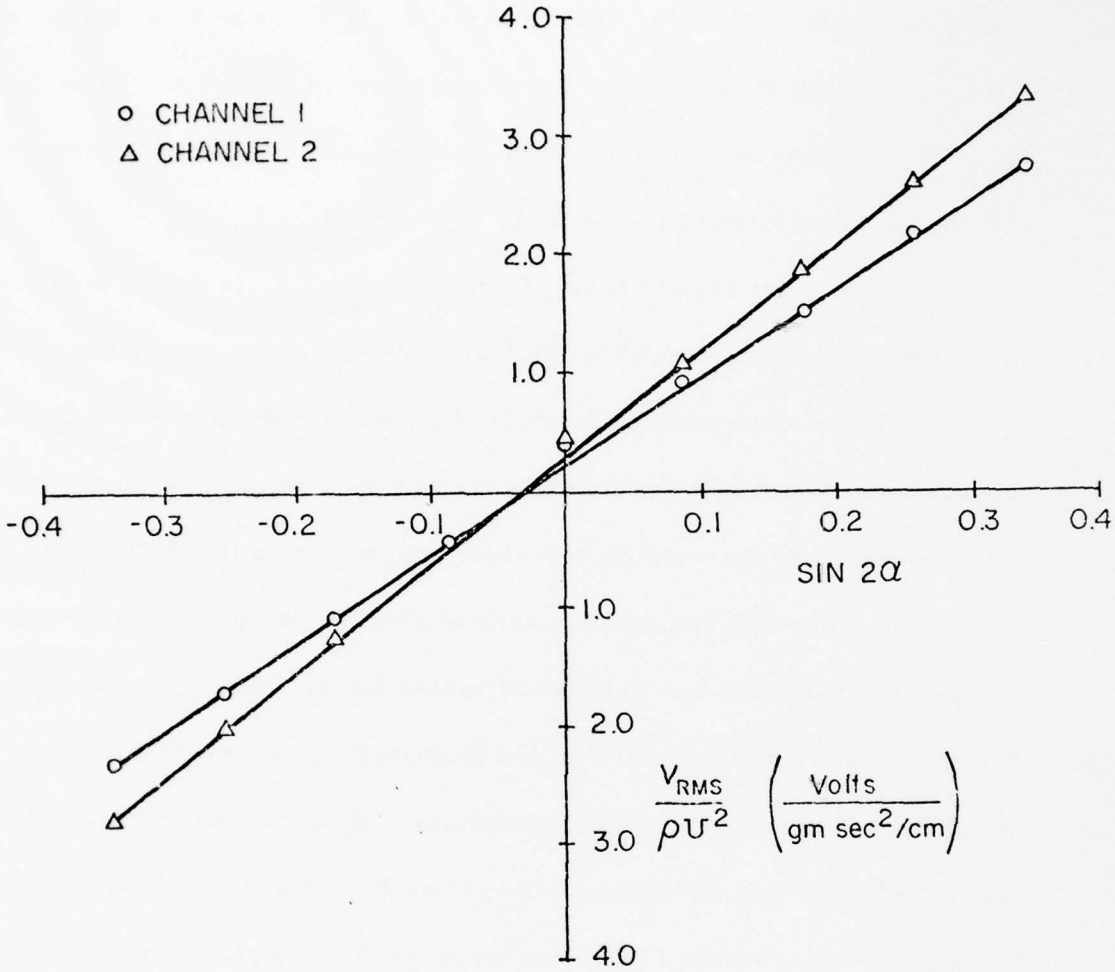

Figure A-3 Calibration curve of the shear probe

a nominal angle of 0°. The effect of this tilt is diminished at larger angles; the true angle is 2% larger for a nominal angle of 5°, 1% at $7\frac{1}{2}$° and 0.5% at 10°. To calculate sensitivities, most weight was put on these three angles, and the expected error in sensitivity is 2%.

The largest errors result from uncertainties in the flow rate in the calibrator during the ATLANTIS II cruise, and the tunnel interference effects. The probes were recalibrated upon our return to Vancouver, but variations of about 10% are found in the two sets of calibrations. It may be that the values of the sensitivities determined during the ATLANTIS II cruise are up to 10% too high because of bubbles in the nozzle during the cruise, and 6-8% too low because of tunnel interference effects. Other errors, such as undertainties in the flow rate, in the angle of tilt and in the change of sensitivity with temperature may contribute to a lesser extent to the overall uncertainty in the value of the sensitivity. I have allowed that the overall error may be up to 20%. Errors in the probe sensitivities are smaller for recent calibrations.

APPENDIX B

Data Analysis

The analogue signals were transmitted from the Camel up a XBT wire as FM multiplexed signals, and recorded on a Hewlett Packard 3960 Instrumentation Recorder. A 14.5 kHz signal was also recorded. The signals were demodulated and demultiplexed by a set of Sonex discriminators, the 14.5 kHz signal being used for tape speed compensation. The shear signals were carried on the 2.3 and 3.0 kHz channels. These analogue signals were digitized at 200 times per second onto 9-track magnetic tape by a 10 bit converter on a PDP-12 computer. Analysis was done on an IBM 370 computer at the University of British Columbia. All eight signals from the Camel were digitized in this manner. The horizontal velocities u_1 and u_2 were sensed by the probe sampling in the x_3 direction. The corresponding spectra measured are $\varphi_{11}(k_3)$, $\varphi_{22}(k_3)$, $(k_3)^2\varphi_{11}(k_3)$ and $(k_3)^2\varphi_{22}(k_3)$.

Dissipation Calculations

The two metre averages of the viscous dissipation were derived from fast Fourier transforms (FFT) of 1024 digitized points. Each FFT gave 513 complex transform values, and the square of the moduli of the last 512 were averaged in blocks of 4 and the cumulative sums of the first 45 blocks (for frequencies up to 35 Hz) were printed out. The first transform value is the mean, and was always zero; (the average was computed and subtracted from each digitized record of 1024 points before the

FFT computation).

The measured signals, transmitted to the ship and recorded are of $\frac{\partial u_1}{\partial t}$, $\frac{\partial u_2}{\partial t}$. The values are related to the output voltages by

$$\frac{\partial u_1}{\partial t} = \frac{1.80}{\rho S_1 V} v_{01} \qquad \text{B-1}$$

$$\frac{\partial u_2}{\partial t} = \frac{1.75}{\rho S_2 V} v_{02} \qquad \text{B-2}$$

as shown in Appendix C and, by use of Taylor's hypothesis, valid in this case, one has

$$\frac{\partial u_1}{\partial x_3} = \frac{-1.80}{\rho S_1 V^2} v_{01} \qquad \text{B-3}$$

$$\frac{\partial u_2}{\partial x_3} = \frac{-1.75}{\rho S_2 V^2} v_{02} \qquad \text{B-4}$$

The effects of the high and low pass filters have been neglected here, but they are discussed in Appendix C. The constants 1.80 and 1.75 in equations B-1 to B-4 have dimensions of seconds $^{-1}$, and are referred to in section 3.1 as $2K_1$ and $2K_2$.

When digitized, one volt of input is given a value of 250 bits; thus, when converting the digitized output to volts, one must multiply by (1/250). Hence

$$\left(\frac{\partial u_1}{\partial x_3}\right)_\ell = -\frac{1.80}{250 \rho S_1 V^2} d_\ell \qquad \text{B-5}$$

where d_ℓ is the ℓ-th digital value, and ℓ ranges from 0 to 1023. The FFT does not give the Fourier sine and cosine coefficients directly, but the

following discussion, from Lee (1974) shows how the discrete Fourier transform values (i.e., the values given by the FFT) are related to the Fourier series sine and cosine coefficients.

Given N samples of real data d (where =0, 1, ... N-1) taken at equally spaced intervals $\Delta t = T/N$ (where T is the period), a corresponding Fourier series is

$$d(t) = \frac{a_0}{2} + \sum_{j=1}^{N/2} \left(a_j \cos \frac{2j\pi t}{T} + b_j \sin \frac{2j\pi t}{T} \right) \qquad \text{B-6}$$

If t=0 at d_0, then for each d_ℓ we have $\frac{t}{T} = \frac{\ell}{N}$ and

$$d(\ell) = \frac{a_0}{2} + \sum_{j=1}^{N/2} \left(a_j \cos \frac{2j\pi \ell}{N} + b_j \sin \frac{2j\pi \ell}{N} \right) \qquad \text{B-7}$$

Now the FFT of the d_ℓ is C(j), and

$$d(\ell) = \frac{1}{N} \sum_{j=0}^{N-1} C(j)\, e^{2\pi i \ell j/N} \qquad \text{B-8}$$

It is possible to show that when the $d(\ell)$ are real

$$N d(\ell) = C_0 + 2\sum_{j=1}^{\frac{N}{2}-1} \left[\mathrm{Re}(C(j)) \cos \frac{2\pi \ell j}{N} - \mathrm{Im}(C(j)) \sin \frac{2\pi \ell j}{N} \right] + (-1)^\ell C(N/2) \qquad \text{B-9}$$

where Re is the real part and Im is the imaginary part. This immediately gives the following results:

$C_0 = \frac{N}{2} a_0$ =0 in our case because the average is zero

$$\mathrm{Re}(C(j)) = \frac{N}{2} a_j \qquad \mathrm{Im}(C(j)) = -\frac{N}{2} b_j$$

$$C(N/2) = N a_{N/2} \qquad b_{N/2} = 0 \qquad \text{B-10}$$

It can be shown that the variance for d is

$$\frac{1}{N} \sum_{\ell=0}^{N-1} d^2(\ell) = \frac{1}{2} \left[\sum_{j=1}^{\frac{N}{2}-1} (a_j^2 + b_j^2) + a_{N/2}^2 \right]$$

$$= \frac{1}{2} \left[\left(\frac{2}{N}\right)^2 \sum_{j=1}^{\frac{N}{2}-1} C_j C_j^* + C_{N/2}^2 \right] \qquad \text{B-11}$$

That is, the sums of the squares of the Fourier series coefficients

divided by 2 equals the mean square value of d. For example, if the time series $d(\ell)$ is

$$d(\ell) = D \cos \frac{2\pi\ell}{N} \qquad \text{B-12}$$

The average value $\overline{d^2}$ will be $D^2/2$. The FFT of the series in equation B-11 will return only one non-zero coefficient: $C(1) = \frac{ND}{2}$, and the average of the power series will be

$$d^2(\ell) = \frac{1}{2}\left(\frac{2}{N}\right)^2 C(1)C(1) = \frac{1}{2}\left(\frac{2}{N}\right)^2 C^2(1) = \frac{D^2}{2} \qquad \text{B-13}$$

because C(1) in this case is real.

Accordingly

$$\bar{\epsilon} = \frac{15}{2}\nu\overline{\left(\frac{\partial u_1}{\partial x_3}\right)^2} = \frac{15}{2}\nu\left(\frac{1.80}{250\rho S_1 V^2}\right)^2\left[\frac{2}{N^2}\sum_{j=1}^{\frac{N}{2}-1} C(j)C^*(j) + \frac{1}{2N^2}C^2\left(\frac{N}{2}\right)\right] \qquad \text{B-14a}$$

and a similar expression holds for $\partial u_2/\partial x_3$. In practice there is noise, particularly at high frequencies and one cannot use the full sum. One can however examine the spectrum to determine the upper and lower limits of the sum. The last term in the summation of B-14a was always dominated by noise, and if the upper and lower limits of the summation for the shear spectrum where noise is relatively small are j_1 and j_2, then equation B-14a becomes

$$\bar{\epsilon} = \frac{15}{2}\nu\overline{\left(\frac{\partial u_1}{\partial x_3}\right)^2} = \frac{15}{2}\nu\left(\frac{1.80}{250\rho S_1 V^2}\right)^2\left[\frac{2}{N^2}\sum_{j=j_1}^{j=j_2} C(j)C^*(j)\right] \qquad \text{B-14b}$$

It is the separation of noise and signal in frequency space which is the advantage of calculating $\bar{\epsilon}$ in this way.

Spectra of $(\frac{\partial u_1}{\partial x_3})^2$ and $(\frac{\partial u_2}{\partial x_3})^2$

The formulae for $\frac{\partial u_1}{\partial x_3}$ are given below and the formulae for $\frac{\partial u_2}{\partial x_3}$ are the same except that the constant 1.80 is replaced by 1.75. To determine the relative contributions of signal and noise to the values of C(j)C*(j) the spectral density functions are plotted for each FFT of 1024 data points. The spectral density function of $(\frac{\partial u_1}{\partial x_3})^2$ is $(k_3)^2 \varphi_{11}(k_3)$ as given in section 2.4.

$$\bar{\epsilon} = \frac{15}{2}\nu \int_0^\infty (k_3)^2 \varphi_{11}(k_3)\, dk_3 = \frac{15}{2}\nu \overline{\left(\frac{\partial u_1}{\partial x_3}\right)^2} \qquad \text{B-15}$$

If C(j) is the jth transform value of the $\frac{\partial u_1}{\partial x_3}$ signal, then the spectral density function is

$$(k_{3_j})^2 \varphi_{11_j}(k_3) = \left(\frac{1.80}{250\rho S_1 V^2}\right)^2 \left(\frac{2}{N^2}\,\frac{C(j)C^*(j)}{\Delta k_3}\right) \quad j = 1, 2, \ldots \frac{N}{2}-1$$

$$= \left(\frac{1.80}{250\rho S_1 V^2}\right)^2 \left(\frac{1}{2N^2}\,\frac{C(j)C^*(j)}{\Delta k_3}\right) \quad j = \frac{N}{2} \qquad \text{B-16}$$

The Δk_3 is in the denominator because each Fourier series coefficient must be divided by the portion of wavenumber space which it represents.

$$\Delta k_3 = \frac{2\pi \Delta f}{V} = \frac{2\pi}{VN\Delta t} \qquad \text{B-17}$$

$$k_{3_j} = \frac{2\pi j}{VN\Delta t} \qquad \text{B-18}$$

The spectra of figure 24 are log $(k_{3j})^3 \varphi_{11_j}(k_3)$ versus log k_3, and substituting equations B-17 and B-18 into B-16.

$$(k_{3_j})^3 \varphi_{11_j}(k_3) = \left(\frac{1.80}{250\rho S_1 V^2}\right)^2 \left(\frac{2j}{N^2}\, C(j)C^*(j)\right) \quad j = 1, 2, \ldots \frac{N}{2}-1$$

$$= \left(\frac{1.80}{250\rho S_1 V^2}\right)^2 \left(\frac{j}{2N^2}\, C(j)C^*(j)\right) \quad j = \frac{N}{2} \qquad \text{B-19}$$

A plot of $(k_{3j})^3 \varphi_{11j}(k_3)$ versus log k_3 may be integrated to give the variance of the $\frac{\partial u_1}{\partial x_3}$ signal:

$$2.3 \int_0^\infty (k_3)^3 \varphi_{11}(k_3)\, d \log k_3 = \int_0^\infty (k_3)^3 \varphi_{11}(k_3)\, dk_3/k_3$$

$$= \int_0^\infty (k_3)^2 \varphi_{11}(k_3)\, dk_3$$

$$= \overline{(\partial u_1/\partial x_3)^2} \qquad \text{B-20}$$

Such a plot is variance preserving. In my case, a plot log $(k_{3j})^3 \varphi_{11j}(k_3)$ is used, which is not variance preserving, but one can see the relative contributions to the variance of $\frac{\partial u_1}{\partial x_3}$ from different wavenumbers. Spectra such as those in figure 24 were used only for this purpose -- to determine wavenumbers (or frequencies) where the noise dominated over the signal, and to determine the upper limit of the sums of the Fournier coefficients of equation B-14b. For this visual display, only the relative contributions are needed from the various frequencies, and the values of the ordinate in figure 24 are in arbitrary units.

Spectra of $(u_1)^2$, $(u_2)^2$

The energy density spectra $\varphi_{11}(k_3)$ and $\varphi_{22}(k_3)$ are

$$\int_0^\infty \varphi_{11}(k_3)\, dk_3 = \overline{u_1^2} \qquad \int_0^\infty \varphi_{22}(k_3)\, dk_3 = \overline{u_2^2}$$

B-21

Using the expressions B-16 to B-18

$$\varphi_{11j}(k_3) = \frac{C(j)C^*(j)}{\left(\frac{2\pi}{VN\Delta t}\right)\left(\frac{2\pi j}{VN\Delta t}\right)^2} \frac{2}{N^2}\left(\frac{1.80}{250\rho S_1 V^2}\right)^2$$

$$= \left(\frac{1.80}{250\rho S_1 V^2}\right)^2 \frac{NV^3(\Delta t)^3}{4\pi^3} \frac{C(j)C^*(j)}{j^2} \qquad j = 1, 2, \ldots, \frac{N}{2}-1$$

$$= \left(\frac{1.80}{250\rho S_1 V^2}\right)^2 \frac{NV^3(\Delta t)^3}{16\pi^3} \frac{C(j)C^*(j)}{j^2} \qquad j = \frac{N}{2} \qquad \text{B-22}$$

The $\log \varphi_{11}(k_3)$ and $\log \varphi_{22}(k_3)$ versus $\log k_3$ spectra are plotted in figures 18, 19, 22 and 23. The plotted values have been band averaged to give 2 average values per octave. The value of $\frac{C(j)C^*(j)}{j^2}$ was computed for each transform value, and averaged over the frequency band. The first four Fourier transform values were plotted individually, and were not averaged together. Next the 5th and 6th transform values were averaged, as were the 7th and 8th. The next band was comprised of the 9th, 10th, 11th, 12th values, and the next band included the 13th to 16th transform values, etc.

The corresponding wavenumber is the geometric mean of the entire interval, which produces the minimum distortion on the log k plots. For example, the arithmetic mean of $\frac{C(j)C^*(j)}{j^2}$ for j=9 to 12 formed one band average. The average of these was plotted at the wavenumber

$$k = (8.5 \times 12.5)^{1/2} \frac{2\pi}{NV(\Delta t)} \qquad \text{B-23}$$

To determine the fit of the universal curve to the $\varphi_{11}(k_3)$ and $\varphi_{22}(k_3)$ spectra, the point $[\log \nu^{-3/4}, \log \nu^{5/4}]$ is marked on the $\log \varphi_{11}(k_3)$ or $\log \varphi_{22}(k_3)$ vs. $\log k_3$ graph, and a line of slope +1 is drawn through the point. The point (0, 0) on the $\log F_2(k/k_s)$ vs. $\log k/k_s$ graph will lie on this line. Its position is determined by the fit of $\log F_2$ to the $\log \varphi_{11}$ or $\log \varphi_{22}$ curve; its absissa is the point $\log \epsilon^{1/4}\nu^{-3/4}$ and the ordinate is the point $\log \epsilon^{1/4}\nu^{5/4}$ on the $\log \varphi_{11}$ vs. $\log k_3$ graph. From these points, the value of $\bar{\epsilon}_u$ can be calculated. A full discussion of this procedure is given by Stewart and Grant (1962).

Universal Dissipation Spectra $G_2(k/k_s)$

From section 2.4

$$(k_1)^2 \Phi_{22}(k_1) = (k_s)^2 (\bar{\epsilon}\nu^5)^{1/4} G_2(k/k_s)$$

or

$$(k_3)^2 \Phi_{11}(k_3) = (k_s)^2 (\bar{\epsilon}\nu^5)^{1/4} G_2(k/k_s) \qquad 2.25$$

where $k_s = (\bar{\epsilon}\nu^{-3})^{\frac{1}{4}}$ 2.23

$$k_{3j} = \frac{2\pi j}{V N(\Delta t)} \qquad \text{B-18}$$

and $\Phi_{11j}(k_3)$ is defined in equation B-22.

Therefore

$$G_2(k/k_s) = \left(\frac{1.80}{250\rho S_1 V^2}\right)^2 \frac{V\Delta t}{N\pi(\bar{\epsilon}\nu)^{1/2}} \; C(j)C^*(j) \qquad j = 1, 2, \ldots, \frac{N}{2} - 1$$

$$= \left(\frac{1.80}{250\rho S_1 V^2}\right)^2 \frac{V\Delta t}{4N\pi(\bar{\epsilon}\nu)^{1/2}} \; C(j)C^*(j) \qquad j = \frac{N}{2}$$

B-24

and these values have been plotted in figure 20. The dissipation $\bar{\epsilon}$ was determined from the fit of the log Φ_{11} and log Φ_{22} curves to the universal F_2 curve.

APPENDIX C

Signal Handling

(a) Linear gain preamplifier

Electronic circuits prior to July 12, 1974 utilized a high impedance preamplifier located near the shear probe, and a differentiating amplifier in the main body of the Camel. These circuits are shown in figure C-1. The shear probe has been represented as an a.c. voltage generator in series with a capacitor Cp. Calibrations performed on an early calibrator allowed the probe and preamplifier to be calibrated together. The calibrator described in Appendix A, completed at the beginning of the ATLANTIS II cruise, required a preamplifier to be wired permanently into it, and a new but identical preamplifier was built for this purpose. The calibration preamplifier and the field preamplifier were identical in design, and were similar in gain to within about 4%.

The output voltage from the preamplifier is

$$v_{c1} = \tfrac{1}{2}\rho S_1 V u_1 \qquad \text{A-4}$$

$$= \frac{-j\omega C_p R_1}{(1 + j\omega C_{1c} R_1)} v_i \qquad \text{C-1}$$

for channel 1, and a similar expression is valid for channel 2. From the values of R_1 and C_1 it can be seen that for frequencies above 1 Hz, an excellent approximation is

$$v_{c1} = -\frac{C_p}{C_{1c}} v_i \qquad \text{C-2}$$

and the gain is uniform at frequencies of interest.

The response of the differentiating amplifier is

$$v_{D1} = \frac{-j\omega R_3 C_2}{(1+j\omega R_3 C_3)(1+j\omega R_2 C_2)} \left(\frac{R_7 + R_8}{R_8}\right) v_{c1} \qquad \text{C-3}$$

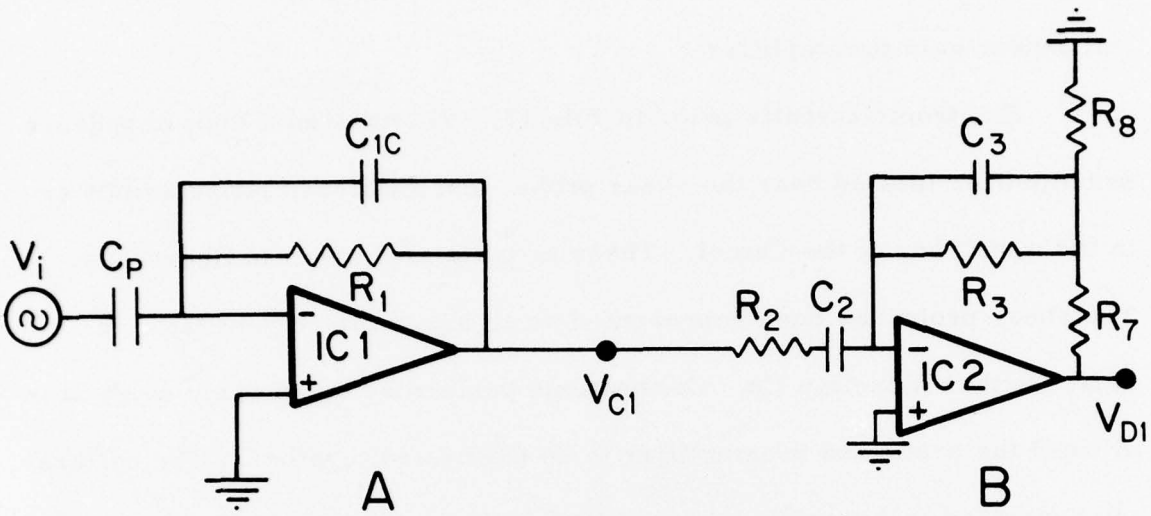

A Preamplifier
B Differentiating Amplifier

C_{1c}	1.5×10^{-10} f	R_1	$10^{10}\,\Omega$
C_2	$1. \times 10^{-6}$ f	R_2	$2.7 \times 10^{3}\,\Omega$
C_3	1.5×10^{-8} f	R_3	$1.6 \times 10^{5}\,\Omega$
IC1	AD503	R_7	$1 \times 10^{4}\,\Omega$
IC2	A777	R_8	$1 \times 10^{3}\,\Omega$

Figure C-1 The calibration and field preamplifier located near the probe and the differentiating amplifier located in the main body of the Camel in use for profile 18.

and again a similar expression holds for the output voltage v_{02} of channel 2. The amplifier differentiates the input signal to give

$$-j\omega v_{c1} = -\frac{dv_{c1}}{dt} = -\frac{1}{2}\rho S_1 V \frac{du_1}{dt} \qquad \text{C-4}$$

and also attenuates the high frequencies. The voltage from the amplifier was stepped down by $\frac{1.414}{2.5}$ by the FM transmission system, so the output voltage to the Brush recorder and the digitizer is

$$v_{01} = \left[\frac{1.414}{2.5}\right] \frac{R_3 C_2}{(1+j\omega R_3 C_3)(1+j\omega R_2 C_2)} \left[\frac{R_7+R_8}{R_8}\right]\left[\frac{1}{2}\rho S_1 V \frac{du_1}{dt}\right] \qquad \text{C-5}$$

If Taylor's hypothesis, valid in this case is applied (equation 3.3)

$$\frac{\partial u_1}{\partial x_3} = \left[\frac{2.5}{1.414}\right]\left[\frac{(1+j\omega R_3 C_3)(1+j\omega R_2 C_2)}{R_3 C_2}\right]\left[\frac{R_8}{R_7+R_8}\right]\left[\frac{-1}{\frac{1}{2}\rho S_1 V^2}\right] v_{01} \qquad \text{C-6}$$

The gain and high frequency attenuation were determined by measuring input and output voltages at various frequencies. A good fit is provided by the values:

$$\frac{\partial u_1}{\partial x_3} = \frac{-1.99(1+.0017j\omega)(1+.0018j\omega)}{\rho S_1 V^2} v_{01} \qquad \text{C-7a}$$

$$\frac{\partial u_1}{\partial x_3} = \frac{-2.08(1+.0017j\omega)(1+.0018j\omega)}{\rho S_2 V^2} v_{02} \qquad \text{C-7b}$$

for channels 1 and 2 respectively.

(b) Differentiating preamplifier

The pyroelectric effect, noted in section 3 generated a low frequency voltage in the probe sufficiently large to saturate the preamplifier during free-fall profiles at the equator. To reduce the low frequency voltages in the preamplifier, a special differentiating preamplifier was con-

structed for use during free-fall profiles called a field preamplifier, and a band pass amplifier with uniform gain over the frequencies of interest was used. The calibration preamplifier was unchanged. These circuits are shown in figure C-2.

The output of the field preamplifier

$$U_{F1} = \frac{-j\omega R_{1F} C_P}{(1 + j\omega R_{1F} C_{1F})} \left[\frac{R_5 + R_6}{R_5}\right] U_i \qquad \text{C-8}$$

and the output of the calibration preamplifier,

$$U_{C1} = \frac{-C_P}{C_{1C}} U_i$$

may be combined to eliminate the capacitance of the shear probe Cp which is an unknown.

$$U_{F1} = \frac{j\omega R_{1F} C_{1C}}{(1 + j\omega R_{1F} C_{1F})} \left[\frac{R_5 + R_6}{R_5}\right] U_{C1}$$

$$= \frac{R_{1F} C_{1C}}{(1 + j\omega R_{1F} C_{1F})} \left[\frac{R_5 + R_6}{R_5}\right]\left[\frac{1}{2}\rho S_1 V\right] \frac{du_1}{dt} \qquad \text{C-9}$$

The response of the amplifier is

$$U_{A1} = \left[\frac{-1/R_2}{\frac{1}{j\omega R_2 C_2} + 1}\right]\left[\frac{R_3}{1 + j\omega R_3 C_3}\right]\left[\frac{R_7 + R_8}{R_8}\right] U_{F1} \qquad \text{C-10}$$

and again the FM system steps down the voltage by $\frac{1.414}{2.5}$. When Taylor's hypothesis is invoked, the final expression for the shear is

$$\frac{\partial u_1}{\partial x_3} = \left[\frac{2.5}{1.414}\right]\left[\frac{\left(\frac{1}{j\omega R_2 C_2} + 1\right)(1 + j\omega R_3 C_3)}{-R_3/R_2}\right]\left[\frac{R_8}{R_7 + R_8}\right]\left[\frac{1 + j\omega R_{1F} C_{1F}}{R_{1F} C_{1F}}\right]\left[\frac{R_5}{R_5 + R_6}\right]\frac{1}{\frac{1}{2}\rho S_1 V^2} U_{01} \qquad \text{C-11}$$

for channel 1.

The three circuits (two preamplifiers and the amplifiers) were tested by measuring the input and output voltages at various frequencies while on board ship, and also by a white noise test utilizing the PDP-12 computer at the Institute of Oceanography. Each channel of each individual circuit was tested separately; the probe was simulated by an a.c. power

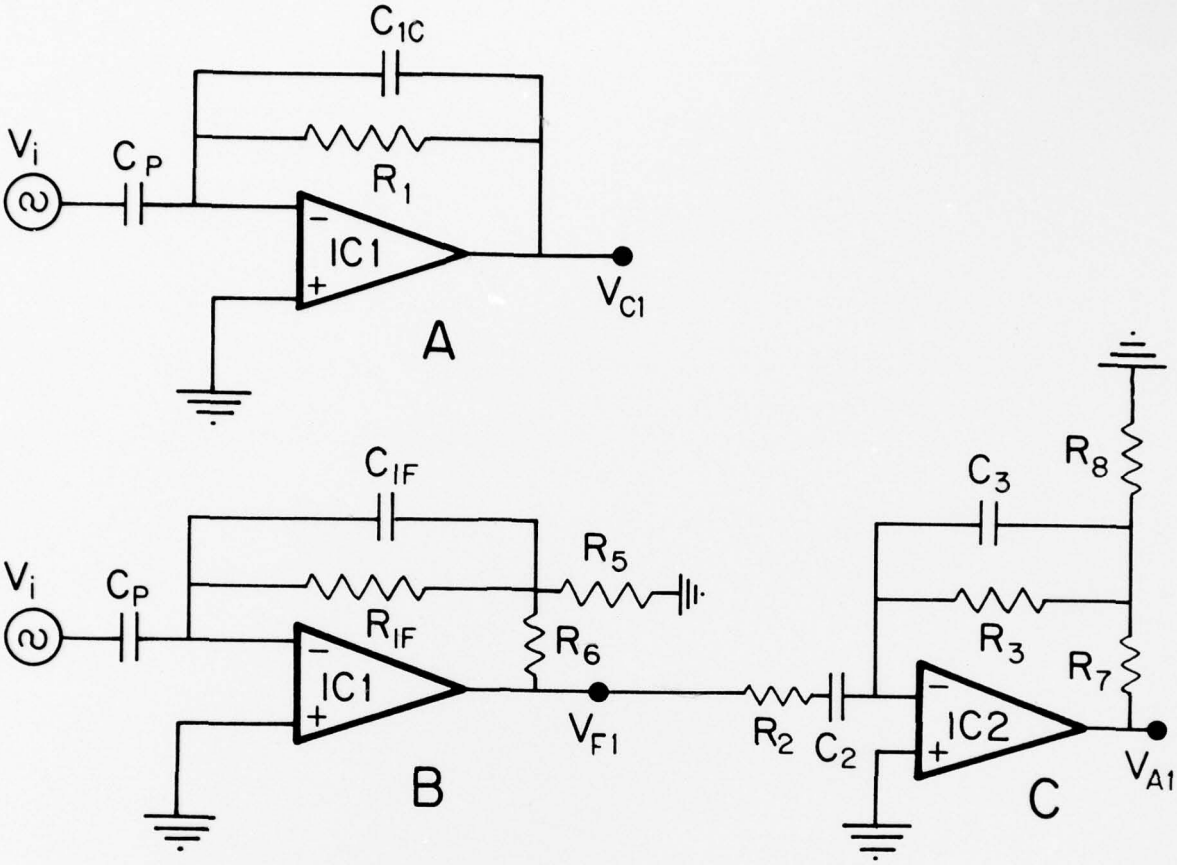

A Calibration preamplifier
B Differentiating field preamplifier
C Amplifier

C_{1c}	1.5×10^{-10} f	R_1	$10^{10}\ \Omega$	R_7	$1.\ \times10^{4}\ \Omega$
C_{1F}	1.3×10^{-10} f	R_{1F}	$2.2\times10^{7}\ \Omega$	R_8	$1.9\times10^{2}\ \Omega$
C_2	$1.\ \times10^{-6}$ f	R_2	$1.7\times10^{5}\ \Omega$		
C_3	1.5×10^{-8} f	R_3	$1.6\times10^{5}\ \Omega$		
IC1	AD503K	R_5	$1.\ \times10^{3}\ \Omega$		
IC2	A777	R_6	$1.\ \times10^{4}\ \Omega$		

Figure C-2 The calibration and differentiating field preamplifiers located near the shear probe and the amplifier located in the main body of the Camel, in use for profile 20 and following profiles.